Measurement and Modeling of Entropy Generation in Microchannels

by

Meghdad Saffaripour

A thesis
presented to the University of Waterloo
in fulfillment of the
thesis requirement for the degree of
Master of Applied Science
in
Mechanical Engineering

Waterloo, Ontario, Canada, 2008

I hereby declare that I am the sole author of this thesis. This is a true copy of the thesis, including any required final versions, as accepted by my examiners.

I understand that my thesis may be made electronically available to the public.

Meghdad Saffaripour

Abstract

Entropy based design is a novel design method that incorporates the second law of thermodynamics with computational and experimental techniques to achieve the upper limits of performance and quality in engineering technologies. As the emerging technologies are pressing towards the theoretical limits of efficiency, the concept of entropy and entropy based design will have an increasing role of performance. Measuring entropy generation is a valuable diagnostic tool from which the areas with high destruction rates of available energy may be determined and re-designed. In this work, a general model is developed, based on previous analytical expressions for pressure drop and heat transfer, for predicting entropy generation in a microchannel. The model includes the effects due to developing and fully developed flow, entrance and exit geometries, cross-sectional shapes, aspect ratio, and different thermal boundary conditions. An experimental technique is presented that enables the measurement of the spatial distribution of entropy generation in a microchannel. The experimental method is a combination of Micro Particle Image Velocimetry to measure the spatial distribution of velocity and Micro Laser Induced Fluorescence to determine the temperature data. This method provides certain advantages over conventional anemometry techniques. This method, offers the whole-field non-intrusive, and instantaneous measurement of entropy generation in the device; while, previous techniques are limited to single point, averaged measurements.

Acknowledgement

I would like to express my sincere appreciation to my supervisor, Professor J. Richard Culham, for the support, guidance, and freedom he gave me throughout the project and for his careful editing of my thesis. I appreciate Dr. Peter Teertstra and my colleagues, Elmer Galvis, William Ma, and Andrew Zwart in Microelectronics Heat Transfer Laboratory for their help in experimental setup. I thank Tom Glawdel, Razim Samy, and all the other individuals in Microfluidics Laboratory, University of Waterloo, for their help in fabricating microchannels. I should also pay tribute to Dr. Stamatious Pothos from TSI Inc. for his aid with the micro-PIV measurements. I appreciate my examining committee, Professor Metin Renksizbulut and Dr. Carolyn Ren for their valuable recommendations. I acknowledge my friends, Zeyad Almutairi, for his help with the experiments, and Arash Tajik, for his fruitful suggestions. I am grateful to Professor Kayvan Sadeghy, University of Tehran, for his encouragement and advice throughout my studies. My special gratitude goes to my parents, my sister, and my aunt for their tremendous support and love.

Dedicated to my parents and my sister, Hassan, Farzaneh, and Mahsa Saffaripour for their love and support.

M.S.

Contents

List of Tables

List of Figures

Nomenclature

A	Area, m^2
a	Acceleration, m/s^2
C	Concentration, M/m^3
C_c	Contraction coefficient
C_p	Specific heat, $J/kg \cdot K$
D	Diffusion coefficient, m^2/s
d	Diameter, m
D_h	Hydraulic diameter, m
d_e	Effective diameter, m
d_s	Diffraction limited spot size, m
E	Energy, J
$\mathbf{E}$	Elliptical integral of second kind
F	Force, N
f	Friction factor
f_{app}	Apparent friction factor
$f^{\#}$	f-number of the lens
g	Gravitational acceleration, m/s^2
H	Height, m
h	Specific enthalpy, J/kg
$\overline{h}$	Average convection coefficient, $W/m^2 \cdot K$
I	Light intensity, W
K	Loss coefficient
k	Thermal conductivity of heat-sink material, $W/m \cdot K$

k_f	Thermal conductivity of fluid, $W/m \cdot K$
L	Length, m
$\mathcal{L}$	Characteristic length, m
M	Magnification
$\dot{m}$	Mass flow rate, kg/s
n	Refraction index
NA	Numerical apperture
Nu	Nusselt number
P	Perimeter, m
p	Pressure, N/m^2
Pr	Prandtl number
$\dot{Q}$	Heat transfer rate, W
Q	Volume flow rate, m^3/s
$\mathbf{q}$	Vectorial heat transfer rate, W
R	Thermal resistance, K/W
r	Radius, m
Re	Reynolds number
S	Entropy, J/K
s	Specific entropy, $J/kg \cdot K$
T	Temperature, K
t	Time, s
t_s	Thickness of the substrate, m
$\mathbf{V}$	Velocity vector, m/s

W	Width, m
$\dot{W}$	Power, W
u, v, w	Velocity components in x, y, and z directions, m/s
x, y, z	Cartesian coordinates, m
z^+	Non-dimensional hydrodynamic entry length, $z/Re \cdot D_h$
z^*	Non-dimensional thermal entry length, $z/Re \cdot D_h \cdot Pr$

Greek

α	Absorptivity, $1/M \cdot m$
β_1	Momentum correction factor
β_2	Energy correction factor
δ	Uncertainty
δz_m	Measurement plain thickness, m
ϵ	Error
ε	Aspect ratio
η	Sensitivity coefficient
κ	Boltzmann's constant
λ	Wavelength, m
γ	Non-dimensional geometric constant
Γ	Cross-correlation function
μ	Dynamic viscosity, $N \cdot s/m^2$
ν	Kinematic viscosity, m^2/s
Φ	Viscous dissipation, $N/m^2 \cdot s$
ϕ	Quantum efficiency
Ψ	Non-dimensional entropy

ρ	Density, kg/m^3
σ	Area ratio $\equiv A_{wide\ channel}/A_{narrow\ channel}$
σ_x	Uncertainty in streamwise velocity component, m/s
σ_y	Uncertainty in normal velocity component, m/s
τ	Response time, s
τ_w	Wall shear stress, N/m^2
θ	Angle, $^\circ$
Θ	Entropy distribution ratio
υ	Specific volume, m^3/kg

Subscripts

0	Ambient	ave	Average
c	Calibration	C	Contraction
ch	Channel	$cond$	Conduction
$conv$	Convection	cs	Cross-sectional
d	Detectability	E	Expansion
ent	Entrance region	f	Friction factor
fd	Fully developed	gen	Generation
H	Hot	I	Irreversible
im	Image plane	in	Into the system
L	Loss	max	Maximum
out	Out of the system	P	Particle
p	Precision	sh	Shaft
spr	Spreading	th	Thermal
tot	Total	x	In the x direction

y	In the y direction	∞	Fully developed

Chapter 1

Introduction

The continuing increase in the operational speed and density of integrated circuits is accompanied by a steady increase in the dissipative heat flux of these components, requiring innovative cooling techniques. The microchannel liquid cooling concept was first introduced by Tuckerman and Pease [22] in 1981. This method of cooling provides a more compact, more efficient arrangement than conventional air cooling systems, due to the higher specific heat and thermal conductivity of liquids as compared to air. The laminar nature of the flow in micro-devices necessitates a heat transfer coefficient inversely proportional to hydraulic diameter of the channels. This implies that by scaling down the liquid cooled heat-sinks to microscopic dimensions, the amount of heat removal by the heat-sink can be significantly increased. The principal advantage of microchannel heat-sinks is the high surface area to volume ratios that can be achieved which leads to very high heat transfer rates. Today, microchannel heat-sinks constitute a novel technology for removing large amounts of heat from a small area. However, the huge increase in pressure drop limits the minimization of the channels. In the subsequent sections, it will be demonstrated that the second law of thermodynamics can be used to find an optimum size and geometry for the microchannels by minimizing the amount of entropy production.

1.1 Motivation

The efficiency of a heat-sink is determined by its thermal resistance, defined as:

$$R_{th} = \frac{\Delta T}{\dot{Q}} \tag{1.1}$$

where $\dot{Q}$ is the heat removal rate and ΔT is the temperature difference between the hot surface of the heat-sink and the coolant fluid at the inlet. ΔT has a fixed value, since ICs have a fixed maximum allowable temperature. Hence it is the thermal resistance that determines the amount of heat removed from the IC. The thermal resistance of a heat-sink is the sum of three terms. First, resistance against conduction in the substrate and other laminated structures:

$$R_{cond} = \frac{t_s}{kA} + R_{spr} \tag{1.2}$$

where t_s, k, A, and R_{spr} are the thickness, conductivity, surface area and spreading resistance of the substrate[1], respectively. Second, resistance against convection from the substrate to the flow or film resistance:

$$R_{conv} = \frac{1}{\bar{h}A} \tag{1.3}$$

where $\bar{h}$ is the average convection coefficient and A is the wetted surface area of the heat-sink. The last one is the resistance due to the absorption of heat by the fluid:

$$R_{flow} = \frac{1}{\dot{m}C_p} \tag{1.4}$$

where $\dot{m}$ is the mass flow rate and C_p is the specific heat of the coolant. These resistances are shown schematically in Fig. 1.1. The resistance against conduction is usually very small, because the thermal conductivity of the materials used to construct heat-sinks is typically very high (see Table 1.1), and the silicon substrates can be thinned to very small values (less

---

[1] Thermal spreading resistance occurs whenever heat leaves a heat source of finite dimensions and enters into a larger region. Depending on the relative size of heat source and the sink, spreading resistance may be significant. For more details, see [23].

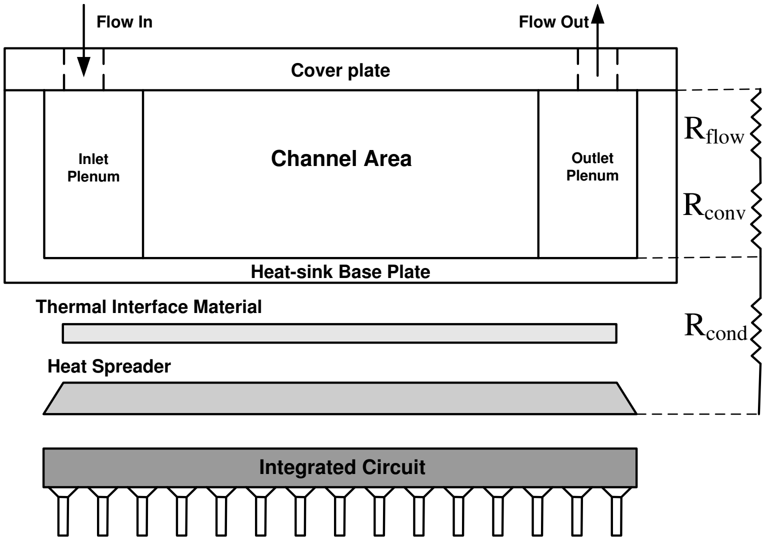

Figure 1.1: Schematic of a microchannel heat-sink package

Table 1.1: Thermal conductivity of the materials used in constructing heat-sinks

Material	k $(W/m \cdot K)$
Copper	401
Aluminum	237
Silicon	134
Graphite/Epoxy	370

than $100\mu m$). The resistance due to the heating of the fluid can be reduced by using a coolant of high specific heat capacity and high volume flow rate. The only resistance that can not be conveniently reduced is the resistance against convection, also known as film resistance. This term is the dominant and thus the controlling term in the resistance network in most heat-sinks. In order to decrease R_{conv}, we can increase either A or $\overline{h}$. To increase A we can create channels for the flow on the back side of the IC substrate, rather than simply flowing the coolant over a flat, smooth surface.

The average convection coefficient, $\overline{h}$, can be calculated using the dimensionless coefficient, Nusselt number, given by:

$$Nu = \frac{\overline{h}\, D_h}{k_f} \tag{1.5}$$

where k_f is the fluid's thermal conductivity, and D_h is the hydraulic diameter defined as:

$$D_h = \frac{4\ \times cross - sectional\, area}{perimeter} \tag{1.6}$$

We assume that the flow is fully developed [2], thus Nu does not vary along the channel and has a constant value. We also assume that fluid properties are constant. Therefore, due to the inverse relation between the channel dimensions and the convection coefficient (Eq. 1.5), the only way to obtain significantly high convection coefficients is to use microscopic channels.

The lower limit of the channel size depends on the coolant viscosity and the pressure head of the pump. For a specific fluid, the flow rate rapidly decreases as the channel size is reduced, because of the huge increase in the pressure drop, which results in an increase in R_{flow}. To keep the flow rate constant, we should increase the power input to the pump which in turn, increases the energy consumption, noise and viscous heating in the heat-sink. Thus, we need to calculate an optimum channel size and geometry that simultaneously minimizes the sum of R_{conv} and R_{flow} as well as the pressure drop.

In cooling systems, a specific amount of heat transfer can be achieved with varying levels of irreversibility. The irreversibilities cause degradation of useful energy of the flow into internal energy, which in turn, prohibits a corresponding amount of heat from being removed by the fluid. But, only a few studies have considered the significant role of irreversibilities and the resulting entropy production in microchannel heat-sinks. In the following sections, it will be demonstrated that the second law of thermodynamics provides us with a way of

---

[2] The thermal entrance length may be expressed as, $L_{th} = 0.05 Re_{D_h} Pr D_h$. In this work, the maximum Reynolds number is 83, Prandtl number for water at room temperature is 5.83, and the hydraulic diameter is 100μm. Therefore, the maximum thermal entrance length is 2.4mm which is 12% of the channel length. Thus, the fully developed flow condition prevails.

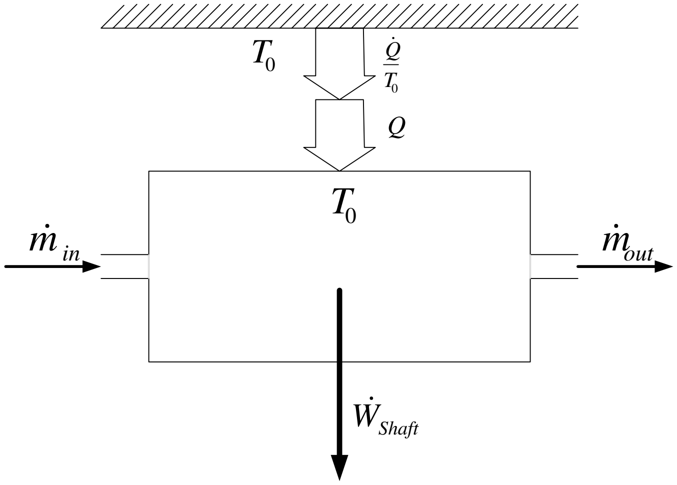

Figure 1.2: An open system in thermal contact with the atmospheric heat reservoir

optimizing fluid devices, both thermally and hydrodynamically, by minimizing the amount of entropy generation.

1.2 Theoretical Background

1.2.1 Global Rate of Entropy Generation

Consider an open system in thermal contact with the atmosphere at a temperature of T_0 (See Fig. 1.2). The rate of heat exchange between the system and the surrounding is $\dot{Q}$. The temperature of the system boundary penetrated by heat transfer is also T_0, i.e. the system boundaries are sketched in regions not affected by heat transfer.

For a general case, the first and second laws of thermodynamics are:

$$\frac{\partial E}{\partial t} = \sum_{in} \dot{m}\left(h + \frac{1}{2}V^2 + gz\right) - \sum_{out} \dot{m}\left(h + \frac{1}{2}V^2 + gz\right) + \dot{Q} - \dot{W}_{sh} \tag{1.7}$$

$$\frac{\partial S}{\partial t} \geq \sum_{in} \dot{m}s - \sum_{out} \dot{m}s + \frac{\dot{Q}}{T_0} \tag{1.8}$$

The entropy generation is defined as:

$$\dot{S}_{gen} = \frac{\partial S}{\partial t} - \sum_{in} \dot{m}s + \sum_{out} \dot{m}s - \frac{\dot{Q}}{T_0} \tag{1.9}$$

Therefore, in terms of the rate of entropy generation, the second law states:

$$\dot{S}_{gen} \geq 0 \tag{1.10}$$

In Eqs. 1.8 and 1.10, the equality is valid for reversible processes and the inequality is valid for irreversible processes. Eliminating $\dot{Q}$ between Eqs. 1.7 and 1.8 yields:

$$\dot{W}_{sh} \leq \sum_{in} \dot{m} \left(h + \frac{V^2}{2} + gz - T_0 s \right) - \sum_{out} \dot{m} \left(h + \frac{V^2}{2} + gz - T_0 s \right) - \frac{\partial}{\partial t} (E - T_0 s) \tag{1.11}$$

The right hand side of the above inequality is the theoretical upper limit for shaft power, $\dot{W}_{sh,\max}$, achieved in reversible processes,

$$\dot{W}_{sh,\max} = \sum_{in} \dot{m} \left(h + \frac{V^2}{2} + gz - T_0 s \right) - \sum_{out} \dot{m} \left(h + \frac{V^2}{2} + gz - T_0 s \right) - \frac{\partial}{\partial t} (E - T_0 s) \tag{1.12}$$

The difference between the maximum shaft power and the actual shaft power is referred to as the lost available power ($\dot{W}_{lost}$) or the rate of exergy destruction which depends on the degree of irreversibility of the system,

$$\dot{W}_{lost} = \dot{W}_{sh,max} - \dot{W}_{sh} \tag{1.13}$$

The destroyed exergy is zero for systems operating reversibly and a positive quantity for irreversible cases. By combining Eq. 1.7 and Eq. 1.9, and using Eq. 1.12, an important relationship between the lost available work and entropy generation is obtained,

$$\dot{W}_{lost} = T_0 \, \dot{S}_{gen} \tag{1.14}$$

Equation 1.14 states that the lost available work is directly proportional to the entropy generation in the device.

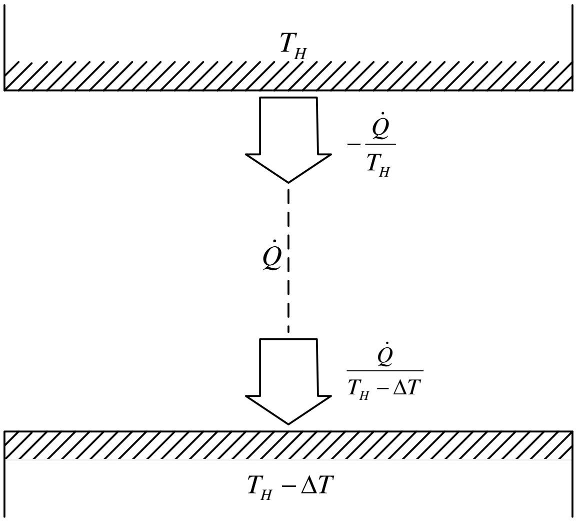

Figure 1.3: Entropy generation by heat transfer across a finite temperature difference

Improving the thermal efficiency of engineering systems requires the identification of processes causing entropy production; the two most common ones are heat transfer across a finite temperature difference and friction in the fluid flow.

- Entropy generation by heat transfer: Consider two bodies at two different temperatures, T_H and $T_H - \Delta T$, experiencing a heat transfer interaction $\dot{Q}$ (see Fig. 1.3). By applying the second law of thermodynamics to the gap between the bodies, it can be shown that the entropy generation is:

  $$\dot{S}_{gen} = \frac{\dot{Q}}{T_H - \Delta T} - \frac{\dot{Q}}{T_H} = \frac{\dot{Q}\,\Delta T}{(T_H - \Delta T)\,T_H} \tag{1.15}$$

  Assuming $\Delta T \ll T_H$ and substituting for ΔT by $\dot{Q}\,R_{th}$ (See Eq. 1.1), we obtain:

  $$\dot{S}_{gen} = \frac{\dot{Q}^2 R_{th}}{T_H^2} \tag{1.16}$$

  where R_{th} is the thermal resistance between the two bodies. Equation 1.16 implies that

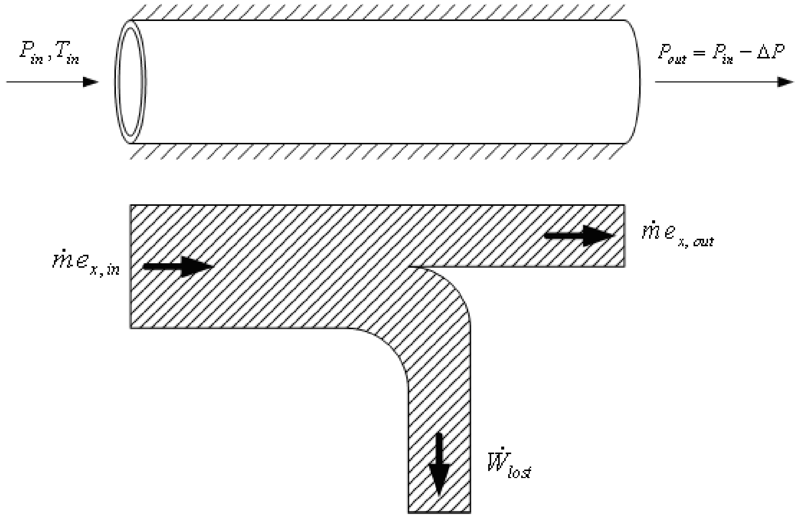

Figure 1.4: Destruction of exergy due to pressure drop in a duct

when removing a certain amount of heat from a high temperature source, the thermal resistance will be a minimum if entropy generation is minimized.

- Entropy generation by fluid friction: Another source of entropy production is fluid friction. Consider the steady and adiabatic flow of an incompressible fluid in a duct, as shown in Fig. 1.4. The pressure and temperature at the inlet are p_{in} and T_{in}, and there is a pressure drop of Δp along the pipe. The first and second laws of thermodynamics for this system state that:

$$h_{in} = h_{out} \tag{1.17}$$

and

$$\dot{S}_{gen} = \dot{m}(s_{out} - s_{in}) \tag{1.18}$$

Using the thermodynamic relation $Tds = dh - vdp$, known as Gibb's equation, and noting that $dh = 0$, we can write Eq. 1.18 as:

$$\dot{S}_{gen} = \dot{m} \left(\int_{p_{out}}^{p_{in}} \frac{v}{T} dp \right) \tag{1.19}$$

For the adiabatic flow of an incompressible fluid where $T_{out} = T_{in}$ and $v = Constant$, the entropy generation rate is directly proportional to the pressure drop along the channel through the following relationship:

$$\dot{S}_{gen} = \dot{m}\frac{\Delta p}{\rho T} \tag{1.20}$$

It is obvious that by minimizing the entropy generation rate, the pressure drop along the channel, hence the amount of useful work needed to push the fluid into the channel, is minimized.

If both sources of entropy generation, namely heat transfer and friction, are present in a fluid device, the total entropy generation rate will be:

$$\dot{S}_{gen} = \dot{m}\frac{\Delta p}{\rho T} + \frac{\dot{Q}^2 R_{th}}{T_H^2} \tag{1.21}$$

The above relationship shows that minimizing entropy production results in simultaneous minimization of thermal resistance and pressure drop in a heat- sink.

1.2.2 Local Rate of Entropy Generation

Consider an infinitesimal fluid element (dx, dy) at point (x, y) in a two- dimensional flow field, exchanging heat with the surrounding (See Fig. 1.5). Treating the fluid element as an open system subjected to mass, energy, and entropy fluxes, we can develop the following equation for the rate of entropy production per unit volume based on the second law of

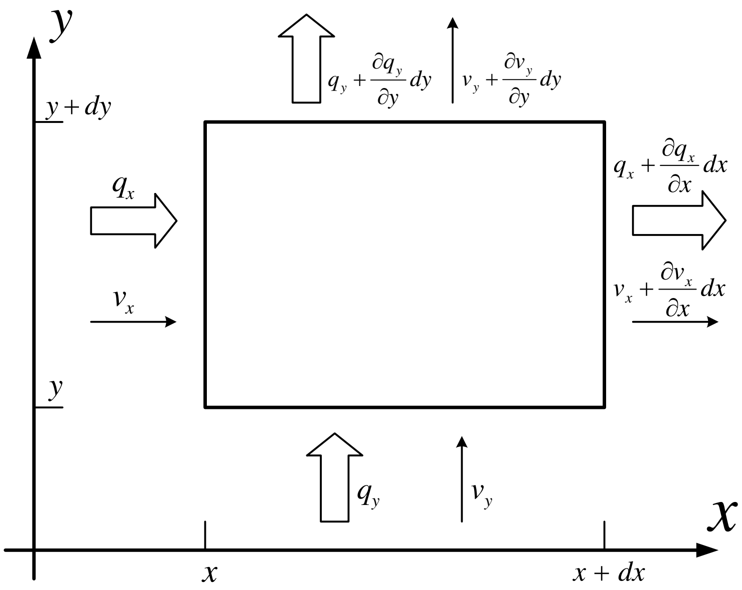

Figure 1.5: A two-dimensional infinitesimal open system subjected to heat transfer and mass flux

thermodynamics [24]:

$$
\begin{aligned}
\dot{S}'''_{gen}\, dx\, dy \quad = \quad & \frac{q_x + \dfrac{\partial q_x}{\partial x} dx}{T + \dfrac{\partial T}{\partial x} dx} dy + \frac{q_y + \dfrac{\partial q_y}{\partial y} dy}{T + \dfrac{\partial T}{\partial y} dy} dx - \frac{q_x}{T} dy - \frac{q_y}{T} dx \\
& + \left(s + \frac{\partial s}{\partial x} dx \right) \left(v_x + \frac{\partial v_x}{\partial x} dx \right) \left(\rho + \frac{\partial \rho}{\partial x} dx \right) dy \\
& + \left(s + \frac{\partial s}{\partial y} dy \right) \left(v_y + \frac{\partial v_y}{\partial y} dy \right) \left(\rho + \frac{\partial \rho}{\partial y} dy \right) dx \\
& - s\, v_x\, \rho\, dy - s\, v_y\, \rho\, dx + \frac{\partial (\rho s)}{\partial t} dx\, dy
\end{aligned}
\tag{1.22}
$$

The first four terms on the right hand side of Eq. 1.22 account for the transfer of entropy by means of heat transfer. The second four terms show the entropy transfer associated with mass flux into and out of the system, and the last term represents the accumulation of entropy inside the system with time. Dividing by $dx\,dy$ and rearranging yields:

$$\begin{aligned}\dot{S}'''_{gen} &= \frac{1}{T}\left(\frac{\partial q_x}{\partial x}+\frac{\partial q_y}{\partial y}\right)-\frac{1}{T^2}\left(q_x\frac{\partial T}{\partial x}+q_y\frac{\partial T}{\partial y}\right)+\rho\left(\frac{\partial s}{\partial t}+v_x\frac{\partial s}{\partial x}+v_y\frac{\partial s}{\partial y}\right)\\ &\quad +s\left[\frac{\partial \rho}{\partial t}+v_x\frac{\partial \rho}{\partial x}+v_y\frac{\partial \rho}{\partial y}+\rho\left(\frac{\partial v_x}{\partial x}+\frac{\partial v_y}{\partial y}\right)\right] \qquad (1.23)\end{aligned}$$

The last term in brackets is zero, based on the mass conservation principal. Equation 1.23 in vectorial form is:

$$\dot{S}'''_{gen}=\frac{1}{T}\,\nabla.\mathbf{q}-\frac{1}{T^2}\mathbf{q}\cdot\nabla T+\rho\frac{Ds}{Dt} \qquad (1.24)$$

The conservation of energy principal written for the same open system in vectorial form is:

$$\rho\frac{Du}{Dt}=-\nabla\cdot\mathbf{q}-p(\nabla\cdot\mathbf{V})+\mu\,\Phi \qquad (1.25)$$

where μ is the viscosity of the fluid, and Φ is the viscous dissipation defined as:

$$\Phi=2\left[\left(\frac{\partial v_x}{\partial x}\right)^2+\left(\frac{\partial v_y}{\partial y}\right)^2\right]+\left(\frac{\partial v_x}{\partial y}+\frac{\partial v_y}{\partial x}\right)^2 \qquad (1.26)$$

Using the substantial derivative notation, we can write the thermodynamic relation $T\,ds = du + P\,dv$ in the following form:

$$\rho\frac{Ds}{Dt}=\frac{\rho}{T}\frac{Du}{Dt}-\frac{p}{\rho T}\frac{D\rho}{Dt} \qquad (1.27)$$

eliminating Du/Dt between Eq. 1.25 and Eq. 1.27, and substituting for Ds/Dt from the result in Eq. 1.24 yields:

$$\dot{S}'''_{gen}=-\frac{1}{T^2}(\mathbf{q}\cdot\nabla T)+\frac{\mu}{T}\,\Phi \qquad (1.28)$$

by substituting for $\mathbf{q}$ in Eq. 1.28 using Fourier's law of heat conduction, $\mathbf{q} = -\,k\,\nabla T$, a relationship for the volumetric rate of entropy production in terms of measurable quantities, namely temperature and velocity is obtained:

$$\dot{S}'''_{gen}=\frac{k}{T^2}(\nabla T)^2+\frac{\mu}{T}\,\Phi \qquad (1.29)$$

for a two-dimensional Cartesian system:

$$\dot{S}'''_{gen} = \frac{k}{T^2}\left[\left(\frac{\partial T}{\partial x}\right)^2 + \left(\frac{\partial T}{\partial y}\right)^2\right] + \frac{\mu}{T}\left\{2\left[\left(\frac{\partial v_x}{\partial x}\right)^2 + \left(\frac{\partial v_y}{\partial y}\right)^2\right] + \left(\frac{\partial v_x}{\partial y} + \frac{\partial v_y}{\partial x}\right)^2\right\} \tag{1.30}$$

1.3 Principles of Micro Particle Image Velocimetry

Particle image velocimetry is an optical technique for measuring velocities in fluid flows [25]. The flow is seeded with small particles whose motion is used to calculate flow velocities. A micro-PIV system is composed of a double-pulsed laser to illuminate the test section, a digital camera to detect the light scattered by particles, a microscope to magnify the submicron particles, an optical fiber to transfer illumination light from laser to microscope, and a computer for processing. In order to measure velocity, at least two exposures are needed, that can be recorded on one or more frames.

There are two main methods for extracting velocity data from images, namely PMV (Pattern Matching Velocimetry) and PTV (Particle Tracking Velocimetry). In PMV, the method used in this work, the frames are divided into smaller regions called interrogation areas. A displacement vector is calculated for each interrogation area by correlating the patterns of particles in the two frames. The correlation process used in this study is a two-frame cross-correlation process. It uses two image frames with one laser pulse on each frame. There is a known time delay between the frames, governed by the delay between the laser pulses. The camera is synchronized with the laser to initiate images right before the laser pulses. Velocity is then obtained by dividing the distance particles have traveled from frame 1 to frame 2 by the time delay. A full field of velocity data is acquired by compiling all the interrogation areas.

In the PTV method, however, the individual particles are tracked, not the overall pattern; therefore, the resolution is significantly increased. In PMV approximately 5 to 20 particles are needed in each interrogation area to produce a vector. It means that in principle, PTV should produce 5 to 20 times more vectors than PMV; but these vectors will be randomly located in the measurement field.

In regular PIV[3] used in macroscopic devices, a thin light sheet is formed to illuminate the flow field and only the image of the illuminated particles located in the light sheet is recorded by the camera; but such a process is not applicable to micro-PIV; because of the lack of optical access and significant diffraction in light sheet forming optics. Instead, epiflourescent[4] microcopy technique is used in which the whole volume of the test section illuminated (see Chapter 4 for more details.).

1.4 Principles of Micro Laser Induced Fluorescence

Laser Induced Fluorescence is another optical diagnostic method, mostly used for the measurement of temperature and concentration [26]. Fluorescence is a process in which molecules excited by electromagnetic radiation emit a photon in a three stage process. First, a photon is absorbed by the fluorophore and its energy level is increased. Second, the fluorophore remains in its excited state for a finite time (typically between 1 to 10 ns) called fluorescent lifetime. Third, a photon is released and the energy level returns to the ground state. Because of the dissipation of energy, the emitted photon is of lower energy and longer wavelength compared to the excitation photon. Some fluorescent dyes exhibit a high temperature dependant fluorescent emission which makes them suitable for laser-based micro-scale temperature measurement.

The fluorescent intensity per unit volume of an organic fluorescent dye is:

$$I = I_o C \, \phi \, \alpha \tag{1.31}$$

---

[3] PIV is one category of the more general PMV method.

[4] Epifluorescent microscopy means that the illumination of the test section and imaging the fluorescent particles are done through the same optical axis.

where I_o is the incident light intensity, C is the concentration of the dye, α is the absorption coefficient (weakly dependant on temperature), and ϕ is the temperature dependant quantum efficiency. If I_o and C are kept constant, one can measure the temperature of a fluorescent dye solution through variations of fluorescent intensity associated with temperature dependence of ϕ. It should be noted that an accurate calibration curve is required before doing the measurements to correlate the intensity with temperature. Although the constant concentration of the dye can be maintained, it is impossible to maintain a constant illumination intensity (the intensity of the illumination light is never distributed uniformly in the incident laser beam); therefore, the variations in fluorescent intensity represents not only the variations in temperature, but also the variations in incident light flux. Hence, there is always some level of error associated with this method of temperature measurement.

1.5 Problem Statement

It is desired to calculate the entropy production rate at the inlet and exit of a single rectangular microchannel, with different geometries, and determine which one produces the smallest amount of entropy. Three geometries for entrance and exit have been selected in this study, namely rectangular, triangular, and circular. The channels are 100 μm wide and 2 cm long, preceded by a 200 μm wide and 1 cm long section to ensure parallel and disturbance free flow. The depth of the microchannels is 100 μm. The volume flow rate ranges from 100 $\mu l/min$ to 500 $\mu l/min$, resulting in an average velocity of 0.17 m/s to 0.83 m/s. A schematic of the microchannels under study in this work is sketched in Figs. 1.6 and 1.7.

In addition to experimental measurements, a global analytical model for the entropy generation rate in the microchannels is needed to predict the total amount of entropy generated in the flow. The model should be able to account for the different aspect ratios and entrance/exit geometries as well as any irregularities in the cross-sectional shape of the

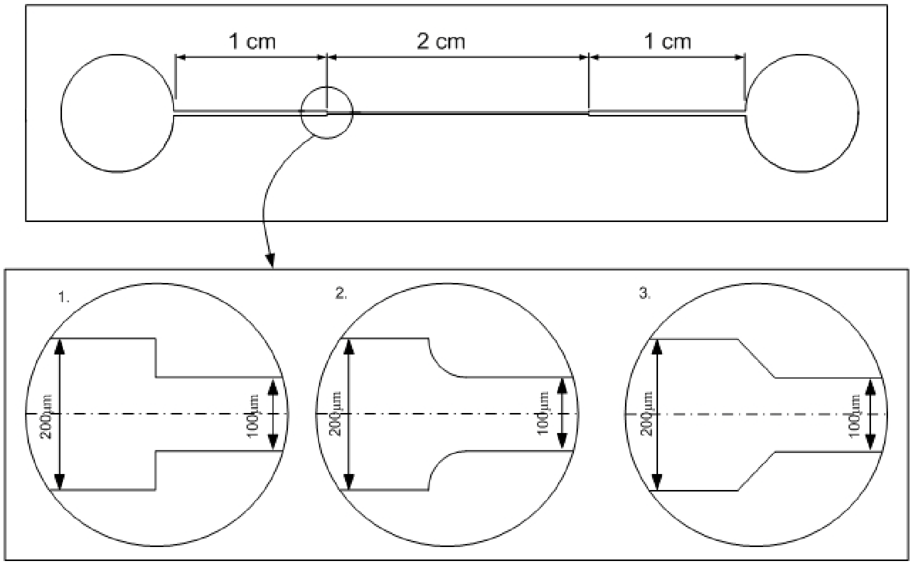

Figure 1.6: Schematic of the microchannels under study

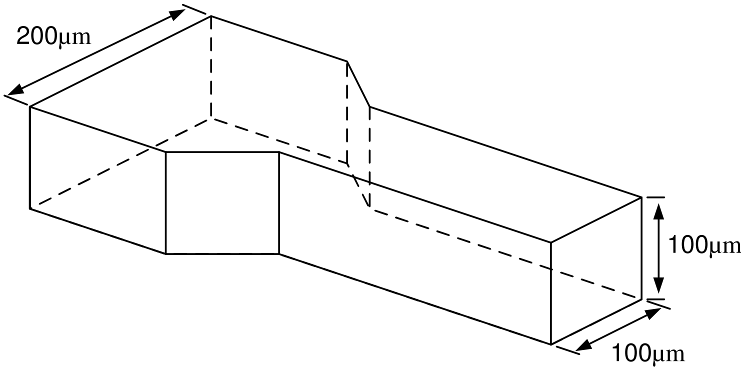

Figure 1.7: Three dimensional schematic of the microchannel exit with triangular shoulder

channels[5].

The Reynolds number is defined as:

$$Re = \frac{\rho U_{ave} D_h}{\mu} \tag{1.32}$$

which in this work varies between 16.6 and 82.9. In this range, the flow is essentially laminar and the entrance length of the flow is determined by the following relationship:

$$L_{ent} = 0.05 \;\; Re\, D_h \tag{1.33}$$

For the range of Reynolds numbers encountered in this work, the entrance length is between 83 μm and 415 μm.

1.6 Approach

In this study, a non-intrusive laser-based technique for the measurement of entropy production in microchannels has been introduced. With conventional techniques, the destruction of exergy can be calculated on a global scale; but in the measurement method used in this work, irreversibilities can be detected locally, allowing the engineers to target and modify problem areas characterized by high entropy production rates, so that the device can reach its upper limits of performance imposed by the second law. The entropy production data are used to determine the optimum heat-sink geometry at inlet and exit sections of the channels, leading to minimum entropy production and exergy loss. As demonstrated earlier in Eq. 1.30, entropy production can be measured indirectly from spatial gradients of velocity and temperature. The use of Micro Particle Image Velocimetry (micro-PIV) and Micro Laser Induced Fluorescence (micro-LIF) methods allows for non-intrusive, full field, and time varying measurement of velocity and temperature. In PIV and LIF methods, the velocities

---

[5] Due to the fabrication constraints (see Chapter 4), the side walls of the channels are not completely vertical and the channel cross-sectional geometry is slightly nonuniform along the channel.

and temperatures are given over a discrete grid. By spatial differencing Eq. 1.30 over such a discrete grid, local rates of entropy production can be determined. The discretized form of Eq. 1.30 is [11]:

$$\begin{aligned}\dot{S}'''_{gen} &= \frac{k}{T(i,j)^2}\left(\frac{T(i+1,j)-T(i-1,j)}{\Delta x}\right)^2 \\ &+\frac{k}{T(i,j)^2}\left(\frac{T(i,j+1)-T(i,j-1)}{\Delta y}\right)^2 \\ &+2\frac{\mu}{T(i,j)}\left(\frac{u(i+1,j)-u(i-1,j)}{\Delta x}\right)^2 \\ &+2\frac{\mu}{T(i,j)}\left(\frac{v(i,j+1)-v(i,j-1)}{\Delta y}\right)^2 \\ &+\frac{\mu}{T(i,j)}\left(\frac{u(i,j+1)-u(i,j-1)}{\Delta y}+\frac{v(i+1,j)-v(i-1,j)}{\Delta x}\right)^2 \qquad (1.34)\end{aligned}$$

where Δx and Δy are twice the grid spacing in x and y directions, respectively. By substituting the measured temperatures and velocities in Eq. 1.34, the value of entropy production rate at the desired location is obtained.

Chapter 2

Literature Review

The performance of microchannel heat-sinks has been the subject of many published works; But, only a few of them adopted the second law approach to the problem. The literature reviewed in this chapter are divided into four categories. The first category is the literature related to the modeling of entropy generation in microchannels. There are a few works done on the modeling of entropy generation in micro-devices and the majority of studies related to entropy production are at the macro-scale. The second and third categories are the measurement of velocity and temperature with micro-PIV and micro-LIF methods, respectively. Since the advent of these new technique in 1998, many researchers have implemented them in studying various micro-scale fluid phenomenon. Here, the leading works on this subject will be reviewed. The fourth category involves the experimental measurements of entropy production in thermo-fluid devices, using the PIV and LIF methods. No previous experimental measurement of entropy in micro-scale has been done (to the knowledge of this author), but the measurements done in macro-scale will be described in this chapter.

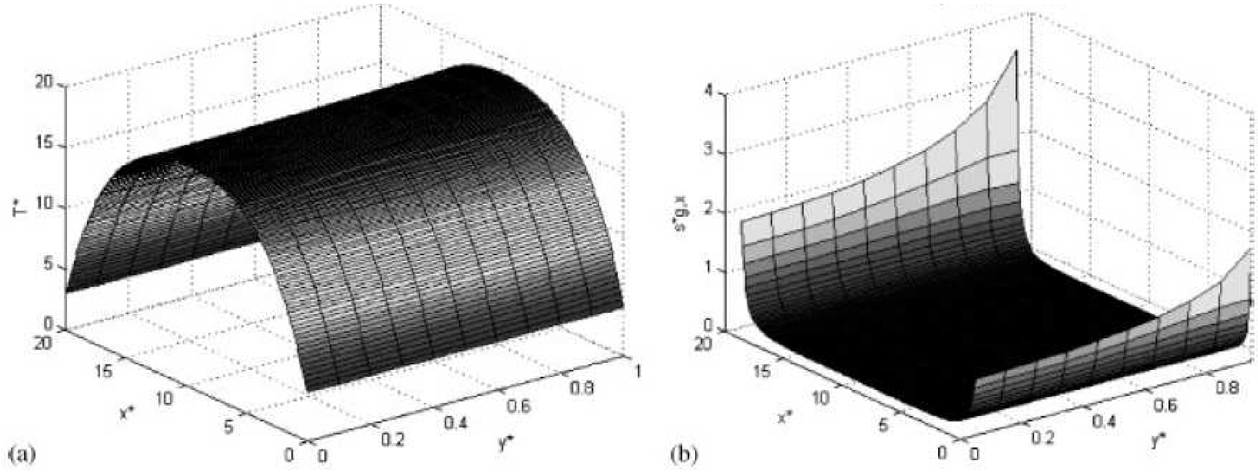

Figure 2.1: Finite difference results of temperature distribution (a) and entropy generation in a microchannel [5]

2.1 Modeling

Chen [5] calculated and analyzed the generation and transfer of entropy in microchannels for different thermal boundary conditions. In his work, the lateral temperature gradients have been neglected, due to the small flow cross-sectional area, and a laterally lumped model has been developed. Heat conduction in the flow direction has been taken into account due to the low Peclet number of the flow. They concluded that the local entropy generation rates are only dependant on the temperature gradient in the flow direction. They simultaneously solved the following equations to determine the local rates of entropy production:

$$\text{energy equation:} \qquad \rho c V \frac{\partial T}{\partial x} = k \frac{\partial^2 T}{\partial x^2} + \frac{\dot{Q}}{A} \tag{2.1}$$

$$\text{temperature distribution:} \qquad \frac{\partial^2 T}{\partial x^2} + \frac{\partial^2 T}{\partial y^2} = 0 \tag{2.2}$$

$$\text{entropy generation:} \qquad \dot{S}_{gen} = \frac{k}{T^2}\left[\left(\frac{\partial T}{\partial x}\right)^2 + \left(\frac{\partial T}{\partial y}\right)^2\right] \tag{2.3}$$

The frictional effects have been neglected in this work, because of the typically low velocities in micro-devices. Figure 2.1 shows the temperature and entropy generation distribution in an arbitrary plane in a micro-channel.

The significant shortcoming of this study is neglecting the lateral temperature gradients and frictional effects in the analysis. Because of the very small cross-sectional dimensions of the microchannels, the lateral temperature gradients and velocity gradients, which are directly proportional to frictional effects, would be huge and must be taken into account.

In another work, Khan et. al.[6] developed a general expression to predict the entropy generation rate in a microchannel heat-sink by considering the combined effects of heat transfer and pressure drop. Their model includes the effects of channel aspect ratio, fin spacing, heat-sink material, Knudsen number, and accommodation coefficient on the entropy generation rate in the slip flow regime. They employed analytical/numerical correlations for the pressure drop and heat transfer in microchannels, with the hydraulic diameter used as the characteristic length. They have used a fin approach to develop a model for the thermal resistance, assuming adiabatic fin tips (see Fig. 2.2). For the pressure drop, they have used the correlations developed for conventional large channels. The restrictions of their model are that it is limited to a uniform heat flux boundary condition, rectangular channels, and hydrodynamically and thermally fully developed flows. They concluded that increasing the flow rate decreases the thermal resistance and increases the pressure drop. The results of their work also show that the optimum channel aspect ratio increases with volumetric flow rate.

Abbassi [27] analytically investigated the problem of entropy generation in a uniformly heated microchannel. A porous medium approach, based on Darcy's equation for fluid flow and the Two Equation Model for heat transfer, was used in their work to solve the forced convection problem. The closed form velocity solution in rectangular channels (see Sec. 3.1) is employed to capture viscous effects. A second law analysis was then conducted using an

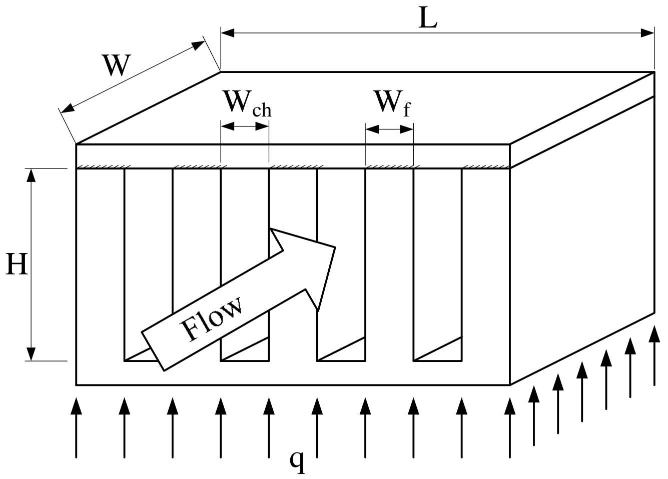

Figure 2.2: The microchannel heat-sink under study in [6]

analytical velocity profile and temperature distribution. This work concludes that entropy generation has an optimum value for aspect ratio; whereas thermal entropy generation decreases and pressure drop rises with increasing aspect ratio. The effect of other parameters like fluid and heat-sink material conductivities, Brinkmann number, and porosity are also discussed in this work. The model of Abbassi is limited to rectangular channels and works for the thermally and hydraulically fully developed flows only.

Erbay et al.[28] numerically studied the entropy generation in parallel plate microchannels induced by transient laminar forced convection in the combined entrance region. The differential continuity, Navier-Stokes, energy, and second law equations are simultaneously solved with a SIMPLE algorithm in the two-dimensional unsteady and developing laminar flow regime of a viscous fluid with constant thermophysical properties. These equations are as follows:

$$
\begin{aligned}
0 &= \frac{\partial \rho}{\partial \tau} + \nabla \rho \overrightarrow{V} && (2.4)\\
\rho \frac{D\overrightarrow{V}}{D\tau} &= -\nabla p + \frac{1}{Re}\nabla^2 \overrightarrow{V} && (2.5)\\
\frac{DT}{D\tau} &= \frac{1}{Re\,Pr}\nabla^2 T && (2.6)\\
\dot{S}_{gen} &= \nabla^2 T + \Theta \left\{ 2\left[\left(\frac{\partial u}{\partial x}\right)^2 + \left(\frac{\partial u}{\partial y}\right)^2 \right] + \left(\frac{\partial u}{\partial y} + \frac{\partial v}{\partial x}\right)^2 \right\} && (2.7)
\end{aligned}
$$

where Θ is an entropy distribution ratio. The strong effects of aspect ratio, Reynolds number, Prandtl number, and Brinkmann number on the entropy generation have been addressed in this work. They concluded that the entropy generation is maximum for the most slender channels.

Many of the models developed for predicting entropy production in microchannels are restricted to fully developed flows. However, the length of the microchannel heat-sinks is relatively low and the flow inside them is often in the developing regime. This fact necessitates the development of a model that accounts for developing flow effects. Moreover, all of the above models are limited to rectangular cross-sections. However, it is difficult in practice to make channels with completely vertical side walls, and developing a model for a wide range of geometries is essential. Moreover, none of the previous studies, considered the effect of entrance and exit losses on entropy generation in fluid devices.

2.2 Velocity Measurement

The Micron Resolution Particle Image Velocimetry System was developed by Santiago et al.[7] in 1998 to measure the instantaneous local velocity distribution in micro-scale fluidic systems. The system utilized an epifluorescent microscope, a continuous Hg-Arc lamp, 100-

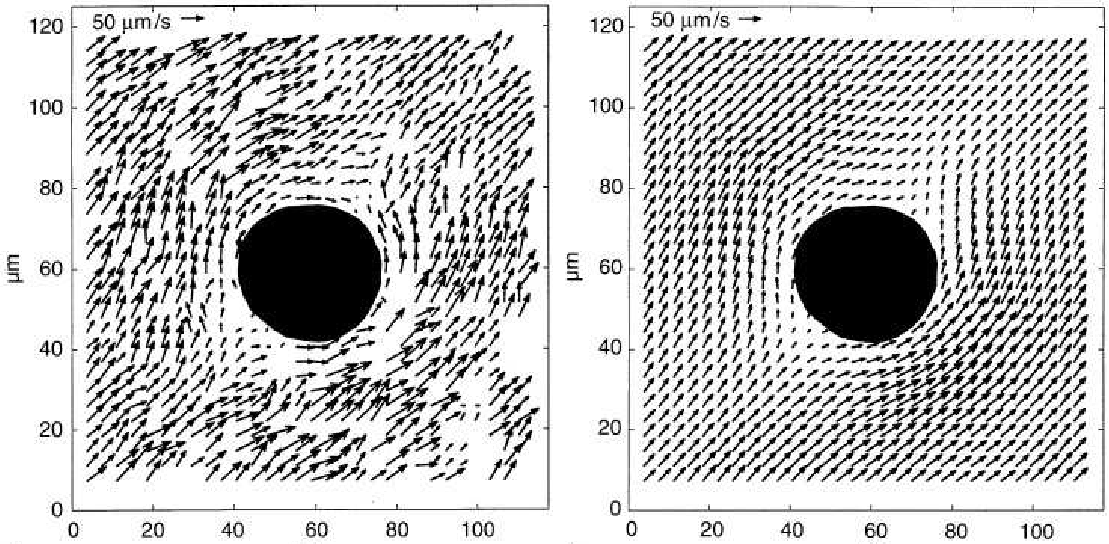

Figure 2.3: Vector fields of a surface tension driven Hele-Shaw flow around a $30\mu m$ diameter obstacle. (a) instantaneous velocity vector field. (b) eight image ensemble averaged vector field [7]

300 nm fluorescently tagged particles, and an intensified CCD camera. They applied this new technique to measure the velocity field in a Hele-Shaw flow around an elliptical cylinder with a major diameter of roughly $30\,\mu m$ and a bulk flow velocity of $50\,\mu m/s$. The resolution of their measurements was $6.9 \times 6.9 \times 1.5\,\mu m$. The images were processed with a double-frame cross-correlation method. They established a Hele-Shaw flow by placing a drop of surfactanted deionized water seeded with $300\,nm$ particles between a frosted microscope slide and a $170\,\mu m$ thick clear cover-glass. The evaporation and wicking of water at the exposed regions of the frosted glass generates a relatively steady flow field in the drop. The Reynolds number of the flow was about 3×10^{-4}. Figure 2.3 shows an instantaneous velocity vector field and a vector field resulting from ensemble averaging several image pairs. The CCD array was exposed for $\delta t = 2\,ms$, and the time delay between exposures was $\Delta t = 68.5\,ms$.

The experimental setup of Santiago et. al. is well suited for situations where high resolutions and low light levels are required. The minimum exposure time required for the camera to record the particle images is in the order of several milliseconds, and the time delay between image pairs is tens of milliseconds. The large time intervals limit this PIV system to low velocity applications.

Meinhart et. al.[8] devised an alternative approach in which an Nd:YAG laser with pulses of $5\,ns$ duration and $1\,mJ$ of energy is the illumination source. The camera used in their study is capable of taking back to back images with a time spacing of $500\,ns$. Meinhart used this system to measure the velocity profile inside a $30\mu m \times 300\mu m \times 25mm$ glass microchannel. The flow rate in the channel was $200\,\mu l/h$, producing a maximum velocity of almost $10\,mm/s$ in the channel. They analyzed their images with a higher spatial resolution (120 × 8 pixels) near the wall where the velocity gradients are higher and with a lower resolution (120 × 40 pixels) away from the wall. With the use of an oil immersion lens, they managed to get velocity vector data in a $450\,nm$ distance from the wall. The resulting PIV measurements agree to within 2% of the analytical solution. An ensemble averaged velocity field and the comparison of the measured profile with analytical profile is shown in Fig. 2.4.

2.3 Temperature Measurement

Ross et. al.[29] described a technique for the measurement of fluid temperature in microfluidic systems based on temperature-dependant fluorescence. They verified the applicability of their method by measuring the temperature distribution resulting from the Joule heating in a variety of electrokinetically pumped circuits. They measured temperatures ranging from room temperature to $90°C$ with an accuracy of 0.03 to $3.5°C$, depending on the amount of signal averaging done. They managed to achieve a spatial resolution of $1\,\mu m$ and a temporal resolution of $33\,ms$. Their temperature indicator was Laser Grade Rhodamine B. Rhodamine B solution (0.1 mM/l) was prepared in the carbonate buffer and filtered with a $0.2\,\mu m$ pore sized filter. Microchannels were fabricated using PMMA, PDMS, and Fused Silica. Their

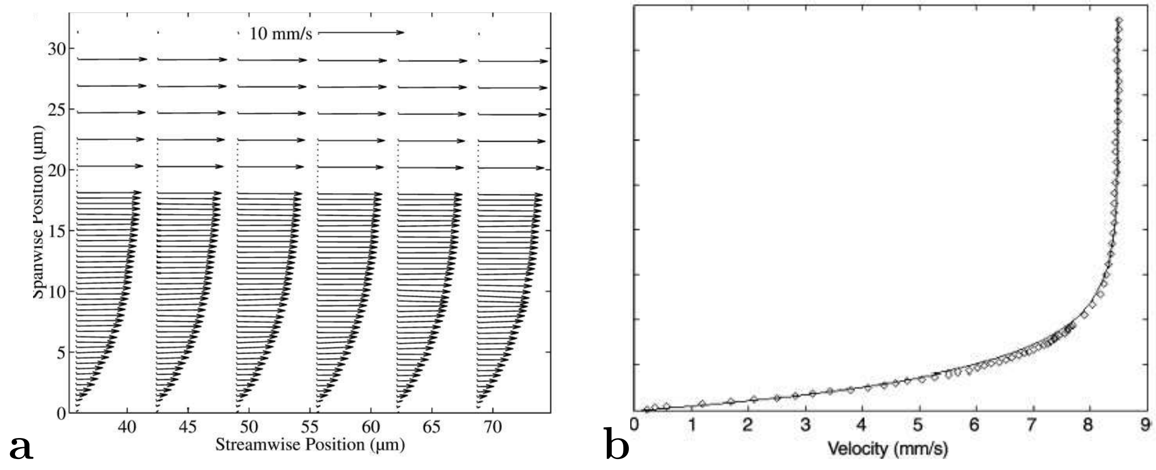

Figure 2.4: (a) A near wall view of ensemble-averaged vector field in a rectangular microchannel. (b) Ensemble-averaged velocity profile in the rectangular microchannel compared with the analytical profile [8]

image acquisition system was composed of a research fluorescent microscope equipped with a 20× objective, Hg-Arc lamp, appropriate filter sets, and a video camera.

Fu et. al.[9] described a micro-heater design for micro-fluidic devices made by embedding a resistance wire into a PDMS chip and the measurement of fluid temperature in the chip. Rhodamine B was used to measure the temperature distribution within the fluid. Two heater configurations were tested (see Fig. 2.5), a point heater to provide localized thermal control and a linear heater to provide a uniform temperature field over the channel length, and the results were compared to numerical simulations. The results of this study agree very well with the numerical predictions within $\pm 2°C$.

In another study, Yamaguchi et. al.[10] implemented a two color Laser Induced Fluorescence technique to measure the temperatures in micro-scale with very high accuracy ($1.0\%/K$). The temperature indicator is a 3:1 mixture of a temperature sensitive dye (Rhodamine B) and a temperature insensitive dye (Nile Red) in ethanol. The fluorescence inten-

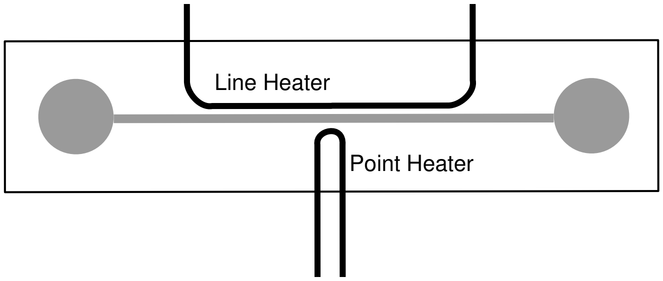

Figure 2.5: A schematic of the micro-heaters implemented inside a microchannel [9]

sity of the temperature sensitive dye is proportional to temperature as well as the illumination intensity according to the following relationship:

$$I = I_0 \, C \, \phi \, \alpha \tag{2.8}$$

where I_0 is the illumination intensity, C is the concentration of the dye, ϕ is the temperature dependant quantum efficiency, and α is the temperature insensitive absorption coefficient. The measurements will be biased if there are variations in illumination intensity.

Variations of the illumination light has been accounted for by measuring the local instantaneous intensity of the illumination light. Such a measurement is done by adding a second fluorescent dye whose quantum efficiency has no or very little dependence on temperature and imaging it separately. If the emissions of the two dyes are separated perfectly and recorded by two different cameras, the ratio of their emission can be expressed as:

$$\frac{I_A}{I_B} = \frac{I_0 \, C_A \, \phi_A \, \alpha_A}{I_0 \, C_B \, \phi_B \, \alpha_B} \tag{2.9}$$

This ratio is independent of illumination intensity, I_0, but depends on temperature via ϕ_A/ϕ_B. A schematic of the optical setup for separating the emissions of the two dyes is shown in Fig. 2.6.

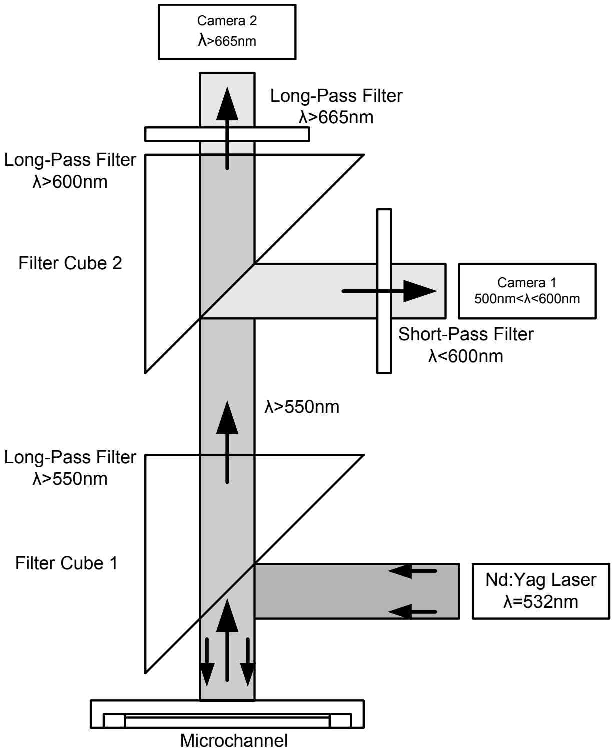

Figure 2.6: A schematic of the filter cubes arrangement in the two dye LIF system [10]

2.4 Entropy Generation Measurement

The experimental measurement of local entropy generation using the Particle Image Velocimetry and Laser Induced Fluorescence systems was successfully done by Naterer and Adeyinka in two macro-scale fluid systems.

Adeyinka and Naterer[11] determined the local entropy production rates within a flow driven by natural convection in a $39mm \times 39mm \times 59mm$ enclosure. Their experimental method involves the use of Particle Image Velocimetry and Planar Laser Induced Fluorescence techniques for the measurement of velocity and temperature components of entropy generation, respectively. The have shown that there is complete agreement between the measured and predicted entropy generation rates.

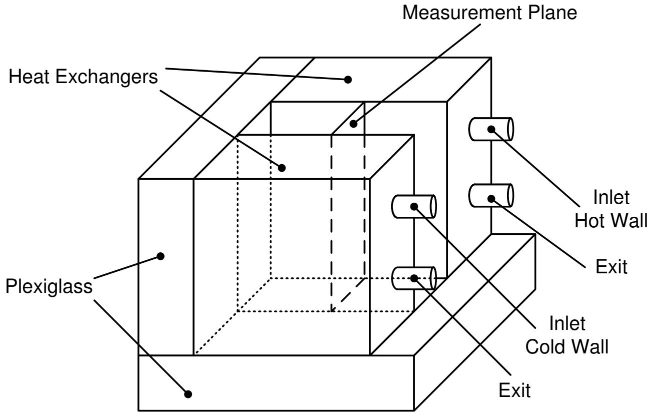

Figure 2.7: The test cell used in Ref. [11] for measuring the entropy generation rate

They measured the flow irreversibilities indirectly from the spatial gradient of velocity and temperature, using the discretized form of the following equation (see Sec. 1.6):

$$\dot{S}_{gen} = \frac{k}{T^2}\left(\frac{\partial T}{\partial x_j}\frac{\partial T}{\partial x_j}\right) + \frac{\mu\,\Phi}{T} \tag{2.10}$$

where Φ is the viscous dissipation arising from velocity gradients in the fluid motion. Their test cell was assembled with front, back, top, and bottom Plexiglas walls and heat exchangers on the right and left sides to control the temperature of the fluid (see Fig. 2.7). Their system configuration consisted of an Nd:YAG pulsed laser, light sheet forming optics, $5\,\mu m$ Polyamide tracer particles, Rhodamine B fluorescent dye for LIF, and a $30Hz$, 1280×1024 pixels CCD camera. The image capturing system detected the particles and the fluorescent dye at two different instants. A long pass optical filter attached in front of the camera separated the long wavelength fluorescent light of Rhodamine B from the laser light reflected by the particles. The Rayleigh number of the flow was controlled by adjusting the fluid temperature inside the heat exchangers. The depth of the test cell ($59mm$) was designed to minimize the error caused by the heat loss from the front and back walls of the test cell. Water at known temperature was circulated inside the heat exchangers from two constant

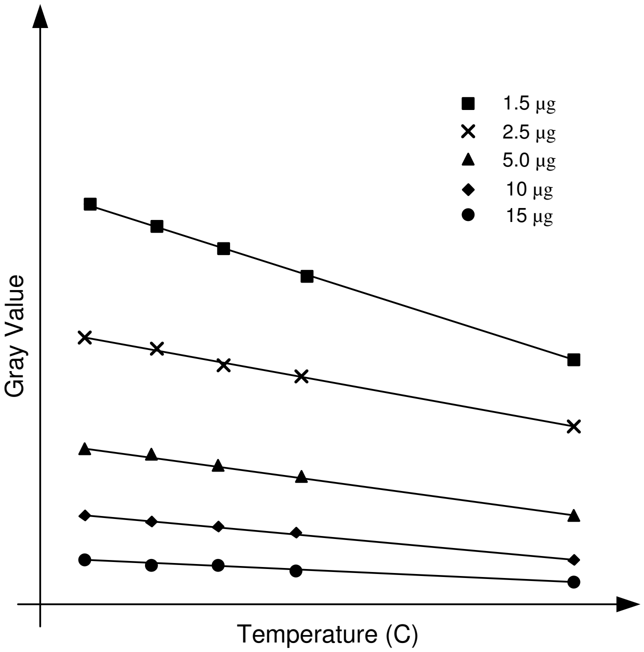

Figure 2.8: Gray values in LIF measurements at different concentrations [11]

temperature baths. They found that the optimum concentration, resulting in the maximum LIF resolution[1], is $15\mu g/L$. The gray values versus temperatures for different concentrations are shown in Fig. 2.8. A single camera was used to record both LIF and PIV images. The 1280 × 1024 pixels image plane was divided into 32 × 32 pixels interrogation regions with a 50% overlap, resulting in a spatial resolution of $0.1\,mm$. The measured velocities could not be obtained within a $0.2\,mm$ distance from the walls. The total measurement uncertainty of the velocity measurements was about 0.5%. Figure 2.9 shows the symmetric velocity distribution and constant temperature contours in the cavity at a Rayleigh number of 1000. A surface plot of the measured velocity and entropy generation in the test cell is shown in Figs. 2.10 a and b. The results show that there is close agreement between the predicted and measured results. The irreversibilities occur predominantly near the side-walls; also the

---

[1] The spatial gradient of gray value with temperature represents the LIF resolution.

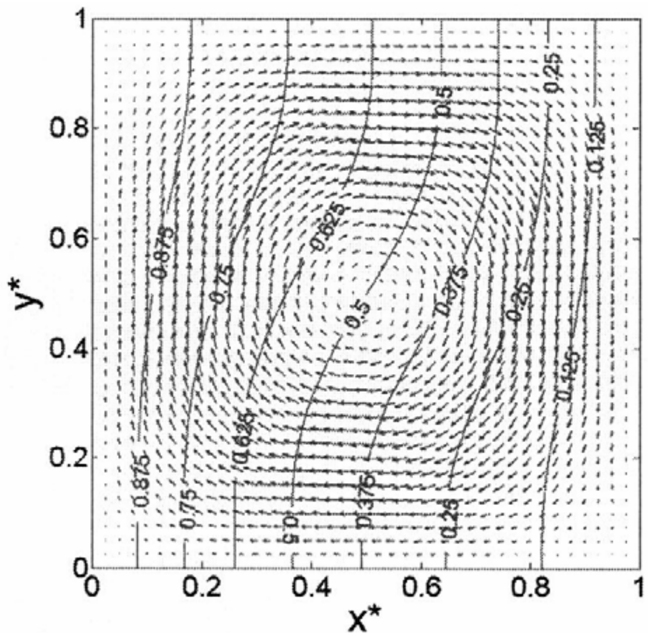

Figure 2.9: Temperature and velocity distribution in the free convection driven flow [11]

maximum entropy generation occurs near the center point along the sidewalls, where the velocities and their gradients are highest. The experimental and predicted velocities agree very well except close to the walls, due to certain limitations of the PIV technology.

In another work[12], Naterer and Adeyinka measured the instantaneous rate of entropy generation in a magnetic stirrer inside a cuvette cube with dimensions of $60\,mm \times 60\,mm \times 60\,mm$. The cube is filled with water and set on a stand where a magnetic field causes the stir bars to spin at $90\,RPM$. They focused only on frictional effects which causes the irreversible degradation of mechanical energy into internal energy through viscous dissipation. Figures 2.11 a and b show the velocity vector field and the entropy production in a plane $5\,mm$ below the free surface of the fluid in the cube. As expected, the regions of high mixing at the center of the flow yield the highest rates of entropy production.

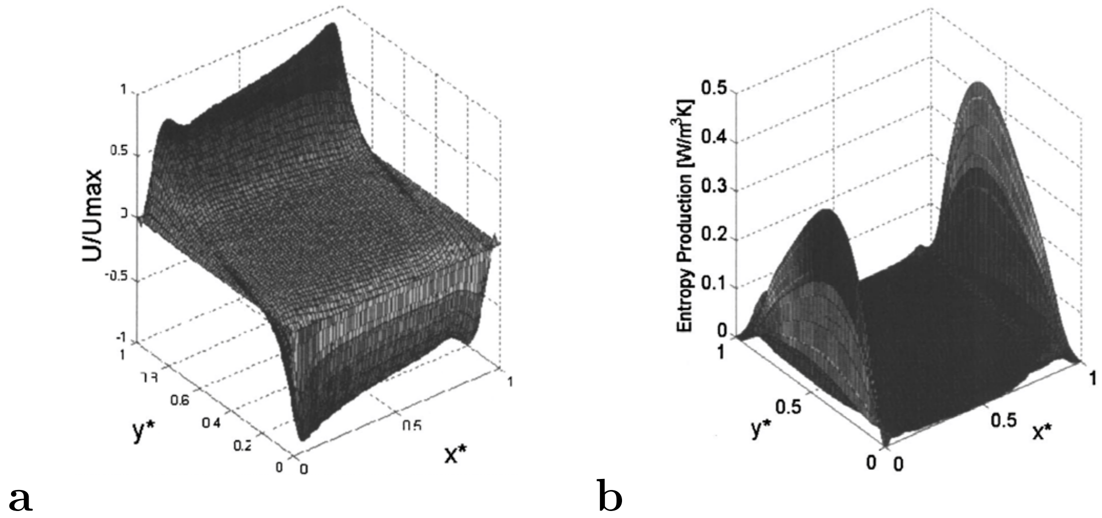

Figure 2.10: Measured velocity (a) and entropy generation (b) distribution in the free convection flow [11]

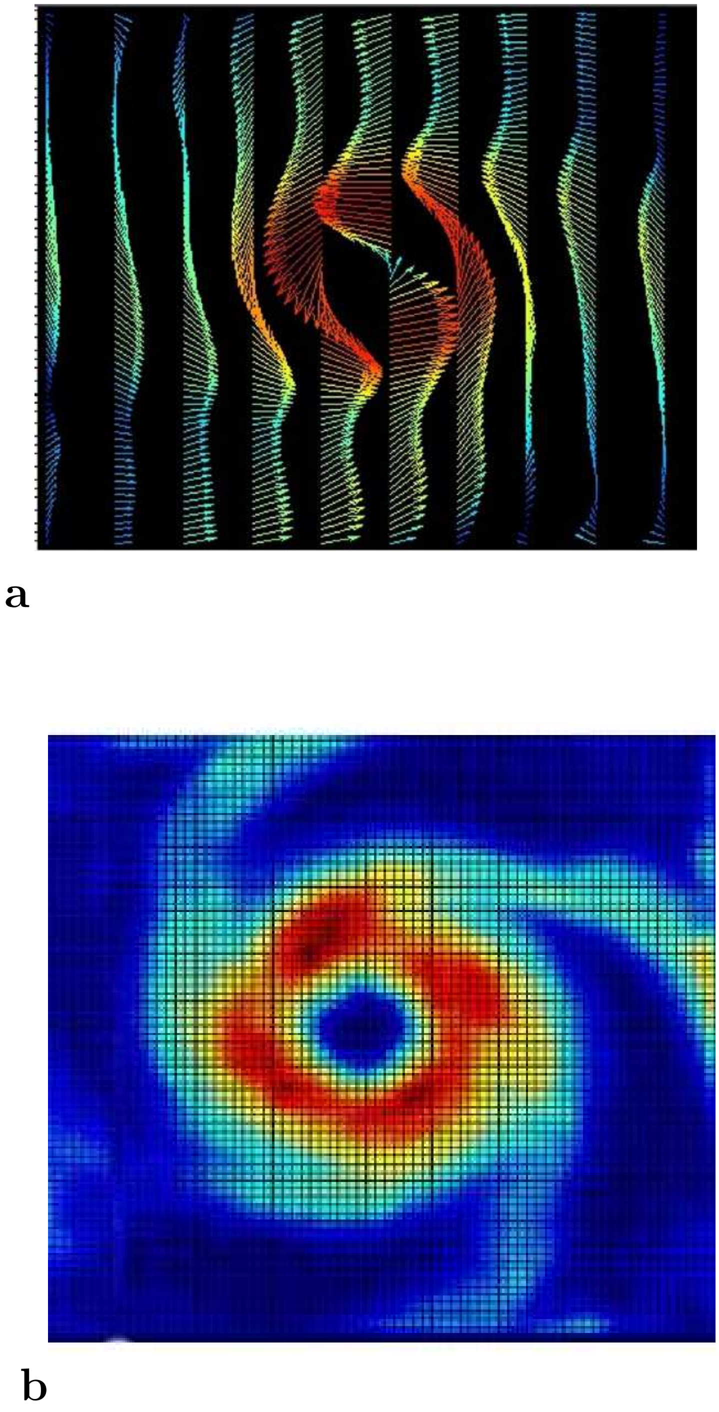

Figure 2.11: Velocity field and contours of entropy generation in a magnetic stirrer [12]

Chapter 3

Modeling

As stated in the previous chapter, certain limitations of the current models for prediction of entropy generation in micro-devices necessitate the development of more accurate models. These limitation are: not accounting for developing flow effects, irregularities in cross-sectional shape, restrictions on thermal boundary condition, and not considering entrance and exit losses. The goal of this chapter is to describe the development of a general model to determine the entropy generation of liquid flows in microchannels.

The model developed in this work is based on Muzychka's model [2] for pressure drop and heat transfer in channels. The details of the models developed by Muzychka for friction factor and Nusselt number are discussed. These models are valid in thermally and hydrodynamically, fully developed and developing flows as well as with various thermal boundary conditions. The models are applicable to a wide range of cross-sectional geometries, including the rectangular channels, which are used in this work. The development of the models is based on the theories for conventional channels, i.e. the Navier-Stokes equations and the no slip boundary condition, which may not be valid in microscopic devices. Therefore, it is uncertain whether the model of Muzychka is applicable to microchannels under study in this work. The experimental data available in the literature for friction factor and Nusselt number in microchannels have been compared to the results of the models. The excellent agreement between the data and the models shows that the macroscopic channel theories are still valid in micro-scale for liquid flows. Analytical expressions for predicting pressure drop in the entrance and exit of the channel are also developed. The results of the model will be compared to the measurement results in Chapter 5.

3.1 Velocity Profile

Consider the incompressible and pressure-driven flow in a straight duct of arbitrary but constant cross section (see Fig. 3.1). In the fully developed region, the velocity is purely axial and varies only with the lateral coordinates, i.e. $u = u(x, y)$ and $v = w = 0$. The differential continuity and momentum equations for this flow are:

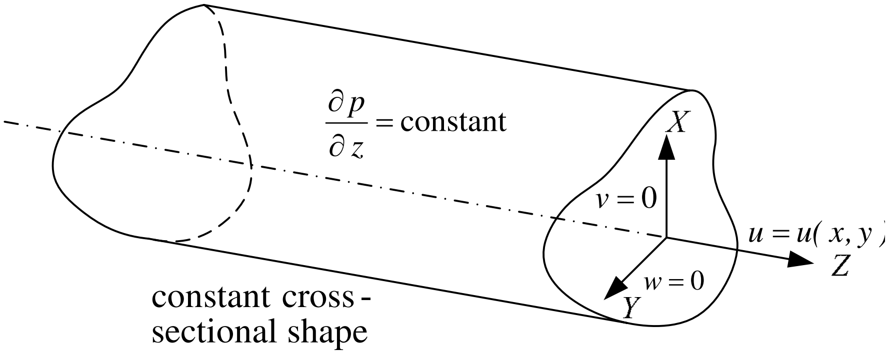

Figure 3.1: Schematic of a fully developed duct flow in a channel of arbitrary cross-section

$$\frac{\partial u}{\partial z} = 0 \tag{3.1}$$

$$-\frac{\partial p}{\partial z} + \mu \left(\frac{\partial^2 u}{\partial x^2} + \frac{\partial^2 u}{\partial y^2} \right) = 0 \tag{3.2}$$

$$-\frac{\partial p}{\partial x} = -\frac{\partial p}{\partial y} = 0 \tag{3.3}$$

The above equations indicate that p is a function of z only and u is a function of x and y. Thus the basic equation for fully developed duct flow will be:

$$\frac{\partial^2 u}{\partial x^2} + \frac{\partial^2 u}{\partial y^2} = \frac{1}{\mu}\frac{\partial p}{\partial z} = \text{constant} \tag{3.4}$$

subjected to a no slip condition on the walls, $u_w = 0$. Since Eq. 3.4 is a classic Dirichlet problem, a large number of exact solutions have been developed for non-circular duct shapes. The solution for the rectangular cross-section is [14]:

$$\begin{aligned} -a &\leq y \leq a\,,\ -b \leq z \leq b \\ u(x,y) &= \frac{16a^2}{\mu\pi^3}\left(-\frac{dp}{dx}\right)\sum_{i=1,3,5,\ldots}^{\infty}(-1)^{\frac{i-1}{2}}\left[1-\frac{\cosh(i\pi z/2a)}{\cosh(i\pi b/2b)}\right]\times\frac{\cos(i\pi y/2a)}{i^3} \qquad (3.5) \\ Q &= \frac{4ba^3}{3\mu}\left(-\frac{dp}{dx}\right)\left[1-\frac{192a}{\pi^5 b}\sum_{i=1,3,5,\ldots}^{\infty}\frac{\tanh(i\pi b/2a)}{i^5}\right] \end{aligned}$$

The validity of the above velocity profile in rectangular microchannels has been confirmed in several studies done by the Micro Particle Image Velocimetry system. A comparison has been done in Fig. 3.2 between the experimental data by Devasenatipathy et al. (see [13]) and the model represented in Eq. 3.5.

3.2 Modeling Friction Factor and Nusselt Number

Muzychka et al. [2] have studied the laminar flow friction and heat transfer characteristics of many duct geometries in the laminar flow regime and the result of their work is simple analytical models for heat transfer coefficient and friction factor, valid for many duct shapes. They have divided their results into the following categories:

- Hydrodynamically fully developed flow

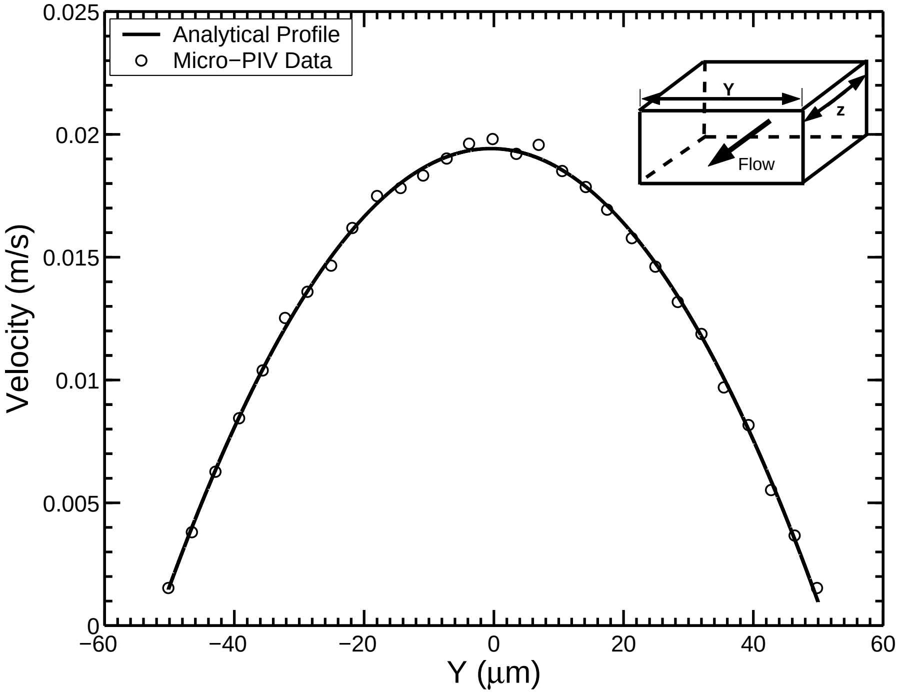

Figure 3.2: Comparison between experimental [13] data and analytical solution [14] for flow in a straight rectangular microchannel, 100μm wide and 107μm deep

- Hydrodynamically developing flow

- Thermally fully developed flow

- Thermally developing flow

- Simultaneously developing flow

3.2.1 Approach to Modeling

By examining the results and the behavior of the existing analytical and numerical solutions in the laminar flow regime, valuable information about the approach to modeling friction and heat transfer is obtained. It is observed that at the beginning of the entrance region of the ducts where the boundary layer thickness is very small, the apparent friction factor does not depend on the cross-sectional geometry and is calculated by the following relationship, regardless of shape:

$$f_{app}Re = \frac{3.44}{\sqrt{z^+}} \tag{3.6}$$

where f_{app} is the apparent friction factor, Re is the Reynolds number, and z^+ is the non-dimensional distance along the duct for the hydrodynamically developing flows, defined as:

$$z^+ = \frac{z}{Re_{\mathcal{L}}\,\mathcal{L}} \tag{3.7}$$

where $\mathcal{L}$ is a characteristic length. As the flow becomes fully developed, the effect of cross-sectional geometry manifests itself. At very large z^+, the fRe group approaches a constant value, strongly dependant on geometry. For most common duct shapes, this constant value is between 12 and 24. A similar behavior is observed for thermally fully developed and thermally developing flows. At the entrance region, Nusselt number is a function of geometry, given by:

$$Nu = C_1 C_2 \left(\frac{fRe_{fd}}{z^*}\right)^{\frac{1}{3}} \tag{3.8}$$

where C_1 determines whether the Nusselt number is averaged or local, C_2 depends on the type of boundary condition, uniform wall temperature or uniform wall heat flux, fRe_{fd} is the friction factor Reynolds number group for fully developed flow, and z^* is the distance along the duct for thermally developing flows defined as:

$$z^* = \frac{z}{Re_{\mathcal{L}}\,\mathcal{L}Pr} \tag{3.9}$$

The dependence of Nu on geometry is because of the dependence of fRe group on cross-sectional geometry. For most common geometries $12 < fRe < 24$, thus $2.29 < (fRe)^{\frac{1}{3}} < 2.88$.

In the fully developed region, Nu number approaches a constant value which is a strong function of cross-sectional shape. For simultaneously developing flows, the Nusselt number is a function of the Prandtl number. This behavior is modeled by the following expression:

$$Nu = \frac{C_4}{\sqrt{z^*}\,\mathrm{Pr}^{\frac{1}{6}}} \tag{3.10}$$

where C_4 depends on the boundary condition. Eventually, the Nusselt number will approach a constant value. The transition of friction factor and Nusselt number from the developing values to the fully developed values is smooth, suggesting that a simple model can combine these asymptotic behaviors. Superposition of the two asymptotic solutions takes the following form:

$$y(z) = \left[y^n_{z\to 0} + y^n_{z\to\infty}\right]^{\frac{1}{n}} \tag{3.11}$$

where $y^n_{z\to 0}$ and $y^n_{z\to\infty}$ are the asymptotic solutions for small and large values of z, respectively. This approach results in a model valid for all values of z along the tube. The fitting parameter, n, is chosen as the value which minimizes the RMS error between the results of the model and the data in the literature.

In order to bring the friction factor and Nusselt number of channels with different cross-sectional geometries together, different characteristic lengths used to non-dimensionalize the Nusselt number and fRe group have been examined by Muzychka and Yovanovich; including the hydraulic diameter, D_h, perimeter of the duct, P, and the square root of the cross-sectional area, $\sqrt{A}$. The most widely used one, the hydraulic diameter, has the advantage of being definable for parallel plate channels, but on the other hand, it has a number of deficiencies. First, the perimeter and area of the hydrodynamically equivalent circular cross-section are not the same as the actual perimeter and area of the non-circular duct, which causes mismatch of dimensionless laminar flow data. Second, using the hydraulic diameter produces results that contradict the correct physical behaviors. For example, in some cases using the hydraulic diameter shows a decrease of friction factor and Nusselt number data with a decrease in aspect ratio[1] which is in contradiction with the observed behavior that the flow friction and heat transfer coefficients generally increase with decreasing aspect ratio. Examining these characteristic lengths revealed that $\sqrt{A}$ and P are successful in bringing the Nu and fRe data close together for different geometries. But, $\sqrt{A}$ is more effective

---

[1] A decrease in aspect ratio means an increase in channel slenderness and vise versa.

in collapsing the data over a wider range of aspect ratios. Furthermore, using $\sqrt{A}$ is more physical, because the cross-sectional area and therefore, the mass flow rate remain conserved.

3.2.2 Fully Developed Flow

Friction Factor

Muzychka analyzed the results of the fRe dimensionless group for many common duct shapes and concluded that using $\sqrt{A}$ is more appropriate than D_h over a wide range of cross-sectional shapes and aspect-ratios. Besides, the friction factor and Nusselt number decrease with increasing aspect ratio for all geometries if the square root of the cross-sectional area is used as the characteristic length. The friction factor Reynolds number group in the fully developed region and for many cross-sectional geometries may be approximated by the solution for the elliptical duct, if the square root of the cross-sectional area is chosen as the dimensionless parameter. The elliptical duct is chosen because it has a closed form solution. In Fig. 3.3, the results for fRe_{D_h} and $fRe_{\sqrt{A}}$ as a function of aspect ratio for the rectangular and elliptical cross sections are plotted, respectively. The results vary substantially when the characteristic length is the hydraulic diameter, but they collapse on each other when the characteristic length is $\sqrt{A}$. The expression for calculating $fRe_{\sqrt{A}}$ in an elliptical duct is:

$$fRe_{\sqrt{A}} = 8\sqrt{\pi}\left(\frac{\pi}{4}\frac{(1+\varepsilon^2)}{\sqrt{\varepsilon}\,\mathbf{E}\left(\sqrt{1-\varepsilon^2}\right)}\right) \tag{3.12}$$

where $\mathbf{E}$ is the elliptical integral of the second kind, and $0.01 < \varepsilon < 1$ is the aspect ratio. The maximum error in predicting the fRe group with Eq. 3.12 for rectangular channels is 7%, and for other duct shapes is 15%. In order to avoid the calculation of the elliptical integral, the following approximate expression was developed in [2] for the term in parentheses:

$$\left(\frac{\pi}{4}\frac{(1+\varepsilon^2)}{\sqrt{\varepsilon}\,\mathbf{E}\left(\sqrt{1-\varepsilon^2}\right)}\right) = \left[\left(\frac{1}{0.92}\right)^{1-\varepsilon}\left(\sqrt{\varepsilon}-\varepsilon^{\frac{3}{2}}\right)+\varepsilon\right]^{-1} \tag{3.13}$$

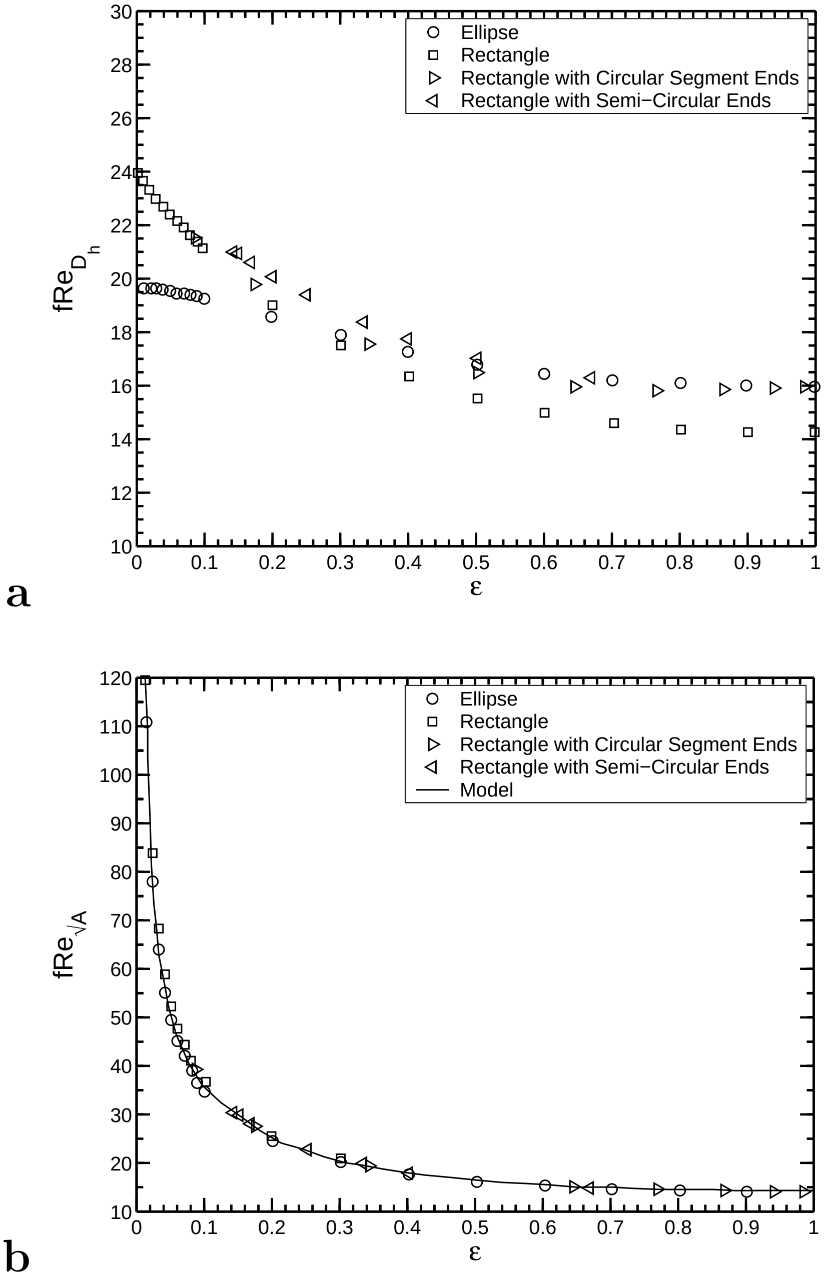

Figure 3.3: Comparison of the experimental data and the model for fRe_{D_h} (a) and $fRe_{\sqrt{A}}$ (b) as a function of aspect ratio. There is a large variation between the results when $\mathcal{L} = D_h$. But, when $\mathcal{L} = \sqrt{A}$ The experimental data and the results of the model are brought together [2]

Table 3.1: Definition of aspect ratio for various geometries.

Geometry	Aspect ratio
Regular polygon	$\varepsilon = 1$
Singly-connected	$\varepsilon = \dfrac{b}{a}$
Trapezoid	$\varepsilon = \dfrac{2b}{a+c}$
Annular sector	$\varepsilon = \dfrac{1-r^*}{(1+r^*)\,\Phi}$
Doubly-connected	$\varepsilon = \sqrt{\dfrac{A_i}{A_o}}$
Circular annulus	$\varepsilon = \dfrac{(1-r^*)}{\pi\,(1+r^*)}$
Eccentric annulus	$\varepsilon = \dfrac{(1+e^*)\,(1-r^*)}{\pi\,(1+r^*)}$

The results of the proposed model for $fRe_{\sqrt{A}}$ given by Eq. 3.12 and fRe_{D_h} for various geometries are compared in Fig. 3.4.

When D_h is used, the results vary significantly and there is no clear trend for the variations of fRe with the aspect ratio. But, when $\sqrt{A}$ is used as the characteristic length, the results are brought together and all geometries have a fRe which increases with decreasing aspect ratio. In Table 3.1, the aspect ratio is defined for the geometries used in the plots.

Comparison with the Microchannel Data Wu and Cheng [1] have conducted careful and extensive experimental investigations on pressure drop of deionized water in smooth trapezoidal microchannels with hydraulic diameters of 25.9 μm- 291.0 μm. They have shown that the friction factor is a strong function of aspect ratio in the microchannels. Their experimental data are found to be in very good agreement with the results of the model used in this study for fully developed laminar flow under the no-slip boundary condition, confirming that macroscopic channel theory is still applicable for microchannels with hydraulic diameters as

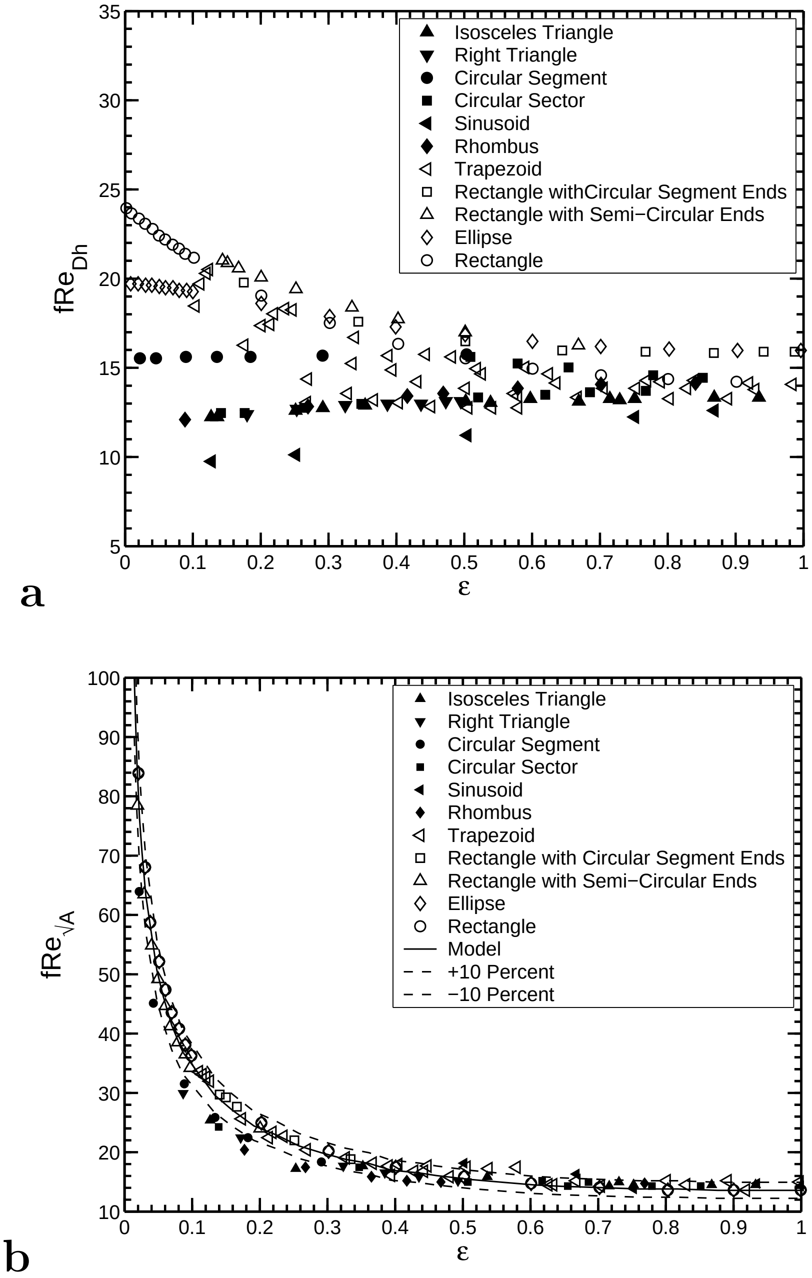

Figure 3.4: fRe_{D_h} (a) and $fRe_{\sqrt{A}}$ (2) as a function of aspect ratio. When $\mathcal{L} = D_h$, the results vary substantially and the trends of the variations in results is not the same for different cross-sectional shapes. But, when $\mathcal{L} = \sqrt{A}$ there is an excellent agreement between the predictions of the model and experimental data [2]

small as $25.9\,\mu m$. Table 3.2 shows the geometric parameters along with the comparison of the friction factor Reynolds number data obtained from the model and the experiments. It is observed that channels with similar values of hydraulic diameter but different aspect ratios have very different values of fRe. Figure 3.5 shows the experimental values of fRe in the laminar Reynolds numbers regime compared to the theoretical value, for two aspect ratios of 0.94 and 0.06.

A number of papers have been published in the past couple of decades, reporting the friction factor data of laminar flow in microchannels. Many of them have reported significant deviation from standard theories for macroscopic channels. Most of their results for friction factor are larger than what is predicted by conventional theory. As a result, an erroneous conclusion has been made that Navier-Stokes equations and no-slip boundary condition are not valid in microchannels. Some researchers have proposed that early transition to turbulent flow occurs in micro-scale. The reason for this discrepancy is that in some of these works, the experiments have been conducted in non-circular channels but the results have been compared to $fRe = 16$ or 64 for circular ducts. Other works have not appropriately accounted for the excess pressure drop caused by area changes at the inlet and exit, and at the entry region of channels.

Nusselt Number

By applying the same approach to Nusselt number data, it can be shown that the Nusselt number as a function of aspect ratio for many different geometries are brought together if $\sqrt{A}$ is used as the characteristic length. In Table 3.3, Nu_{D_h} and $Nu_{\sqrt{A}}$ are compared for both slug and fully developed flows and for uniform heat flux and uniform temperature boundary conditions. The Nusselt number results in each flow and boundary condition reduces to a single value when $\sqrt{A}$ is used as the boundary condition. The difference between the triangular duct and circular duct is 13.9% and 9.1% for the uniform wall temperature and

Table 3.2: Experimental results for the friction factor Reynolds number group compared against the results of the model for a group of microchannels [1]

Channel	Shape	W_b	W_t	H	ε	D_h	$fRe_{\sqrt{A}}$		% Diff.
		μm	μm	μm		μm	Model	Exp.	
N1-100	Trapezoid	100	20.1	56.5	0.94	52.5	14.2	14.5	-1.9
N1-150	Trapezoid	150	70.1	56.4	0.51	69.3	16.2	15.9	1.7
N1-200	Trapezoid	200	120.2	56.4	0.35	78.8	18.7	18.7	0.1
N1-500	Trapezoid	500	420	56.4	0.12	98.1	31.3	31.6	-0.9
N1-1000	Trapezoid	1000	920	56.4	0.06	105.3	46.4	45.8	1.2
N1-4000	Trapezoid	4000	3920	56.4	0.01	110.9	99.9	93.2	7.1
N2-50	Triangle	50	0	35.5	0.71	25.9	14.8	14.0	5.7
N2-100	Trapezoid	100	39.9	42.5	0.61	48.7	15.4	14.9	2.8
N2-150	Trapezoid	150	89.9	42.4	0.35	59.2	18.7	18.2	2.3
N2-200	Trapezoid	200	140	42.2	0.25	65.0	21.9	22.3	-2.1
N2-500	Trapezoid	500	440	42.5	0.09	76.4	36.8	38.1	-3.2
N2-1000	Trapezoid	1000	940	42.4	0.04	80.6	54.4	54.6	-0.3
N2-4000	Trapezoid	4000	3940	42.4	0.01	83.8	116.4	110.6	5.3
N3-50	Triangle	50	0	35.5	0.71	25.9	14.8	13.6	8.8
N3-100	Triangle	100	0	70.5	0.71	51.7	14.8	14.2	4.2
N3-150	Triangle	150	0	106.0	0.71	77.6	14.8	14.4	2.8
N3-200	Triangle	200	0	141.1	0.71	103.4	14.8	14.85	-0.3
N3-500	Trapezoid	500	284	152.6	0.39	206.6	17.9	17.18	4.2
N3-1000	Trapezoid	1000	784	152.5	0.17	252.2	26.3	26.0	1.1
N3-2000	Trapezoid	2000	1784	152.5	0.08	277.6	39.1	38.8	0.8
N3-4000	Trapezoid	4000	3784	152.5	0.04	291.0	57.8	56.0	3.2
N4-100	Triangle	100	0	70.5	0.71	51.7	14.8	14.0	5.5
N4-200	Trapezoid	200	27.2	122.1	0.93	105.4	14.2	15.3	-7.2
N4-500	Trapezoid	500	327	122.1	0.30	179.3	20.2	20.55	-1.7
N4-1000	Trapezoid	1000	827	122.1	0.13	209.8	29.9	31.0	-3.5
N4-4000	Trapezoid	4000	3828	122.1	0.03	235.2	65.4	64.1	2.0
N5-150	Trapezoid	150	47.4	72.5	0.73	76.3	14.7	14.9	-1.3
N5-500	Trapezoid	500	279	156.2	0.40	209.5	17.7	17.1	3.9

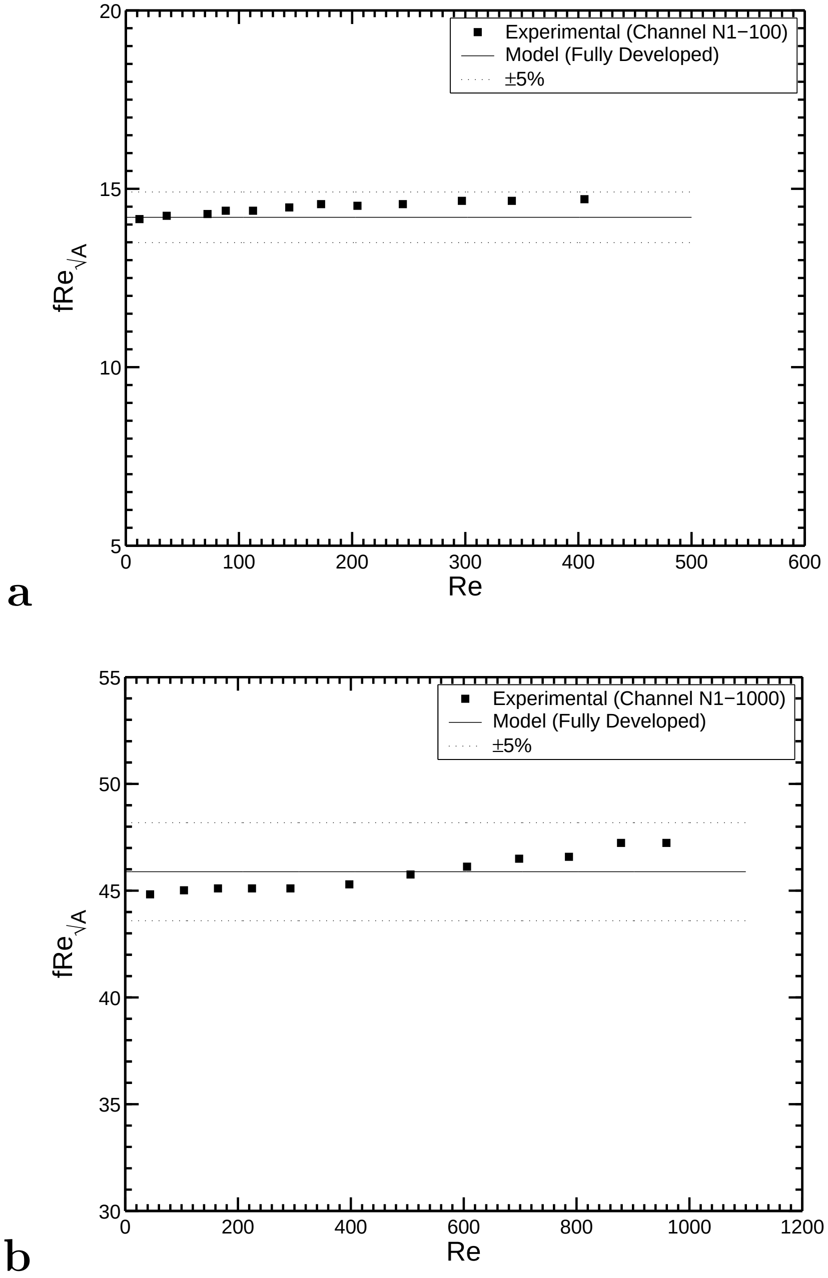

Figure 3.5: Comparison of the experimental data for fully developed fRe group [1] with the result of the model, for the N1-100 (a) and N1-1000 (b) channels with aspect ratios of 0.94 and 0.06, respectively

uniform wall heat flux, respectively, when the characteristic length is $\sqrt{A}$. While, these differences are 32.5% and 28.7% when the characteristic length is the hydraulic diameter. The Nusselt numbers, based on the square root of the cross-sectional area, for different duct shapes with the constant temperature and constant heat flux boundary conditions are compared in Figs. 3.6 a and b, respectively.

Table 3.3: Nusselt numbers for slug and fully developed flows [2]

		Isoflux		Isothermal	
	Geometry	FDF	Slug	FDF	Slug
Nu_{D_h}	Triangle	3.11	-	2.47	-
	Square	3.61	7.08	2.98	4.93
	Hexagon	4.00	7.53	3.35	5.38
	Octagon	4.21	7.69	3.47	5.53
	Circular	4.36	7.96	3.66	5.77
Nu_{D_h}	Triangle	3.51	-	2.79	-
	Square	3.61	7.08	2.98	4.93
	Hexagon	3.74	7.01	3.12	5.01
	Octagon	3.83	7.00	3.16	5.03
	Circular	3.86	7.06	3.24	5.11

The plots show two distinct bounds for $Nu_{\sqrt{A}}$; a lower bound for duct shapes that have corner angles less than 90° and an upper bound for shapes with rounded or right angled corners. The following model has been developed to calculate the Nusselt number in the thermally fully developed region for a wide range of cross-sectional areas:

$$Nu_{\sqrt{A}} = Nu^0_{\sqrt{A}} \left(\frac{f\, Re_{\sqrt{A}}}{8\sqrt{\pi}\, \varepsilon^{\gamma}} \right) \tag{3.14}$$

where $Nu^0_{\sqrt{A}}$ is 3.24 for uniform wall temperature boundary condition and 3.86 for uniform wall heat flux boundary condition, and γ is $1/10$ for upper bound duct shapes or $-3/10$ for lower bound shapes. It is clear that using the square root of the cross-sectional area has significantly reduced the variation in results. Almost all of the available experimental data are predicted by Eq. 3.14 within ±10%.

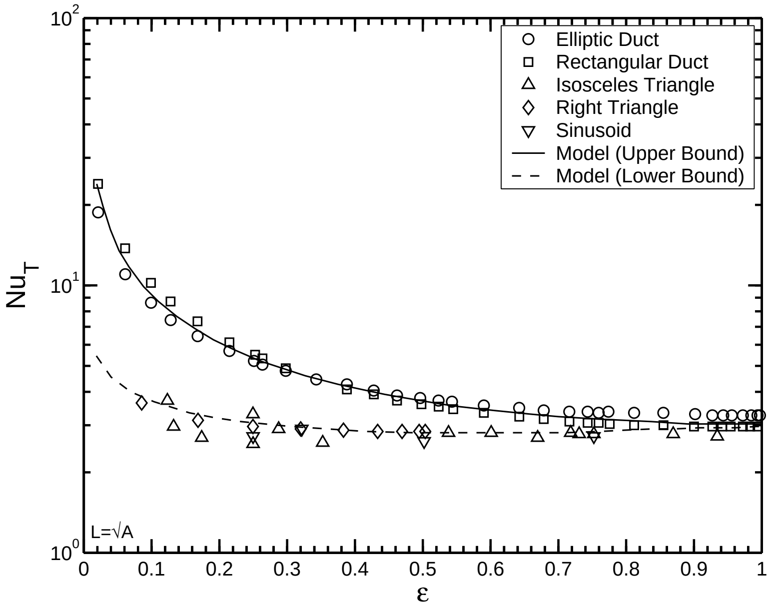

a

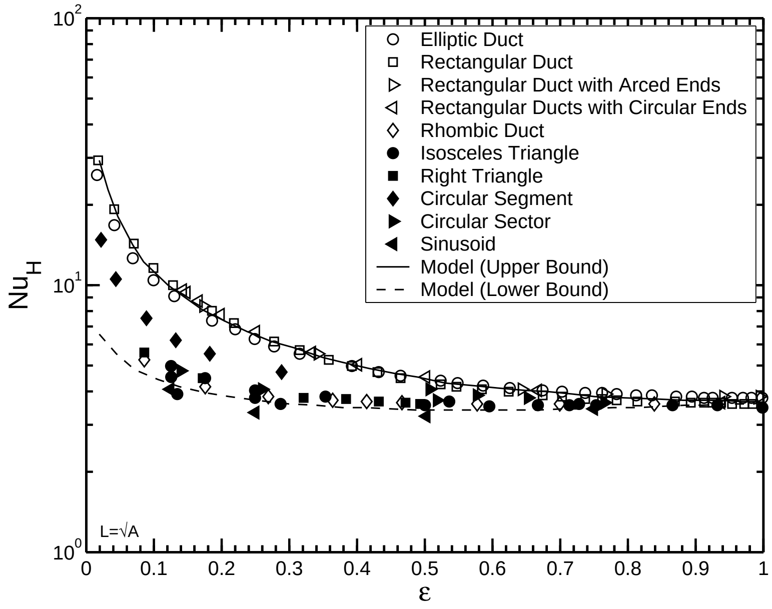

b

Figure 3.6: Comparison of the experimental results for fully developed Nusselt number, under the constant wall temperature (a) and constant wall heat flux (b) boundary conditions, with the results of the model. The characteristic length is $\sqrt{A}$ and there is complete agreement between the results [2]

3.2.3 Developing Flow

Friction Factor

Models for hydrodynamically and thermally developing flows are developed by matching the asymptotic solutions for the entrance region and fully developed region. As stated earlier, there exist analytical solutions for friction factor and Nusselt number at the beginning of the entrance region which are independent of duct geometry. For hydrodynamically developing flow:

$$f_{app}Re_{\mathcal{L}} = \frac{3.44}{\sqrt{z^+_{\mathcal{L}}}} \tag{3.15}$$

valid for $z^+_{\mathcal{L}} < 0.001$. Combining this solution with the solution for fully developed flow, Eq. 3.12), using Eq. 3.11, and substituting for $\mathcal{L}$ with $\sqrt{A}$ results in:

$$\begin{aligned} f_{app}Re_{\sqrt{A}} &= \left[\left\{\frac{3.44}{\sqrt{z^+_{\sqrt{A}}}}\right\}^2 + \{fRe\}^2\right]^{\frac{1}{2}} \\ &= \left[\left\{\frac{3.44}{\sqrt{z^+_{\sqrt{A}}}}\right\}^2 + \left\{8\sqrt{\pi}\left(\frac{\pi}{4}\frac{(1+\varepsilon^2)}{\sqrt{\varepsilon}\,\mathbf{E}\left(\sqrt{1-\varepsilon^2}\right)}\right)\right\}^2\right]^{\frac{1}{2}} \end{aligned} \tag{3.16}$$

The fitting parameter, n, was chosen such that the RMS difference between the model results and the numerical and analytical results in the literature is minimized. A comparison has been made between the experimental data and the present model in Figs. 3.7 a and b, over a wide range of z^+ and for various geometries. The proposed model can predict the data available in the literature within ±12%.

Kohl et al. [15] constructed straight microchannels with integrated pressure sensors with hydraulic diameters of 25 to 100 μm to investigate the discrepancies in previously published data for pressure drop in microchannels. The integrated sensors allow for static pressure measurements inside the microchannel at multiple locations. They used deionized water in a Reynolds number range of 4.9 to 2068. The results of their work suggest that

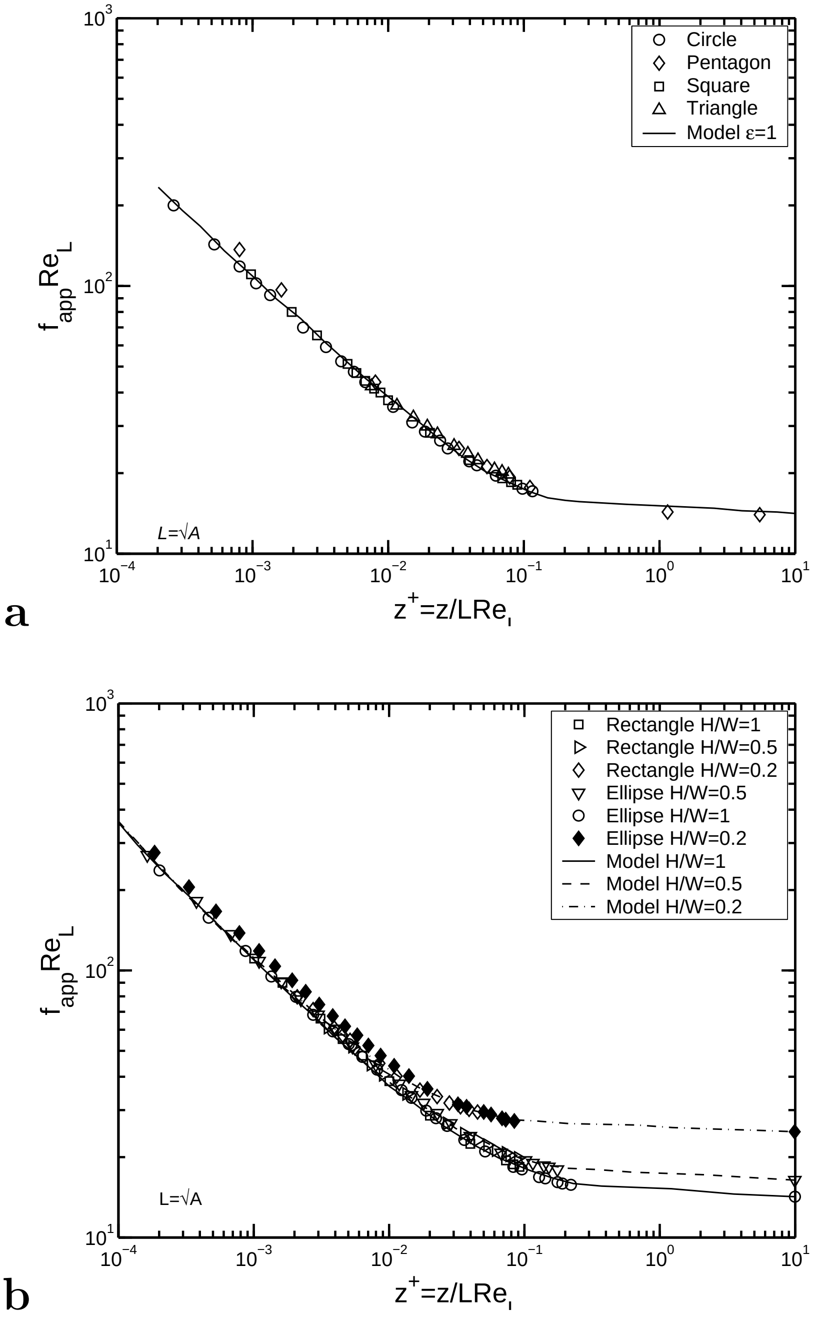

Figure 3.7: Apparent friction factor Reynolds number group as a function of position along the channel. With $\sqrt{A}$ as the characteristic length, the results of the model are in complete agreement with the results of the experiments [2]

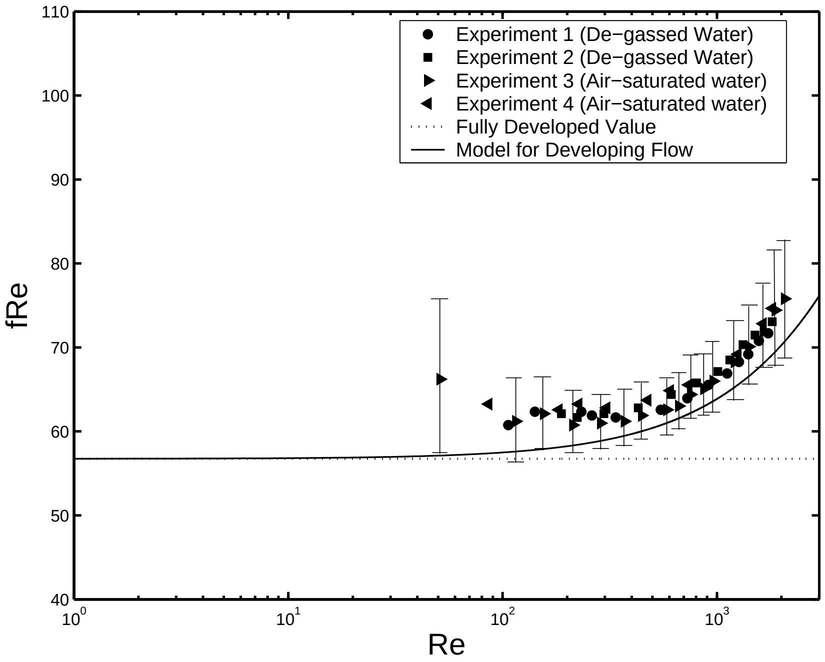

Figure 3.8: Friction factor Reynolds number group as a function of Reynolds number. When the Reynolds number rises, the length of the hydrodynamically developing region increases, thus the friction factor goes up as a result of a larger part of the channel having a steep velocity gradient at the wall [15]

the conventional theories for macroscopic channels can be accurately used to predict the pressure drop in microchannels. In Fig. 3.8 the experimental data of Kohl et al. have been compared to the results of the model for developing flow in the laminar Reynolds number regime. There is excellent agreement between the prediction of the model and the available data. It is observed that the deviation from the fully developed value of fRe, caused by not accounting for the excess pressure drop in the developing region, may be misinterpreted as the early transition to turbulent flow, reported in some of the previously published works(see [30], [31], [32], [33], [34]).

Table 3.4: Constants for the thermally fully developed flow Nusselt number

	Local	**Averaged**
C_1	1	1.5

	Isothermal	**Isoflux**
C_2	0.409	0.501
C_3	3.01	3.66

	Upper Bound	**Lower Bound**
γ	0.1	-0.3

Nusselt Number

A general model for predicting the Nusselt number in the thermal entrance region can be developed by combining the analytical solution for Nu at the beginning of the entrance region, Eq. 3.8, and the solution for the fully developed region, Eq. 3.14. The resulting expression is:

$$Nu_{z^*} = \left[\left\{ C_1 C_2 \left(\frac{fRe_{\sqrt{A}}}{z^*_{\sqrt{A}}} \right)^{\frac{1}{3}} \right\}^5 + \left\{ C_3 \left(\frac{fRe_{\sqrt{A}}}{8\sqrt{\pi}\varepsilon^{\gamma}} \right) \right\}^5 \right]^{\frac{1}{5}} \tag{3.17}$$

where the constants C_1, C_2, C_3,and γ are given in Table 3.4, and $fRe_{\sqrt{A}}$ is obtained from Eq. 3.12. Equation 3.17 can predict the Nusselt number for various duct shapes within ±12%. A comparison of this model's results with the available data is presented in Fig. 3.9. Heat transfer in microchannels has been studied and compared to large-scale channels in a number of previously published works. Similar to friction factor, there is a wide discrepancy in heat transfer data between different published works. The transitional Reynolds number also varies widely in these studies. The validity of the Navier-Stokes equations in representing the heat transfer characteristics of micro-flows has been called into question in some of these works.

Most recent studies have confirmed that flow and heat transfer behavior of micro-flows

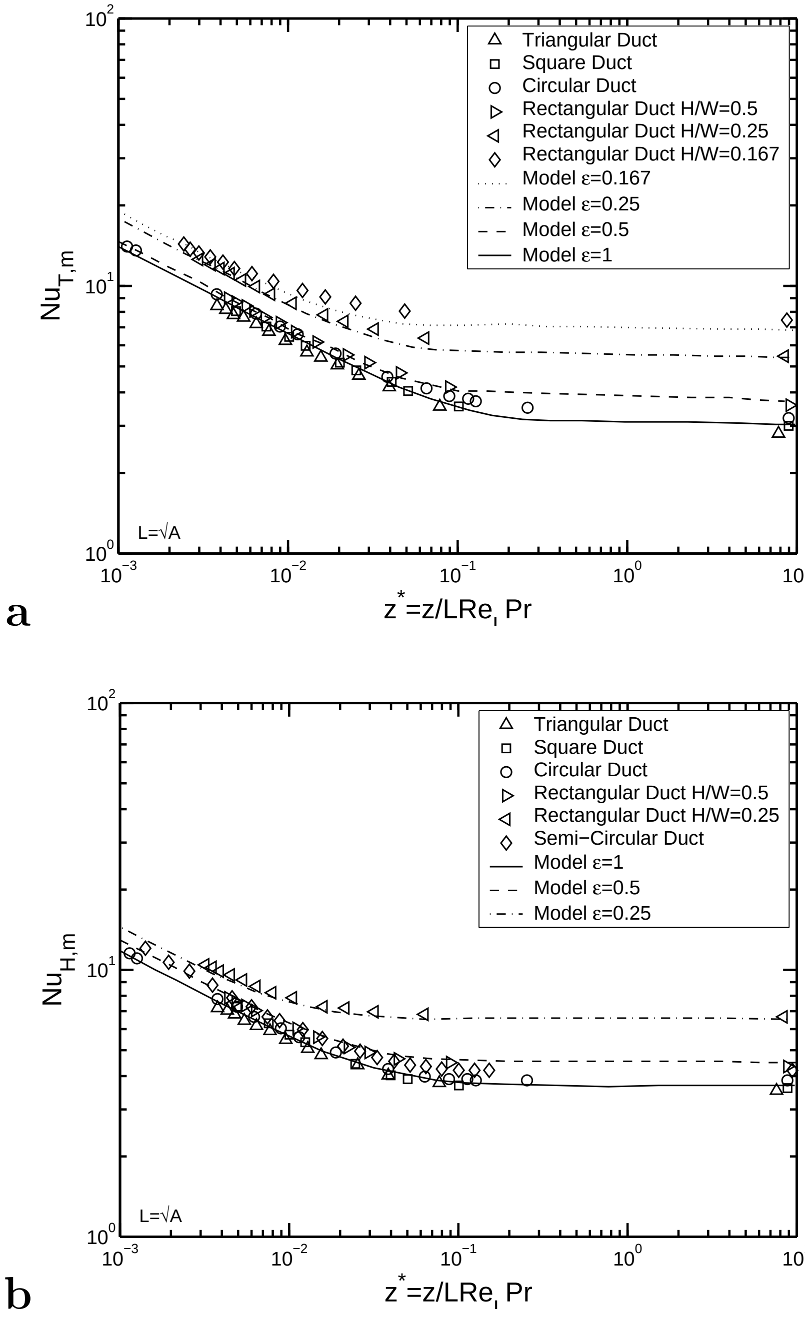

Figure 3.9: Nusselt number in the thermally developing region, with the constant temperature wall (a) and constant heat flux (b) boundary condition. The model results agree well with the experimental data when $\mathcal{L}=\sqrt{A}$ [2]

is similar to that of large-scale flows, and if any non-Navier-Stokes phenomenon exists, its effect is so small that it is masked by experimental uncertainties. Lee et al.[16] conducted experiments to explore the validity of conventional theories in predicting the heat transfer behavior of liquid flows in microchannels. They considered channels with a width of 194 μm to 534 μm and a height of roughly five times the width. They used deionized water as the working fluid with the Reynolds number ranging from 300 to 3500. Their results for Nusselt number are in close agreement with numerical results based on the classical, Navier-Stokes approach.

In Fig. 3.10, the experimental results of Lee et al. [16] for the average Nusselt number have been compared to the results of the model used in this work for a microchannel of 194 μm wide and 884 μm high. Up to a Reynolds number of approximately 2000, the experimental data agrees very well with the model. The data also suggest a transition to turbulent flow at a Reynolds number of 2000. The experimental results are compared against the model results for three more microchannels in the laminar Reynolds number regime in Fig. 3.11 . There is complete agreement between the model and experimental results, suggesting that the proposed model, based on conventional channel theory, can be employed to predict Nusselt number in microchannels.

The test pieces are made of copper with the top wall made of an insulating material, i.e. only three walls are being heated; but, the model is based on the assumption that heat transfer occurs on all the four walls of the channel. Therefore, the results of the model should be corrected before being compared to the experimental data. The following correction factor, proposed by Phillips [35] is used in this work to correct the effect of 3 heated side walls:

$$Nu_{z,3} = Nu_{z,4} \times \frac{Nu_{\infty,4}}{Nu_{\infty,3}} \tag{3.18}$$

where $Nu_{z,3}$ and $Nu_{z,4}$ are the three and four heated side wall Nusselt numbers for developing

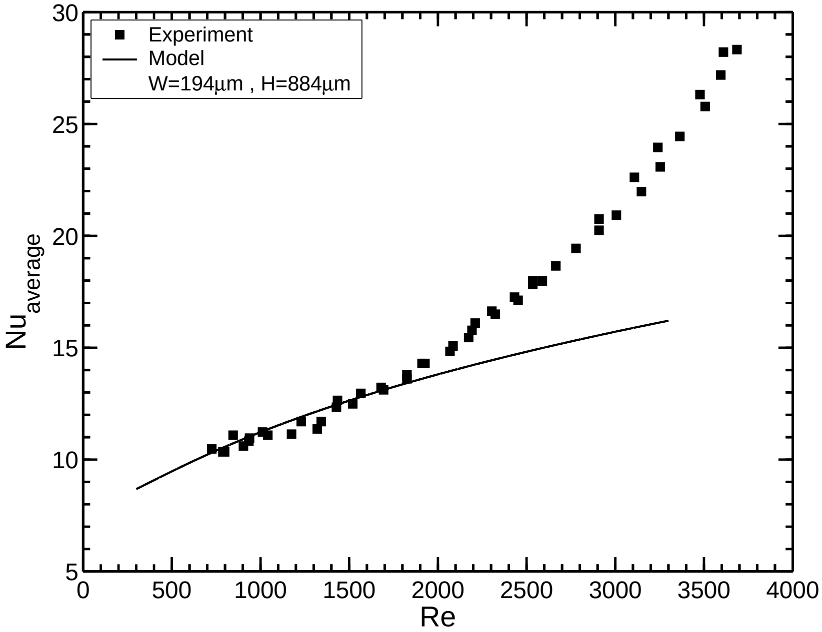

Figure 3.10: Average Nusselt number as a function of Reynolds number with $\sqrt{A}$ as the characteristic length. The results of the model and experimental data agree well up to a Reynolds number of roughly 2000 [16]

flow, and $Nu_{\infty,3}$ and $Nu_{\infty,4}$ are the three and four heated side wall Nusselt numbers for fully developed flow. It is assumed that the ratio of the three and four heated wall cases for fully developed flow are equal to that for developing flow. $Nu_{\infty,4}$ is obtained from Eq. 3.14 and $Nu_{\infty,3}$ is given by the following expression [36]:

$$Nu_{\infty,3} = 8.235\left(1 - \frac{1.883}{\varepsilon} + \frac{3.767}{\varepsilon^2} - \frac{5.814}{\varepsilon^3} + \frac{5.361}{\varepsilon^4} - \frac{2.0}{\varepsilon^5}\right) \tag{3.19}$$

The numerical results of Lee et al. [17] for average Nusselt number as a function of position along the channel, which is based on Navier-Stokes equations, is compared against the results of the model in Figs. 3.12 a and b, for channel aspect ratios of 1 and 1/10, respectively. The agreement between the results is satisfactory. Finally, for the combined entrance region or simultaneously developing flow, a model has been developed by combining the solutions of the thermally developing flow with the solution for the flat plate; because, in the combined

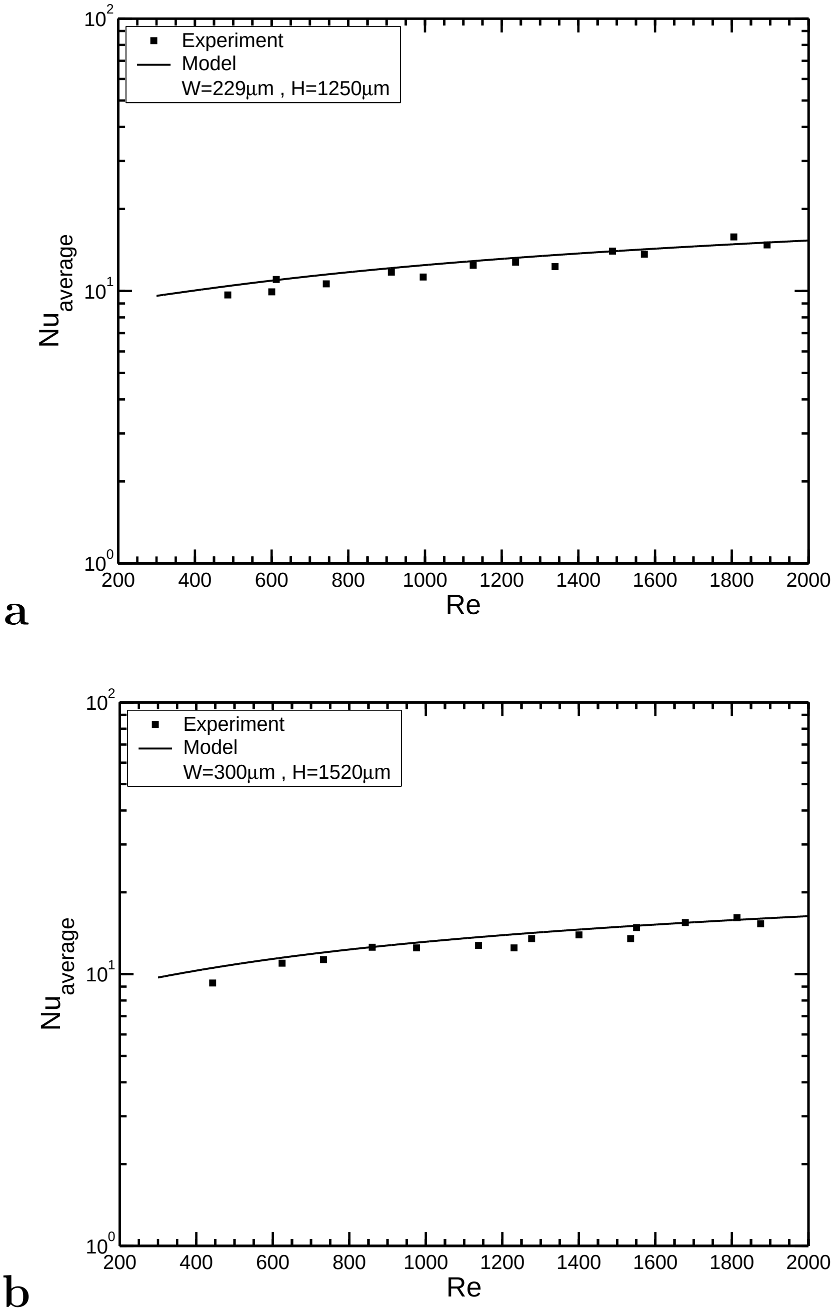

Figure 3.11: Experimental and model results for average Nusselt number as a function of Reynolds number with $\mathcal{L} = \sqrt{A}$ at two aspect ratios [17]

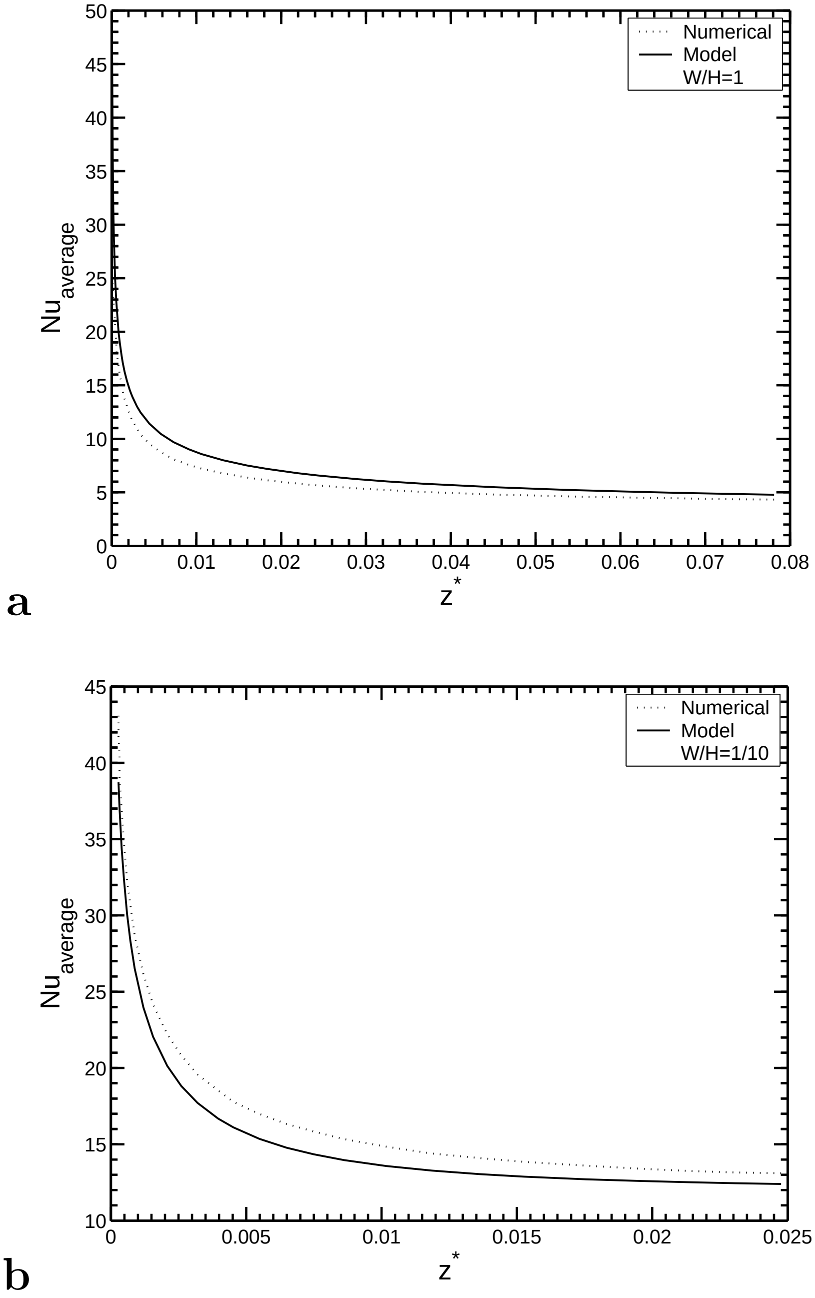

Figure 3.12: Comparison of the Numerical results for average Nusselt number as a function of location along the tube with the results of the model, at a channel aspect ratio of 1 (a) and 1/10 (b) [17]

entrance region the boundary layer behavior is similar to that over a flat plate. The proposed model has the following form:

$$y(z) = \left(\{ y_{z\to 0}(Pr)^m \} + \{ y^n_{z\to 0} + y^n_{z\to\infty} \}^{\frac{m}{n}} \right)^{\frac{1}{m}} \tag{3.20}$$

The model is a combination of three asymptotic solutions. The first term in braces is the solution for a flat plate and may be written as:

$$Nu_{\mathcal{L}} = \frac{C_4 C_5}{\sqrt{z^*}\,\mathrm{Pr}^{\frac{1}{6}}} \tag{3.21}$$

where C_4 takes a value of 1 or 2 for local or average solutions, respectively, and C_5 takes a value of 0.332 or 0.453 for uniform wall temperature or uniform wall heat flux boundary condition, respectively. The second term in braces in Eq. 3.20 is the solution for thermally developing flow in ducts given by Eq. 3.17. The result is:

$$Nu_{z^*} = \left[\left(\left\{ C_1 C_2 \left(\frac{fRe_{\sqrt{A}}}{z^*_{\sqrt{A}}} \right)^{\frac{1}{3}} \right\}^5 + \left\{ C_3 \left(\frac{fRe_{\sqrt{A}}}{8\sqrt{\pi}\varepsilon^{\gamma}} \right) \right\}^5 \right)^{\frac{m}{5}} + \left\{ \frac{C_4 C_5}{\sqrt{z^*_{\sqrt{A}}}\,\mathrm{Pr}^{\frac{1}{6}}} \right\}^m \right]^{\frac{1}{m}} \tag{3.22}$$

This model is valid for $0.1 < Pr < \infty$ and the optimal value of m is 5. The proposed model predicts most of the available data within ±15%.

3.2.4 Pressure Variations Caused by Area Changes

Abdellal et al. [37] experimentally investigated the pressure drop caused by an abrupt area expansion and contraction in micro-tubes, using water as the working fluid with the larger and smaller tube diameters of 1.6 *mm* and 0.84 *mm*, respectively. They concluded that the expansion and contraction loss coefficients agree reasonably well with the commonly used prediction methods for large tubes. Therefore, analytical expressions for pressure drop in sudden area changes have been developed here based on the conventional channel theories.

The pressure variation caused by an abrupt area change, is composed of a reversible and an irreversible part. The reversible alterations in pressure is due basically to the area changes and the resulting velocity variations to satisfy the momentum conservation principle. The reversible pressure changes may be positive or negative. The irreversible pressure drop, which is always positive, is caused primarily by viscous dissipation in the decelerating flow regions due to the loss of kinetic energy. The majority of this loss is due to the inertial effects which are eventually dissipated by the shear stresses within the fluid and only a small portion of it is due to the wall shear stress.

By applying the one-dimensional mass, momentum, and energy conservation equations to the control volume shown in Fig. 3.13 in an abrupt expansion, we can determine the two pressure drop components:

$$\begin{aligned} A_1 V_1 &= A_2 V_2 \Rightarrow \frac{V_2}{V_1} = \frac{A_1}{A_2} && (3.23) \\ p_1\, A_2 - p_2\, A_2 &= \rho\beta_{1,2} A_2 V_2^2 - \rho\beta_{1,1} A_1 V_1^2 \Rightarrow p_1 - p_2 = \rho V_1^2 \left(\beta_{1,2}\frac{V_2^2}{V_1^2} - \beta_{1,1}\frac{A_1}{A_2}\right) && (3.24) \\ p_1 + \frac{1}{2}\beta_{2,1}\rho V_1^2 &= p_2 + \frac{1}{2}\beta_{2,2}\rho V_2^2 + \Delta p_{L,e} \ \Rightarrow \\ \Delta p_{L,E} &= (p_1 - p_2) + \frac{1}{2}\rho V_1^2 \left(\beta_{2,1} - \beta_{2,2}\frac{V_2^2}{V_1^2}\right) && (3.25) \end{aligned}$$

where $\Delta p_{L,E}$ is the irreversible pressure loss in an expansion, $p_1 - p_2$ is the total pressure loss, V is the average velocity, A is the cross-sectional area, ρ is the fluid density, β_1 is the momentum correction factor, and β_2 is the kinetic energy correction factor.

These factors show the deviation of the momentum and kinetic energy in the actual velocity profiles from that in a uniform velocity profile and are defined as:

$$\beta_1 = \frac{1}{A}\int \left(\frac{v}{V_{ave}}\right)^2 dA \qquad (3.26)$$

$$\beta_2 = \frac{1}{A}\int \left(\frac{v}{V_{ave}}\right)^3 dA \qquad (3.27)$$

where the average velocity is:

$$V_{ave} = \frac{1}{A}\int v dA \qquad (3.28)$$

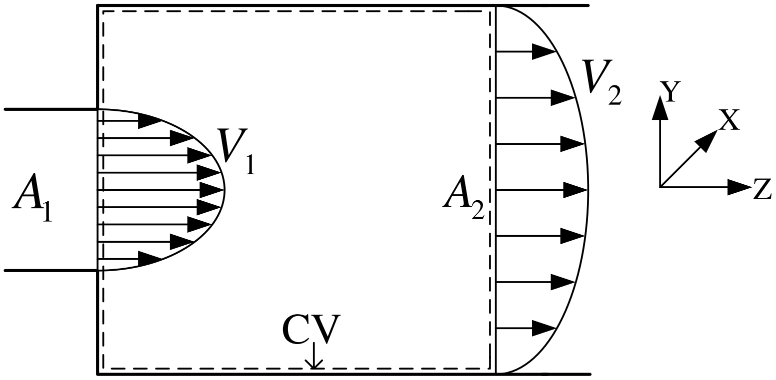

Figure 3.13: The control volume used in deriving the pressure loss coefficient for an abrupt expansion

These factors depend on the cross-sectional geometry and the flow regime. For the rectangular channel, the analytical velocity distribution in the fully developed laminar regime, dominant in this work, is known (see Sec. 3.1); therefore, we can calculate the correction factors by doing the integrations numerically. For an aspect ratio of one:

$$\beta_1 = 1.3784$$

$$\beta_2 = 2.1546$$

By substituting for $p_1 - p_2$ in Eq. 3.25 from Eq. 3.24, and for V_2/V_1 from Eq. 3.23 in Eqs. 3.24 and 3.25, we obtain the following relation for irreversible pressure drop:

$$\Delta p_{I,E} = \frac{1}{2}\rho V_1^2 \left(2\beta_{1,2}\sigma^2 - 2\beta_{1,1}\sigma + \beta_{2,1} - \beta_{2,2}\sigma^2\right) \tag{3.29}$$

where σ is the area ratio, A_1/A_2. The most common method used to show these pressure losses is to specify a loss coefficient, defined as:

$$K_{L,E} = \frac{\Delta p_{L,E}}{\frac{1}{2}\rho V^2} \tag{3.30}$$

by analogy with Eq. 3.29, the loss coefficient for an abrupt expansion is:

$$K_{L,E} = 2\beta_{1,2}\sigma^2 - 2\beta_{1,1}\sigma + \beta_{2,1} - \beta_{2,2}\sigma^2 \tag{3.31}$$

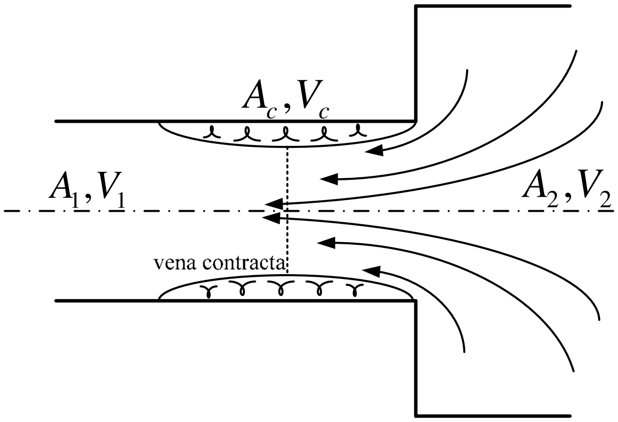

Figure 3.14: Flow pattern in a sharp entrance

and the total pressure change is:

$$\Delta p_{tot,E} = p_1 - p_2 = \frac{1}{2}\rho V_1^2 \left(\beta_{1,2}\sigma^2 - \beta_{1,1}\sigma\right) \tag{3.32}$$

In an abrupt contraction (see Fig. 3.14), a vena contracta region is formed because the fluid can not turn a sharp corner. The maximum velocity occurs at section c where the flow area is minimum. The fluid can be accelerated very efficiently from section 2 to section c without producing any irreversible pressure loss. But, it is almost impossible to decelerate the fluid efficiently; therefore, the pressure can not be recovered completely after the vena contracta. To develop a model for the pressure variations in a sudden contraction, we apply the same analysis as a sudden expansion to the region after section c, and further assume that there is no irreversible losses before section c. The following expression for the irreversible pressure loss can be easily developed:

$$\Delta p_{I,C} = \frac{1}{2}\rho V_1^2 \left(\frac{2\beta_{1,1}C_c^2 - 2C_c + 1 - \beta_{2,1}C_c^2}{C_c^2}\right) \tag{3.33}$$

where C_c is the contraction coefficient A_c/A_1. We have assumed that the velocity profile at the vena contracta cross section is flat, since it is not in contact with the walls; therefore,

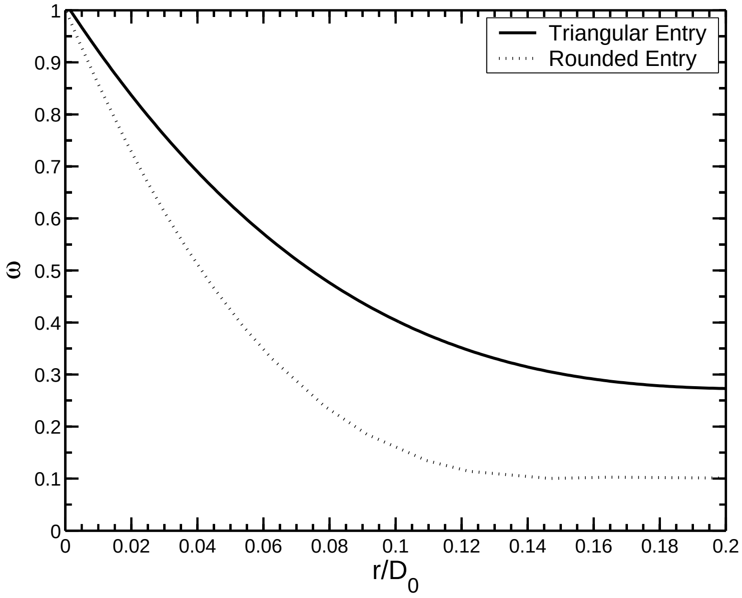

Figure 3.15: Pressure loss coefficient correction factor for rounded entrances [18]

$\beta_{1,c} = \beta_{2,c} = 1$. Using the same approach as the sudden expansion, the total pressure drop is found:

$$\Delta p_{tot,C} = \frac{1}{2}\rho V_1^2 \left(\frac{2\beta_{1,1}C_c^2 - 2C_c + 1 - \beta_{2,3}C_c^2\sigma^2}{C_c^2} \right) \tag{3.34}$$

where σ is the area ratio, A_1/A_2. The contraction coefficient, C_c, is actually a function of Reynolds number and the area ratio, but may be roughly estimated by the following expression [37]:

$$C_c = 1 - \frac{1-\sigma}{2.08(1-\sigma)+0.5371} \tag{3.35}$$

The loss coefficient of a sudden contraction is strongly dependant on the entrance shape. If the area change occurs smoothly, the pressure losses reduce significantly. This is taken into account in this work by introducing a correction factor, ω, which is presented in Fig. 3.15 [18], with r/D_{h0} defined in Fig. 3.16. The following polynomial curves can accurately

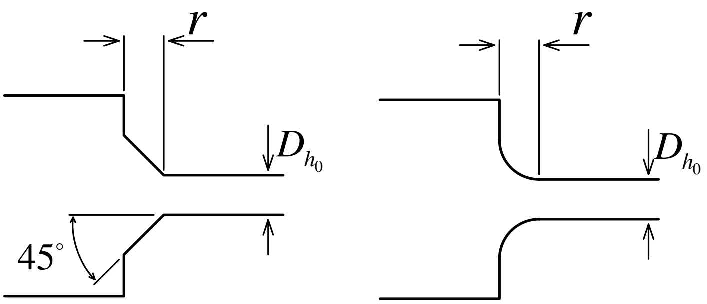

Figure 3.16: r and D_{h_0} for rounded entrance shapes

predict ω:

$$\begin{aligned}\omega_{triangular} = & - 366.6\left(\frac{r}{D_{h0}}\right)^4 + 84.289\left(\frac{r}{D_{h0}}\right)^3 + 24.291\left(\frac{r}{D_{h0}}\right)^2 - 8.9958\left(\frac{r}{D_{h0}}\right) \\ & + 1.0094 \qquad (3.36)\end{aligned}$$

$$\begin{aligned}\omega_{rounded} = & - 381.44\left(\frac{r}{D_{h0}}\right)^5 - 113.06\left(\frac{r}{D_{h0}}\right)^4 - 82.164\left(\frac{r}{D_{h0}}\right)^3 + 77.707\left(\frac{r}{D_{h0}}\right)^2 \\ & - 15.247\left(\frac{r}{D_{h0}}\right) + 1.0023 \qquad (3.37)\end{aligned}$$

The pressure loss coefficient for the smooth area changes will then be:

$$K_{smooth} = \omega\, K_{abrupt} \tag{3.38}$$

To predict the pressure changes in the triangular exit, the data for the loss coefficient in a conical diffuser are used [19]. This approach was successfully used to model pressure drop in micro flat walled diffusers by Olsson et al.[38]. The results for a conical diffuser, for a fixed area ratio, are shown in Fig. 3.17. The angle of the diffuser is the controlling parameter of the loss coefficient. For moderate and large diffuser angles, the flow separates from the walls and the losses are due mainly to the viscous dissipation. For small angles, the diffuser is long and the losses are mostly due to the wall shear stresses. In fact, the conical diffuser is less

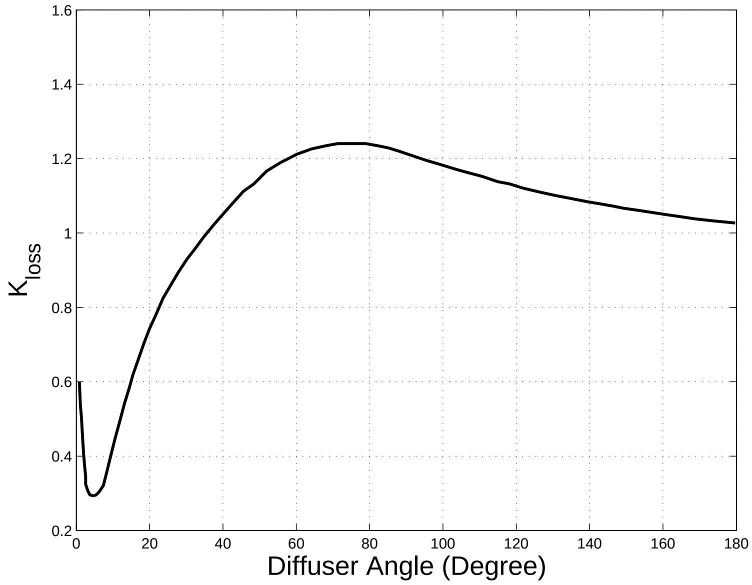

Figure 3.17: Pressure loss coefficient of a conical diffuser as a function of diffuser angle [19]

efficient than an abrupt area change for moderate and large angles because of the combined effect of separation and wall friction effects. The following two polynomial have been used to estimate the values of K_{loss} in the above diagram:

$$\begin{aligned} \text{From } 8^\circ \text{ to } 180^\circ\text{: } K_{loss} &= -5.0828e-9\,\theta^4 + 2.762e-6\,\theta^3 - 0.00054002\,\theta^2 + 0.042701\,\theta^1 \\ &+ 0.061772 \qquad (3.39) \end{aligned}$$

$$\begin{aligned} \text{From } 0^\circ \text{ to } 8^\circ\text{: } K_{loss} &= -0.0045919\,\theta^4 + 0.049071\,\theta^3 - 0.14557\,\theta^2 - 0.003565\,\theta^1 \\ &+ 0.67709 \qquad (3.40) \end{aligned}$$

No models or correlations exist for the rounded expansion (to the knowledge of the author); therefore, the loss coefficient has been estimated by assuming the rounded expansion to be composed of a straight, a triangular, and an abrupt expansion whose loss coefficients are known (see Fig. 3.18)

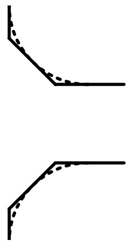

Figure 3.18: Approximating a rounded entrance with a straight, a triangular, and a sudden area change

3.3 Entropy Generation Model

The goal of this section is to develop a model for predicting the total rate of entropy generation in a microchannel, including the entrance and exit. The following equation (Eq. 1.21) was developed in chapter one, for the entropy generation in a duct[2]:

$$\dot{S}_{gen} = \dot{m}\frac{\Delta p}{\rho T} + \frac{\dot{Q}^2 R_{th}}{T_H^2}$$

The first step in developing the model from Eq. 1.21 is to relate Δp and R_{th} to $f_{app}Re$ and Nu, respectively.

From the definition of friction factor, for the developing flow, we have:

$$f_{app} = \frac{2\,\tau_w}{\rho V^2} \tag{3.41}$$

where τ_w is the wall shear stress and V is the average velocity in the channel. By writing a force balance in the x direction (see Fig. 3.19), an expression for τ_w as a function of the pressure drop will be obtained:

$$P\,L\,\tau_w = A_{cs}\,\Delta p \Rightarrow \tau_w = \frac{A_{cs}\,\Delta p}{PL} \tag{3.42}$$

where P is the perimeter, L is the length, and A_{cs} is the cross-sectional area of the channel. By substituting for τ_w in Eq. 3.41 from Eq. 3.42 and rearranging, an expression for pressure

---

[2] For more details, see [24].

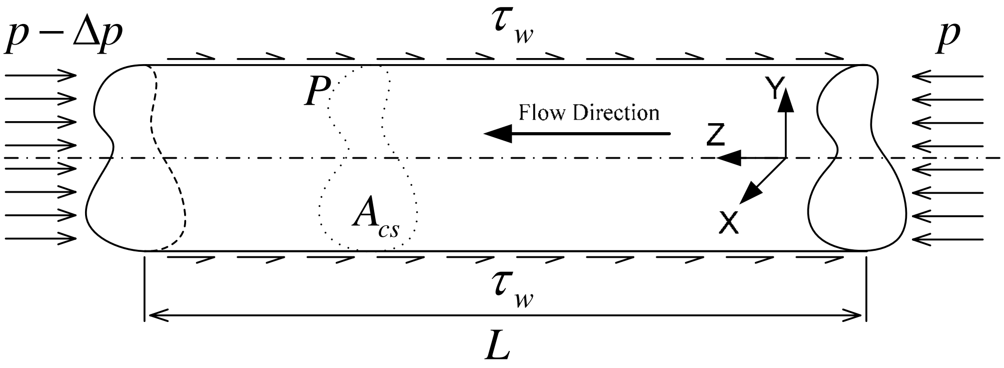

Figure 3.19: Forces applied to an element of fluid in a duct of arbitrary cross-section

drop as a function of friction factor will be obtained:

$$\Delta p_{ch} = f_{app}\frac{1}{2}\rho V^2\frac{LP}{A_{cs}} = f_{app}\,\frac{\dot{m}^2 LP}{\rho A_{cs}^3} \tag{3.43}$$

From the definition of loss coefficient, K_L, we have:

$$\Delta p_L = K_L\frac{1}{2}\rho V^2 = K_L\frac{\dot{m}^2}{2\rho A_{cs}^2} \tag{3.44}$$

The frictional term of the entropy generation in the duct is:

$$\dot{S}_{gen,\,\Delta p} = \dot{m}\frac{\Delta p_{tot}}{\rho T} \tag{3.45}$$

replacing Δp in Eq. 3.45 from Eqs. 3.43 and 3.44 yields the following relationship for $\dot{S}_{gen,\,\Delta p}$ as a function of f:

$$\dot{S}_{gen,\,\Delta p} = f_{app}\,\frac{\dot{m}^3 LP}{T\rho^2 A_{cs}^3} + K_L\frac{\dot{m}^3}{2T\rho^2 A_{cs}^2} \tag{3.46}$$

Models were developed earlier in this chapter for $fRe_{\sqrt{A}}$. Therefore we substitute f with $fRe_{\sqrt{A}}$ and multiply the denominator by $Re_{\sqrt{A}}$. The following expression is obtained:

$$\dot{S}_{gen,\,\Delta p} = f_{app}Re_{\sqrt{A}}\frac{L}{\sqrt{A_{cs}}}\frac{\dot{m}^2 P\mu}{2T\rho^2 A_{cs}^2} + K_L\frac{\dot{m}^2\mu\sqrt{A_{cs}}}{2T\rho^2 A_{cs}^2} \tag{3.47}$$

where $f_{app}Re_{\sqrt{A}}$ is calculated from Eq. 3.16. R_{th} is related to the Nu through the following expression:

$$R_{th} = \frac{1}{hPL} = \frac{\sqrt{A_{cs}}}{Nu_{\sqrt{A_{cs}}}\,k\,PL} \tag{3.48}$$

the heat transfer term of the entropy generation will then be:

$$\dot{S}_{gen,\dot{Q}} = \frac{\dot{Q}^2 R_{th}}{T_H^2} = \frac{\dot{Q}^2}{T_H^2}\frac{\sqrt{A_{cs}}}{k\,PL}\left(\frac{1}{Nu_{\sqrt{A_{cs}}}}\right) \tag{3.49}$$

where $Nu_{\sqrt{A}}$ is obtained from Eq. 3.17. By summing the heat transfer and friction terms of the entropy generation, the following expression for the total entropy generation rate is obtained:

$$\begin{aligned}\dot{S}_{gen} &= \dot{S}_{gen,\dot{Q}} + \dot{S}_{gen,\Delta p}\\ \dot{S}_{gen} &= \frac{\dot{Q}^2}{T_H^2}\frac{\sqrt{A_{cs}}}{k\,PL}\left(\frac{1}{Nu_{\sqrt{A_{cs}}}}\right) + \left(fRe_{\sqrt{A}}\frac{L}{\sqrt{A_{cs}}}\frac{P}{\sqrt{A_{cs}}} + K_L\right)\frac{\dot{m}^2\mu\sqrt{A_{cs}}}{2T\rho^2 A_{cs}^2} \qquad (3.50)\end{aligned}$$

In order to non-dimensionalize the above relationship, we divide both sides by:

$$\frac{\dot{Q}^2}{T_H^2}\frac{\sqrt{A_{cs}}}{k\,PL} \tag{3.51}$$

the resulting equation is:

$$\frac{\dot{S}_{gen}}{\dfrac{\dot{Q}^2}{T_H^2}\dfrac{\sqrt{A_{cs}}}{k\,PL}} = \left(\frac{1}{Nu_{\sqrt{A_{cs}}}}\right) + \left(fRe_{\sqrt{A}}\frac{L}{\sqrt{A_{cs}}}\frac{P}{\sqrt{A_{cs}}} + K_L\right)\frac{1}{2}\mu T\,k\frac{V^2 PL}{\dot{Q}^2} \tag{3.52}$$

the term on the left hand side is the non-dimensional entropy generation, defined as:

$$\Psi_{gen} = \frac{\dot{S}_{gen}}{\dfrac{\dot{Q}^2}{T_H^2}\dfrac{\sqrt{A_{cs}}}{k\,PL}} \tag{3.53}$$

another non-dimensional term that arises in Eq. 3.52 is:

$$\Theta = \frac{1}{2}\mu T\,k\frac{V^2 PL}{\dot{Q}^2} \tag{3.54}$$

parameter Θ is a distribution ratio, showing the relative contributions of viscous dissipation and heat transfer to the entropy generation. Substituting Θ and Ψ into Eq. 3.52 results in the following non-dimensionalized form of Eq. 3.52:

$$\Psi_{gen} = \left(\frac{1}{Nu_{\sqrt{A_{cs}}}}\right) + \left(fRe_{\sqrt{A}}\frac{L}{\sqrt{A_{cs}}}\frac{P}{\sqrt{A_{cs}}} + K_L\right)\Theta \tag{3.55}$$

The non-dimensional entropy generation is a function of the following non-dimensional parameters: $L/\sqrt{A_{cs}}$, $P/\sqrt{A_{cs}}$, Re, Pr, ε, Θ, σ, and K_L.

As the Reynolds number increases, the length of the thermally developing flow also goes up. Due to the higher temperature gradient at the wall in the developing region, the Nusselt number in that region is higher than in the fully developed region; therefore, there is a decrease in $\Psi_{gen,\dot{Q}}$ with increasing Reynolds number. On the other hand, for a constant channel cross-sectional area and a specific fluid, the frictional term of the entropy generation, $\Psi_{gen,\Delta p}$, rises with increasing Reynolds number, due to the second order dependence on velocity and the increase in the hydrodynamically developing flow. These trends are shown in Fig. 3.20 a. $\Psi_{gen,\Delta p}$ drops as the aspect ratio rises, due to the decrease in the friction factor with decreasing channel slenderness. However, the $\Psi_{gen,\dot{Q}}$ goes down as the aspect ratio increases, because of the increase in the circumferential area of the duct and thus the heat transfer rate to the fluid, with the cross-sectional area and mass flow rate kept constant. Figure 3.20 b shows $\Psi_{gen,\dot{Q}}$, $\Psi_{gen,\Delta p}$ and $\Psi_{gen,total}$ as a function of aspect ratio. Figures 3.21 a and b show entropy generation as a function of Reynolds number and channel aspect ratio. There is an optimum Reynolds number and aspect ratio for which the entropy generation is minimum. In Fig. 3.22 a comparison has been done between the amounts of entropy generation in the three inlet and exit geometries as a function of Reynolds number, respectively. The effect of rounding the inlet is well presented in this figure. The rounded and triangular geometries produce a much lower entropy than the rectangular entrance due to their lower pressure loss coefficients. However, at the exit of the channel, the entropy generated in the triangular shape is maximum, because of the combined effect of separation and wall friction at the 45° angled diffusers.

The effect of increasing $L/\sqrt{A}$ is shown in Fig. 3.23. As the length of the channel increases, the Nusselt number drops and approaches the fully developed value, thus the heat transfer term of the entropy generation goes up and converges to a constant value. The

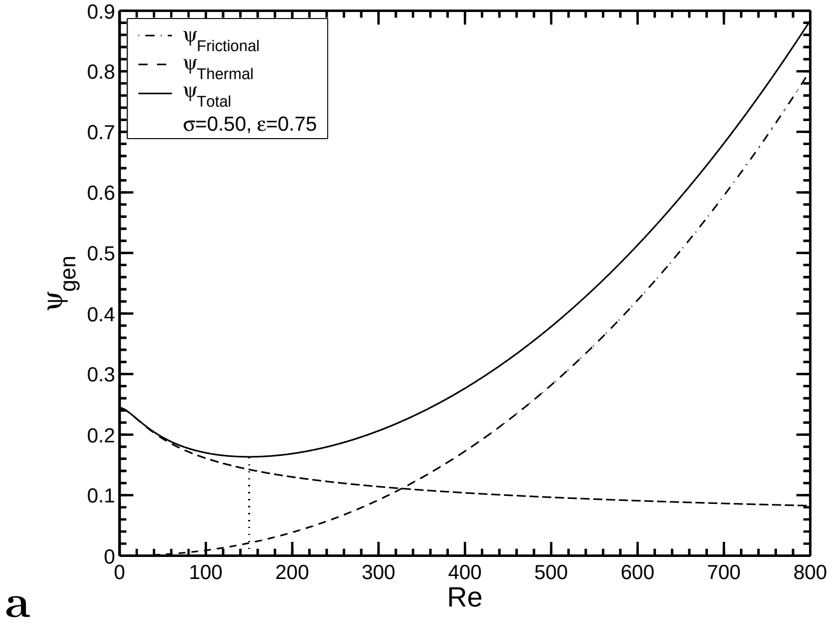

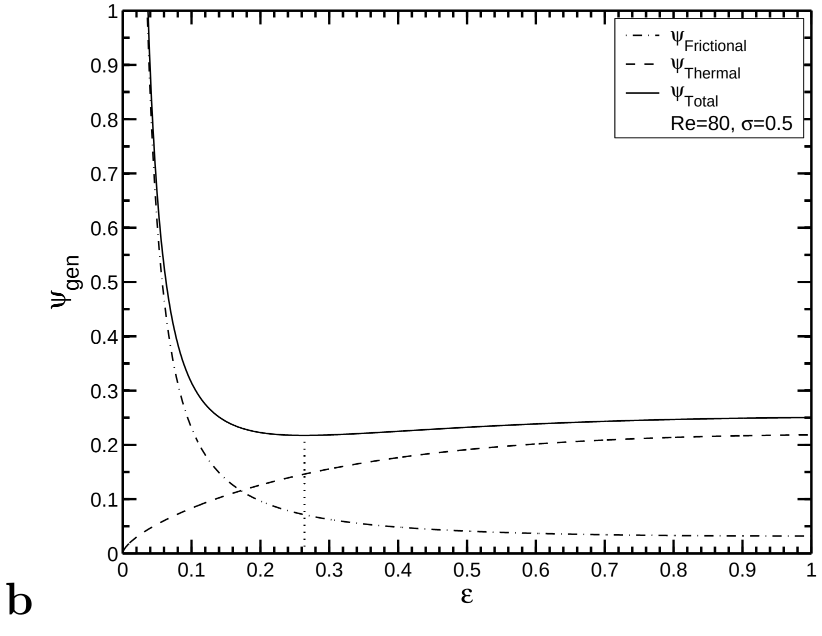

Figure 3.20: Comparison of the total amount of entropy generation with the thermal and frictional components of it as a function of Reynolds number (a) and aspect ratio (b)

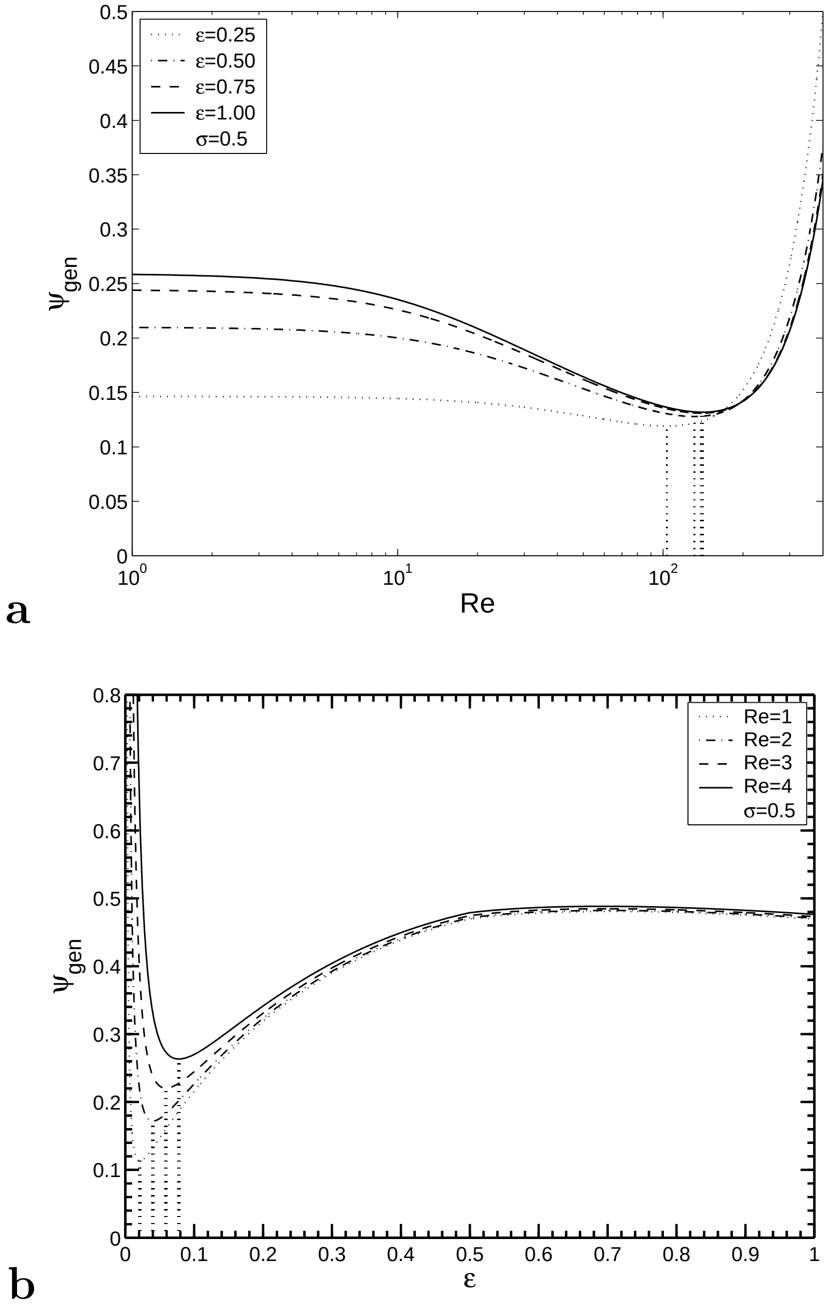

Figure 3.21: Entropy generation as a function of Reynolds number (a) and channel aspect ratio (b)

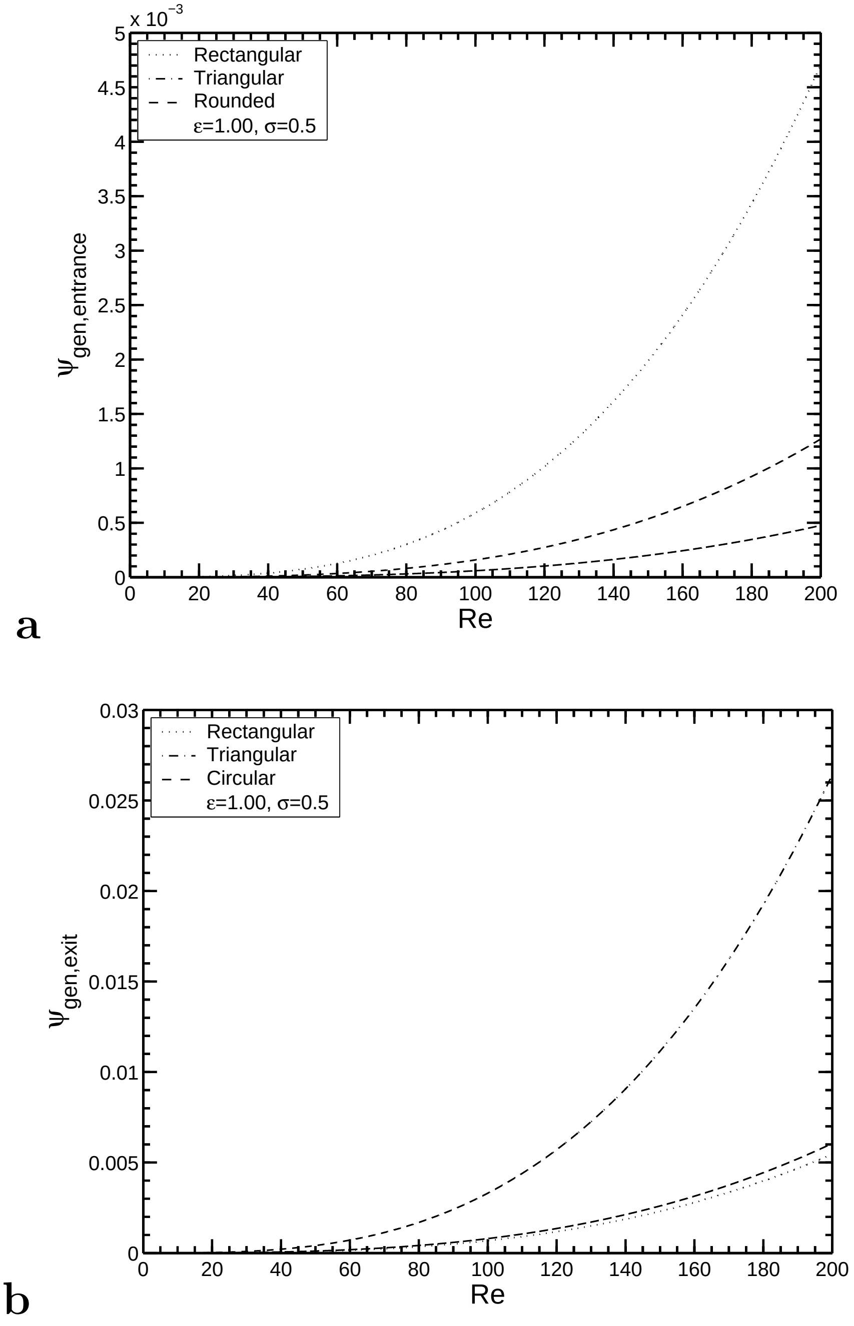

Figure 3.22: Comparison of entropy generation caused by the entrance (a) and exit(b) of the channel for three geometries

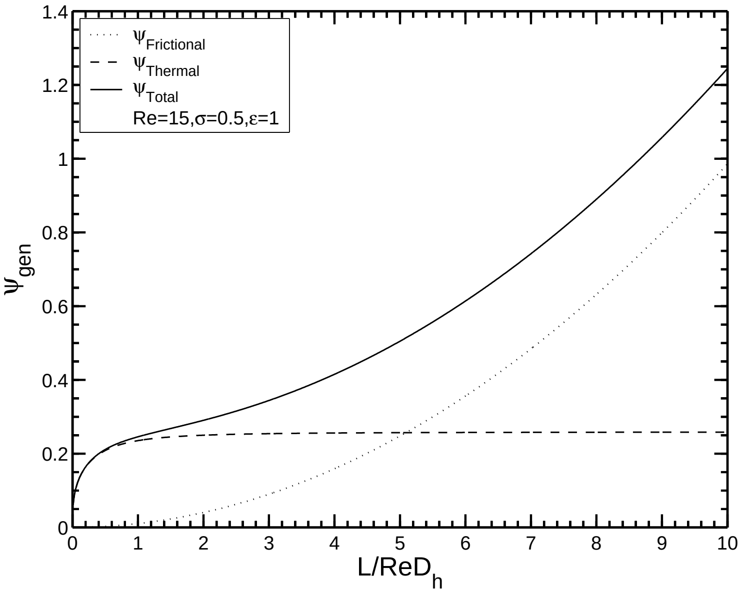

Figure 3.23: Variations in entropy generation in a channel with position

frictional term, however, steadily increases with length of the channel, because of the higher peripheral area over which the shear stresses act to retard the fluid.

Chapter 4

Experimental Study

4.1 Particle Image Velocimetry

Particle image velocimetry (PIV) is a technique which enables instantaneous measurement of the flow velocity at several positions in a plane. The working principle is quite simple. The flow is made visible by seeding it with reflective particles; these particles are then photographed at two different times. The two frames are sectioned into many smaller uniformly spaced areas, called interrogation regions. The usual method for determining the motion of particles in the two images separated by a small finite time step, each with only one illumination, is called cross-correlation (see Fig. 4.1). The cross correlation function for the interrogation region (i, j) is [25]:

$$\Gamma(m,n) = \sum_{j=1}^{q} \sum_{i=1}^{p} f(i,j) \cdot g(i+m, j+n) \tag{4.1}$$

where Γ is the cross-correlation function, (m, n) is the pixel offset between the images, f and g are the image intensity distributions of the first and second images, respectively, and (p, q) is the distance around the first interrogation region which is looked for by the algorithm. The location of the peak of the correlation function determines the displacement of the particles

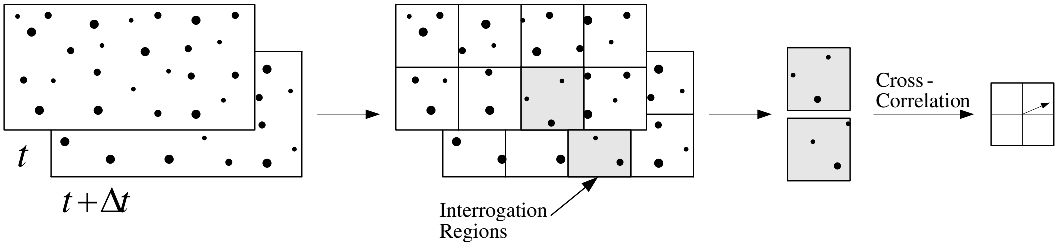

Figure 4.1: Determining the velocity vector field with the Particle Image Velocimetry method

in the interval Δt. This chapter concentrates on how PIV is different at the micro scale and the principles of a micro-PIV system.

4.2 Fundamental Physical Considerations of Micro-PIV

The following three fundamental problems differentiate micro-PIV from regular PIV [3]:

1. The diameter of the tracer particles is small compared to the wavelength of the illumination light.
2. The particles are sufficiently small that the effect of Brownian motion must be considered.
3. The illumination field is not a light a sheet but rather a volume element within the flow field. The difference is shown schematically in Fig. 4.2.

4.2.1 Small Particles

The flow-tracing particles must always be large enough to scatter sufficient light so that their image can be recorded. When particles are small compared to the wavelength of the

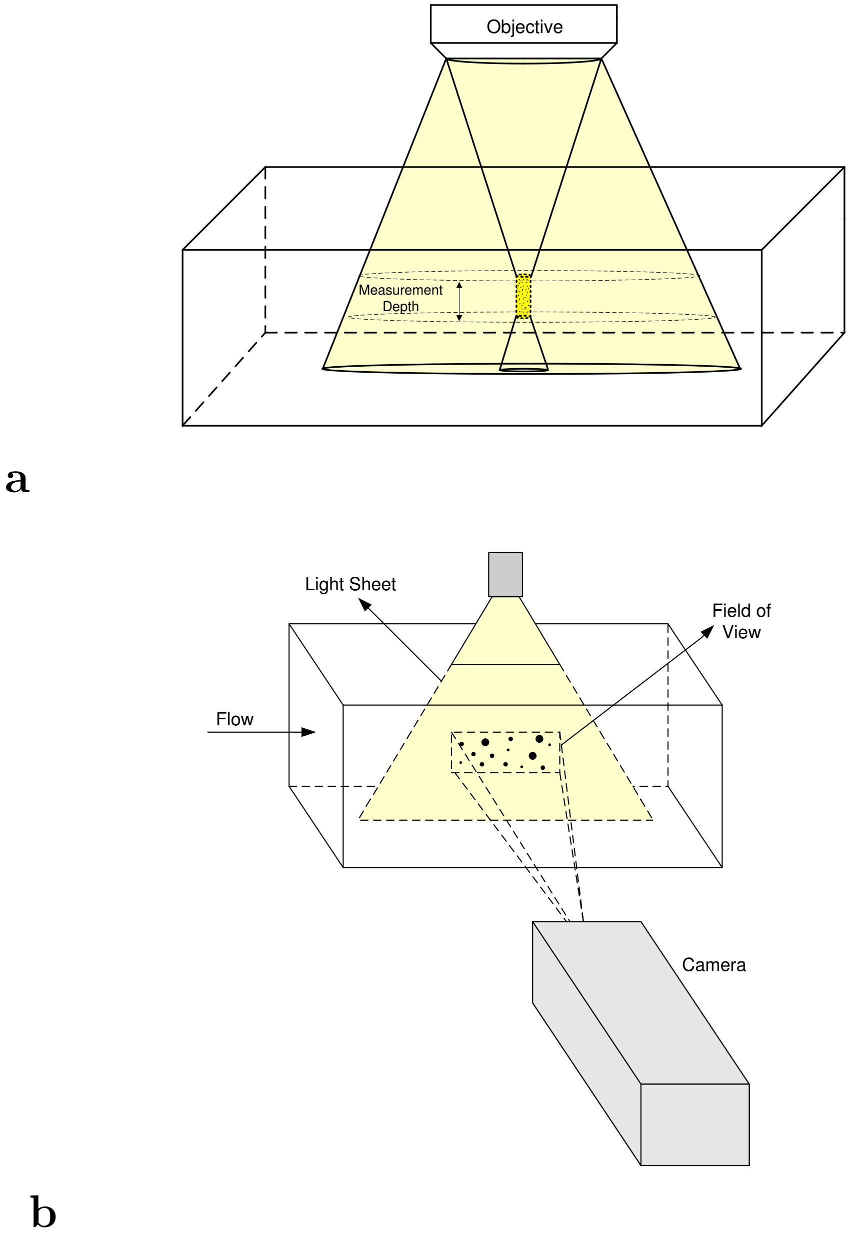

Figure 4.2: (a) Volume illumination and measurement plane in micro-PIV. (b) Light sheet illumination in macro-PIV

illumination light source, i.e. $d \ll \lambda$, we are in the Rayleigh scattering regime. In this regime, the amount of light scattered by a particle is proportional to d^6. In micro-PIV the size of the particles should be small enough so that they do not disturb the flow; therefore, the diameter of the particles is typically between 50 nm to 500 nm. The wavelength of the illumination light is 532 nm and as a result we are approaching the Rayleigh scattering regime in which the amount of scattered light is very small and image recording is extremely difficult. This fact puts significant constraints on the image recording optics.

One solution to this problem is using particles covered with fluorescent dye, which reflect light at a wavelength higher than the illumination light, and optical wavelength-specified long pass filters which remove the background light and transmit only the fluorescent light reflected from the particles.

Fluorescent particles

Fluorescence is the process in which a fluorescent dye absorbs light in one wavelength and emits energy at a longer wavelength. The fluorescence process is composed of three phases. The first phase of the process is excitation, during which a photon from a light source is absorbed by the fluorophore[1]. The absorbed photon makes it unstable by raising the energy level and electronic state of the fluorophore. The second stage of the process is the period over which the fluorophore remains in the excited state, and lasts for 1-10 nano seconds. During this stage, the conformational changes in the fluorophore cause some of the absorbed energy to dissipate. The third part of the process is emission, in which a photon is released from the fluorophore, returning it to the stable base energy level. Due to the lower energy level of the fluorophore, the wave length of the emitted light is longer than that of the incident light. The fluorophore can repeat this cycle assuming that it has not been damaged by photo-bleaching. Photo-bleaching is the irreversible damage to the fluorophore due to

---

[1] Fluorophore is the component of a molecule which causes the molecule to be fluorescent.

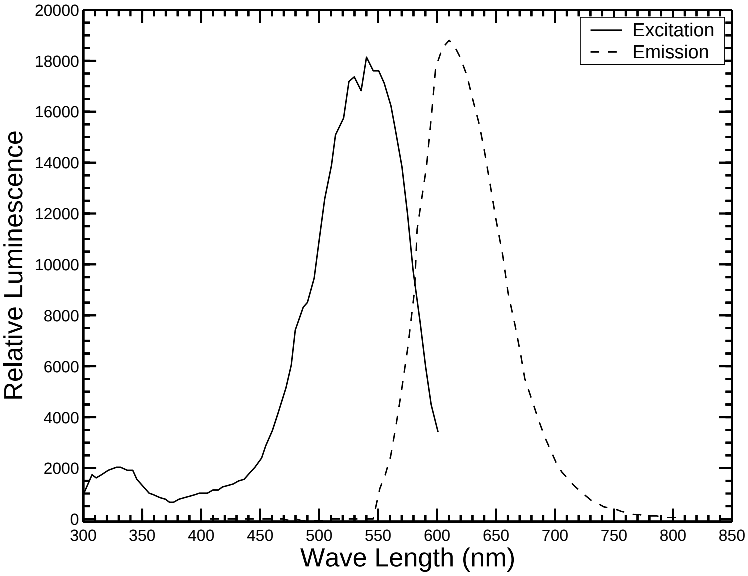

Figure 4.3: Excitation and emission spectra of Duke Scientific red fluorescent particles [20]

high intensity or prolonged illumination. The fluorophore is no longer able to fluoresce if photo-bleaching occurs. Figure 4.3 shows the excitation and emission spectra of the Duke fluorescent particles, used in this work. The maximum excitation wavelength is 542 nm and the emission maximum wavelength 612 nm. In this work, the illumination light is 532 nm green light coming from a Nd-YAG double pulse laser which corresponds to a 560 nm red emission light from the fluorescent particle.

4.2.2 Effect of Brownian Motion

When the size of the particles is very small, the collective effect of collisions between the particles and the fluid molecules is unbalanced, preventing the particle from following the flow. This phenomenon is called Brownian motion and causes errors in measurement of flow velocity. The velocity spectrum of particles due to Brownian motion consists of frequencies too high to be resolved; therefore, the average displacement of the particles after several fluctuations is used to quantify the intensity of Brownian motion. For a time interval Δt, much lager than the particle's response time[2], the dynamics of Brownian motion are independent of inertial parameters, such as particle and fluid density, and the mean square distance of diffusion is proportional to $D\,\Delta t$:

$$\begin{aligned} \sigma_x^2 &= 2D\Delta t \\ \sigma_y^2 &= 2D\Delta t \end{aligned} \tag{4.2}$$

where D is the diffusion coefficient of the particles, and σ_x^2 and σ_y^2 are the mean square displacements in $x-$ and $y-$ directions. For small spherical particles subjected to Stoke's drag law, the diffusion coefficient is:

$$D = \frac{\kappa\, T}{3\,\pi\,\mu\, d_p} \tag{4.3}$$

In the above relationship, κ is Boltzmann's constant[3], T is the absolute temperature, μ is the dynamic viscosity of the fluid, and d_p is the diameter of the particle.

The random Brownian motion causes the particles to fluctuate about the main pathlines of the flow field. Assuming a steady flow, the particle motion can be considered as a fluctuation about a streamline that passes through the particles initial location. The displacement of an ideal non-Brownian particle after a time period of Δt is:

$$\begin{aligned} \Delta x &= u\,\Delta t \\ \Delta y &= v\,\Delta t \end{aligned} \tag{4.4}$$

where u and v are the local velocity components of the flow in the $x-$ and $y-$ directions, respectively. The relative errors incurred because of the Brownian displacements in a two-

---

[2] See section 4.3.

[3] Boltzmann's constant $= 1.3806503\times10^{-23}\frac{m^2 kg}{s^2 K}$

dimensional velocity field are:

$$\begin{aligned}\epsilon_x &= \frac{\sigma_x}{\Delta x} = \frac{1}{u}\sqrt{\frac{2D}{\Delta t}} \\ \epsilon_y &= \frac{\sigma_y}{\Delta y} = \frac{1}{v}\sqrt{\frac{2D}{\Delta t}} \qquad (4.5)\end{aligned}$$

by substituting for D from Eq. 4.3 we obtain:

$$\begin{aligned}\epsilon_x &= \frac{1}{u}\sqrt{\frac{2\,\kappa\,T}{\Delta t\,3\,\pi\,\mu\,d_p}} \\ \epsilon_y &= \frac{1}{u}\sqrt{\frac{2\,\kappa\,T}{\Delta t\,3\,\pi\,\mu\,d_p}} \qquad (4.6)\end{aligned}$$

The Brownian errors put a lower limit on the time interval, Δt, between the two frames. For large time intervals, the flow displacements which are proportional to Δt, are dominant while for short intervals the random Brownian motions, proportional to $\sqrt{\Delta t}$, are dominant. As a result, the uncertainty can be reduced by increasing the time interval between the images. It should be noted that the accuracy of the measurements drops with increasing Δt, because they are based on first order accurate approximations[4]. The error may be reduced by averaging over several particles in an interrogation region or by averaging over several realizations on the same spot. The decrease in error is proportional to $1/\sqrt{N}$, where N is the total number of particle pairs in the average. The error caused by the Brownian motion is less for faster flows, however, Δt is usually smaller for high velocity flows.

4.2.3 Volume Illumination

The third fundamental difference between micro-PIV and regular PIV is that, due to a lack of optical access and significant diffraction in the light sheet forming optics, it is not practical to generate a sheet of light, thin enough for micro-scale illumination. Instead, an

---

[4] $u = \Delta x/\Delta t + u'\Delta t/2 + \mathcal{O}(2)$ where $u'\Delta t/2 + \mathcal{O}(2)$ is the error associated with the first order approximation of velocity.

epiflourescent[5] microcopy technique is used in which the flow is volume illuminated; leaving two choices for us to visualize the particles; with an optical system whose depth of field is larger than the depth of the device or with an optical system whose depth of field is small compared to the depth of the flow. The advantage of the former type of imaging system is that all particles are well focused and contribute to the velocity measurement. But on the other hand, all the information about the depth of particles is lost and the measurement is depth-averaged. Particles that are within the measurement depth are sharply focused. The remaining particles are unfocused and contribute to the background noise. In a micro-PIV application, the optical system defines the depth of field, or more accurately, the thickness of the measurement plane (δz_m), and it is important to characterize the thickness of the measurement plane.

Measurement Depth

The measurement depth of the volume-illuminated PIV can be defined as twice the distance from the center of the object plane at which a particle can be located such that its maximum image intensity is an arbitrarily specified fraction of its maximum in-focus intensity. Beyond this distance, the particle-image intensity is sufficiently low that it will not significantly contribute to the velocity measurement. The theoretical contribution of an out-of-focus particle to the correlation function is estimated by considering the effect due to diffraction, the effect due to geometrical optics, and the size of the particle. For the micro-PIV system used in this work, the cut-off for the on-axis image intensity is chosen to be arbitrarily a tenth of the in-focus intensity. Meinhart et al. [39] suggested the following expression to find the micro-PIV measurement depth:

$$\delta z_m = \frac{3n\lambda_0}{NA^2} + \frac{2.16\,d_p}{\tan\theta} + d_p \tag{4.7}$$

---

[5] Epifluorescent microscopy means that the illumination of the test section and imaging the fluorescent particles are done through the same optical axis.

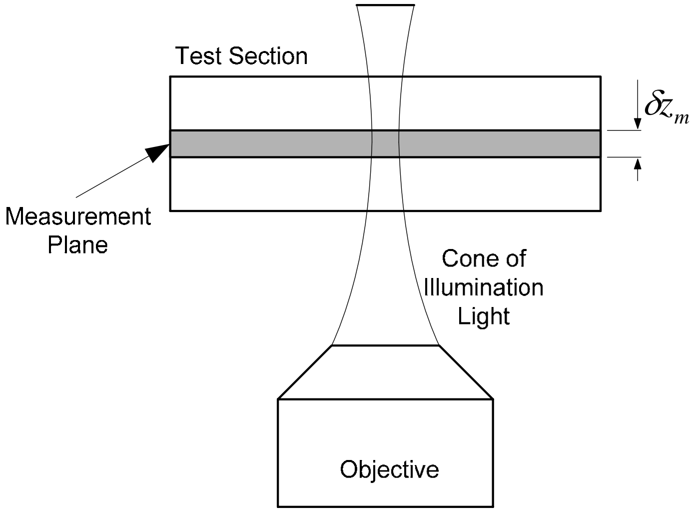

Figure 4.4: Measurement plane in a volume illuminated flow field

In this work, $NA = 0.3$, $n = 1.00$, $\lambda_0 = 532\,nm$, $d_p = 500\,nm$, $\theta = 17°$, and therefore $\delta z_m \approx 22\,\mu m$. The first term on the right hand side shows the effect of diffraction which has been evaluated by considering the intensity of a point source of light along the optical axis. The second term shows the effect of geometrical optics which is estimated by considering the distance from the object plane in which the intensity of a particle of diameter d_p along the optical axis decreases by an amount of 0.1, and the third term is the diameter of the particle. A schematic of the measurement plane in a volume illuminated flow is shown in Fig. 4.4.

4.3 Particles

The seeding particles should have a density which closely matches the working fluid, so that they are not affected by buoyancy and gravitational forces. The particles used in this work are made of polystyrene with a specific gravity of 1.05 which is close to that of the working

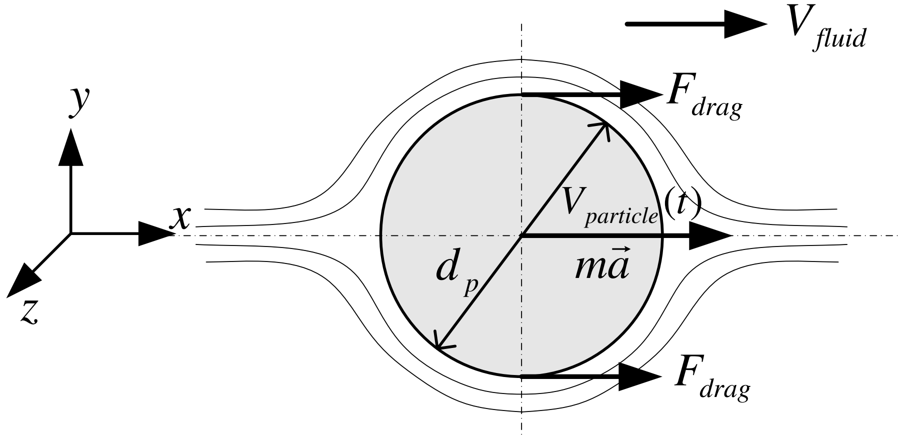

Figure 4.5: Forces acting on a particle in the flow

fluid, in this case, deionized water. The particles should preferably have a diameter of 200-700 *nm*. Smaller particles are subjected to Brownian motion and can not faithfully follow the flow, while larger particles decrease the accuracy and resolution of the measurements.

Particle dynamics

The size of the particles is a measure of their ability to follow the flow, based on the ratio of the drag force to the inertial force. In contrast to macro-scale experiments, the size of the particles is not a concern in micro-PIV experiments, because of the large surface area to volume ratio in micro-scale and the resulting increase in the ratio of drag to inertial force. In order to gauge the behavior of a particle in response to changes in flow velocity, a simple model for the response time of a particle to a step change in flow velocity is developed. We start from the momentum equation in the flow direction for a spherical particle suspended in the flow (see Fig. 4.5). The particle starts to move from rest due to a step change in fluid velocity. The momentum balance equation for the spherical particle in the flow is:

$$F_x = ma_x = \rho_p \pi \frac{d_p^3}{6} \frac{dV_p(t)}{dt} \tag{4.8}$$

where d_p, and ρ_p are the diameter and density of the particle, respectively. V_p is the particle velocity which varies from 0 to V_{fluid}. F_x and a_x are the force and the acceleration of the particle in the direction of the flow, respectively. If the particle moves horizontally, the gravity and buoyancy do not contribute to the overall forces in the flow direction and only the drag force is considered. Due to the sub-micron diameter of the fluorescent particles used in micro-PIV measurements, the Reynolds number of the flow is very small. The Reynolds number of a typical particle used in this study is:

$$Re_p = \frac{\gamma \rho_{H_2O} V_{ave,\max} d_p}{\mu} = \frac{1.05 \times 998 \times 0.83 \times 500e-9}{1.003e-3} = 0.43 \tag{4.9}$$

γ is the specific gravity of Duke Scientific fluorescent particles used in this work and $V_{ave,\ \max}$ is the largest average velocity in this study, and μ is the dynamic viscosity of the fluid. For Reynolds numbers less than 0.5, Stokes law can accurately predict the drag force acting on a spherical particle [40]:

$$F_{drag} = 3\,\pi\,\mu\,d_p\,\left(V_{fluid} - V_p(t)\right) \tag{4.10}$$

Substituting F_{drag} into Eq. 4.8 and integrating yields:

$$V_p(t) = V_{fluid}\left(1 - e^{(-t/\tau)}\right) \tag{4.11}$$

where $\tau = (\rho_p\,d_p^2)/(18\,\mu)$ is the response time of the particle. For the particles used in this work,

$$\tau = \frac{1.05 \times 998 \times (500e-9)^2}{18 \times 1.003e-3} = 1.451e-8\,s \tag{4.12}$$

The smallest time delay between the two frames is $5.5\,\mu s$ when the flow rate is $500\,\mu l$ min. Using Eq. 4.11, it takes $6.6959e-8\,s$ for the particle to reach 99% of the fluid velocity, which is about 100 times smaller than the delay between two frames. We can conclude that the particles' response to flow velocity changes is fast enough to be realized by the micro-PIV system and that they follow the flow very faithfully.

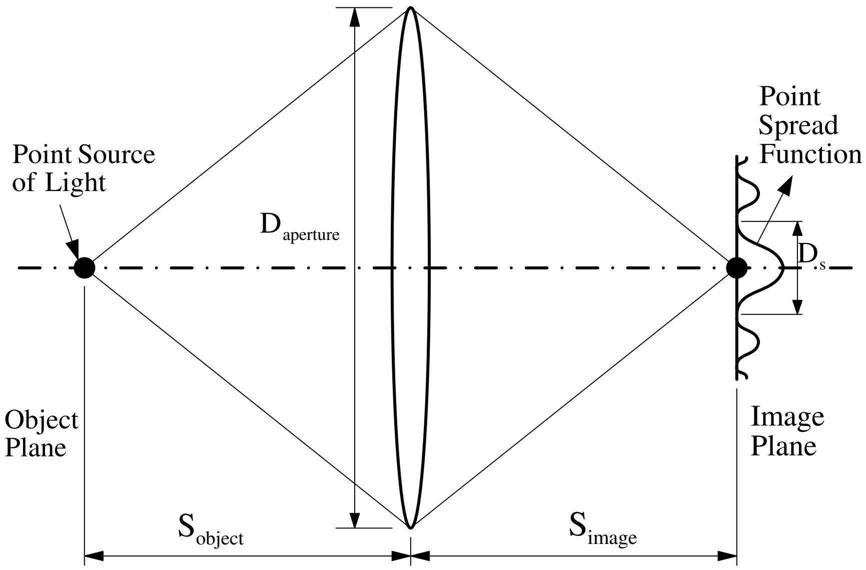

Figure 4.6: The recorded image of a point source of light

4.4 Spatial Resolution and Accuracy

The image of a point source of light through a circular aperture is in the form of an Airy function. The diameter of the point spread function is defined as the diameter of the first dark ring in the image (See Fig. 4.6) and can be estimated by the following relationship [41]:

$$d_s = 2.44(M+1)\, f^{\#}\lambda \tag{4.13}$$

where M is the magnification of the lens, $f^{\#}$ is the f-number of the lens and λ is the wavelength of the light. The f-number is basically the focal length of the objective divided by its aperture diameter and for an infinitely corrected objective, can be determined from the following relationship [39]:

$$f^{\#} \approx \frac{1}{2}\left[\left(\frac{n}{NA}\right)^2 - 1\right]^{1/2} \tag{4.14}$$

Numerical aperture, NA, characterizes the range of angles over which the lens can accept or emit light and is defined as:

$$NA = n\,\sin\theta \tag{4.15}$$

where n is the index of refraction of the recording medium[6], and θ is the half-angle of the maximum cone of light that can enter or exit the lens.

The actual diameter of the recorded image of the particles can be estimated as the convolution of the point-spread function and the geometric image. Approximating these functions as Gaussian, the effective image diameter will be:

$$d_e = \left(M^2 d_p^2 + d_s^2\right)^{1/2} \tag{4.16}$$

In this work, a Nikon Plan Fluor objective with a magnification of 10, and numerical aperture of 0.3 has been used. The imaging medium [7] is air, with a refractive index of 1, and diameter of the tracer particles is 500 nm. By substituting these values into Eqs. 4.13, 4.14, and 4.16, we can determine the effective image diameter:

$$d_e = 46.70\,\mu m \tag{4.17}$$

The effective particle image diameter places a bound on the spatial resolution of the measurements. If the particle images are sufficiently big to be resolved by the CCD[8] camera within 3-4 pixels in diameter, the location of the correlation peak can be detected by curve fitting and interpolation to ±1/10 of the effective particle image diameter. Therefore, the correlation peak in this work can be determined in the image plain within $\pm 4.67\mu m$. The uncertainty in the measurement of displacement can be determined by projecting this value back into the flow:

$$\delta x = \frac{\frac{1}{10} d_e}{M} = 233.50\,nm \tag{4.18}$$

---

[6] 1.0 for air, 1.33 for pure water, and up to 1.56 for oils and glass

[7] The medium between the lens and the microchannel

[8] Charge Coupled Device (see Sec. 4.5 for more details)

The measurement error due to detectability, ϵ_d, can be written as the ratio of the measurement uncertainty to the displacement, Δx:

$$\epsilon_d = \frac{\delta x}{\Delta x} \tag{4.19}$$

The in-plane resolution of the measurements is proportional to the particle displacement. As a rule of thumb, the length of the interrogation windows along the flow direction should be about 4 times larger than the particle displacements. Equation 4.19 clearly shows the trade off between in-plane resolution and the accuracy of the measurements. Larger displacements are required in order to obtain smaller errors while larger errors can be expected with higher in-plane resolutions.

4.5 Hardware Implementation

A schematic of a micro-PIV system is presented in Fig. 4.7. The mono-chromatic pulsed Nd:YAG[9] laser, from New Wave Research Inc. is chosen as the illumination source because of its high illumination intensity. Pulsed lasers need some time to build up energy before they can deliver a new pulse and the two images in a PIV image pair have to be taken within a short period of time; therefore, the lasers designed for PIV applications have two cavities. The laser pulses have a duration time of about 5 ns and the energy in each pulse is $30\,mJ$. Nd:YAG lasers emit light with a wavelength of 1064 nm which is in the infrared range. For micro-PIV purposes we need a wavelength of 532 nm. For this reasons the wavelength of the Nd:YAG laser is halved, using a device called a harmonic generator, so that it becomes 532 nm. The harmonic generator is not 100% efficient and therefore a separator and an IR-dump is needed to get rid of the remaining IR-light. The laser light is delivered to the microscope via a 1.5 m long liquid-filled light guide and several beam forming optics and

---

[9] Neodymium Yttrium Aluminum Garnet

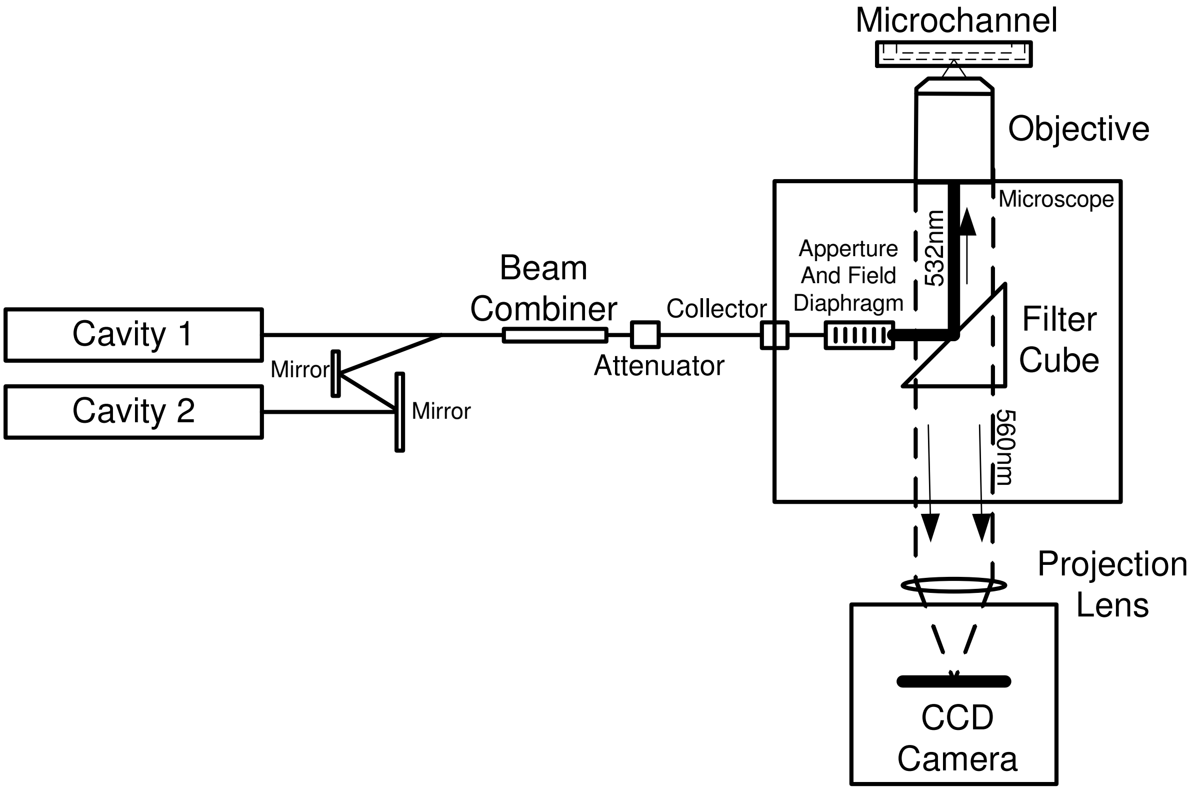

Figure 4.7: The schematic of the micro-PIV system

filters. The Nikon TE-2000E inverted microscope, which provides sufficient free space on its stage, is used. As stated earlier, a Nikon Plan Fluor objective with a magnification of 10 and numerical aperture of 0.3 is used. In order to obtain higher resolutions, objectives with higher numerical aperture and magnification could be used at the expense of reduced working distance and field of view.

Micro-PIV puts specific demands on the camera used to record the images [42]. When the imaged area is very small, as in microfluidic measurements, the camera needs to be able to capture two images within a very short period of time so that the same particles appear in both images. This requirement is achieved by using a progressive scan architecture. Cameras

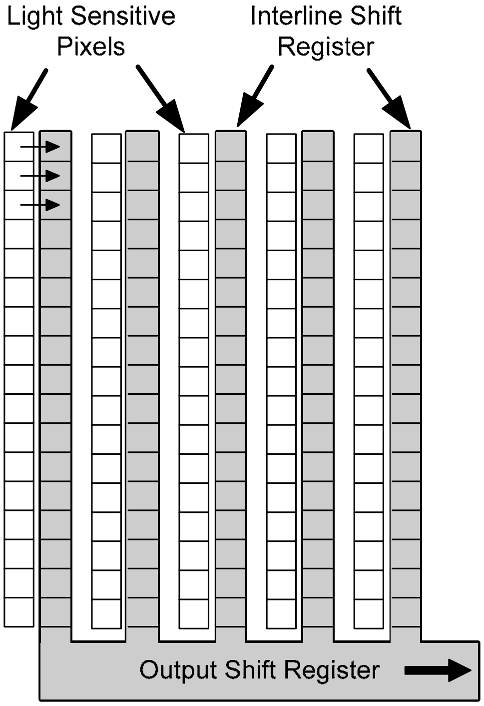

Figure 4.8: Progressive scan camera sensor

with progressive scan architecture can take two images with less than 1 μs delay. Figure 4.8 shows the layout of such a sensor. Directly after the first image has been recorded the charge of each pixel is transferred to its adjacent position in the interline shift register. A new image can now be recorded by the pixels. The second image is exposed until the first image has been read out from the interline shift register and is then transferred to the image buffer in the same way. Therefore, the second image will be exposed for a longer time.

For the submicron particles used in micro-PIV, with very low reflected light intensity, the camera needs to have a high sensitivity to incident light. The sensitivity of a photon sensor such as a CCD-camera is measured in QE (quantum efficiency) which is the average number of electrons that are released from the sensor when it is hit by a photon. The camera used in this work is a 14-10 PIVCAM from TSI Inc. with a CCD size of 1376 pixel × 1040 pixel and a pixel size of 6.45 μm. In order to remove temperature induced noise on the CCD, it is cooled with air and maintained at a temperature of -12°C. The minimum delay between two frames is 200 ns and the quantum efficiency is 62% at an incident wavelength of 500 nm [43]. The computer controlled Laser Pulse 610035 synchronizer from TSI is used to coordinate the timing of laser pulses and camera frames with each other.

4.5.1 Filter Cube

The heart of the micro-PIV system is the filter cube. The fluorescent light is emitted from the fluorophore dye on the particles and we want only this light to reach the camera. As stated earlier, the fluorescent emission is at a longer wavelength than the excitation light. The filter cube is a group of optical filters that separates short wavelength illumination light from long wavelength fluorescent emissions. The optical filters are the Exciter, the Dichroic Mirror, and the Barrier. The Exciter filter selects the illumination light, with the wavelength of 532 nm, from the broadband light source. If the light source is an Nd:YAG laser which emits a single wavelength, the Exciter is not required. But, if the light source is a xenon or mercury lamp, the Exciter only lets a specific, narrow wavelength range pass to illuminate the object. The Dichroic Mirror, has a coating that reflects the illumination wavelength and transmits the fluorescent wavelength; i.e. it is a mirror at the illumination light wavelength and a clear glass at the fluorescent emission wavelength. The wavelength versus transmission graph of the Dichroic Mirror is shown in Fig. 4.9. The Dichroic Mirror has almost zero transmissivity (high reflectivity) for 532 nm illumination light, and the illumination light scattered from the test section is reflected back towards the light source. For the 560 nm fluorescent emission, about 80% of the light is transmitted through the dichroic. The illumination and reflected laser light paths are shown in Fig. 4.10. A small percentage of the reflected laser light can pass through the Dichroic Mirror. The Barrier filter is used to block the remaining reflected laser light, so that it can not reach the camera or eyepieces. The transmission of

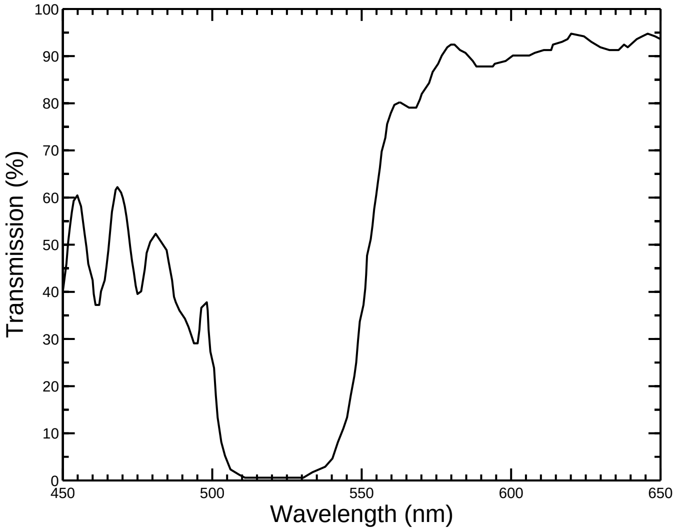

Figure 4.9: Wavelength versus transmission graph of the Dichroic Mirror

the Barrier filter versus wavelength is shown in Fig. 4.11. The Barrier has a sharp cutoff to effectively block the illumination wavelength while passing the reflected fluorescent emission wavelengths. The fluorescent emission light path is shown in Fig. 4.12.

4.6 Capturing and Processing Parameters

The timing parameters are set so that the camera captures two consecutive singly exposed images. The Laser Pulse Delay is adjusted to pulse the laser exactly at the end of the first frame. *Pulse Separation*, i.e. the delay between the firing of the $\mathcal{Q}$-switch 1 and the $\mathcal{Q}$-switch 2, is the key parameter in matching the PIV system with the flow parameters. The delay should be adjusted so that the particle displacements are roughly 1/4 the size of the interrogation regions. *PIV Exposure*, the time that the camera shutter is open for capturing the first frame, also depends on the flow rate. *Pulse Repetition Rate*, which specifies the delay from the start of a laser pulse sequence to the start of the next sequence, is $4.83\,Hz$, the maximum allowable frequency of the laser. A schematic of the timing diagram is shown

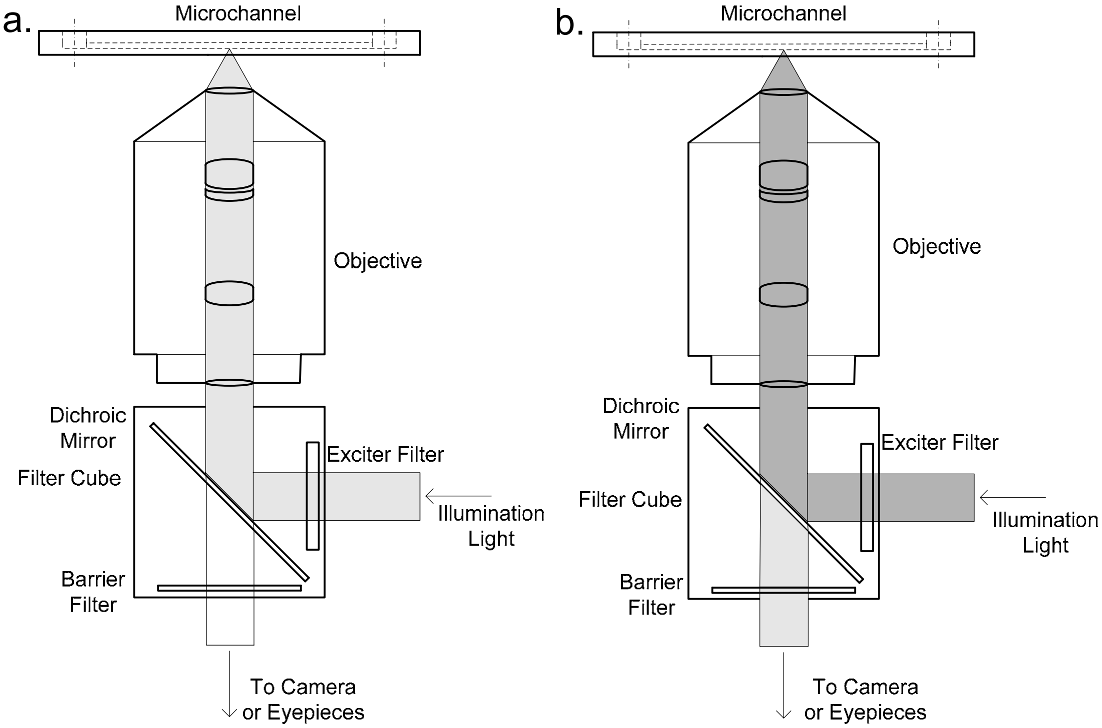

Figure 4.10: The illumination (a) and reflected (b)laser light paths

in Fig. 4.13. The values of the laser pulse delay and PIV exposure are given in Table 4.1. Background subtraction, a method of increasing the signal to noise ratio of PIV images, is used in this work. The minimum intensity image is an estimate of the background light level. In the seeded area of the flow, the minimum will be when a particle is not at a pixel location. When a large enough number of image pairs are used to create the minimum intensity image, the possibility that a particle is present at a specific location in all images in the sequence of images decreases; in other words, an image of flow without seeding particles emerges. If there are any particle images left, they are stationary particles adhered to the surface of the channel. The minimum intensity image is useful for finding stationary particles, walls, and scratches on the flow model. If the images in the sequence are subtracted from the minimum intensity image, these sources of noise will be eliminated.

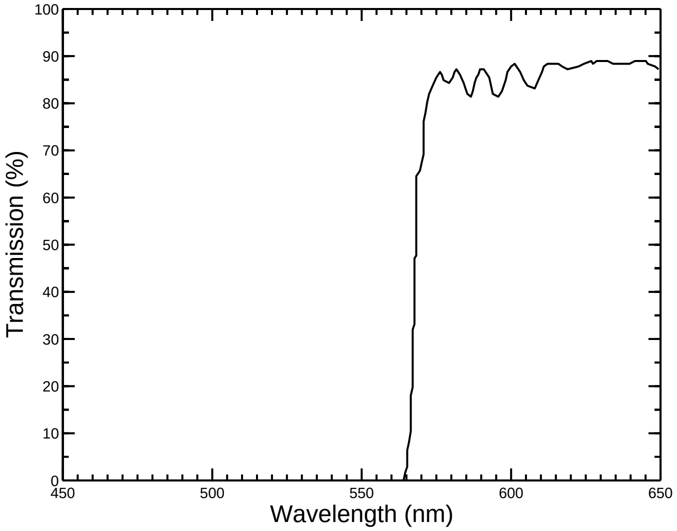

Figure 4.11: Barrier filter's transmission versus wavelength diagram

The *Nyquist Grid Generator* (see [44]), used in this work, creates a uniformly spaced grid with a 50% overlap, i.e. an x-spacing equal to half of the spot width and a y-spacing equal to half of the spot height. To increase the accuracy and resolution, the Recursive Nyquist grid generator is used which processes the images in two or more passes. The first processing pass computes the vector field at the starting spot size with the Nyquist grid engine. The result of the first pass is used to optimize the spot offset in the next processing pass. The idea is to spatially shift the second interrogation region by the integer part of the local displacement of the particles calculated in the previous pass. This offset significantly increases the probability of obtaining a valid correlation measurement between the t_1 and t_2 images by directing the algorithm where to look for the particle matches in the second frame. Different offset values are used for each of the measurements in this work, typically between 4 and 10 pixels. The size of the interrogation region in the first processing pass for the first image in the pairs is 64 pixel × 64 pixel and for the second image in the pair is 128 pixel × 128 pixel. If the spot size for the second frame is larger than that for the first frame, it is

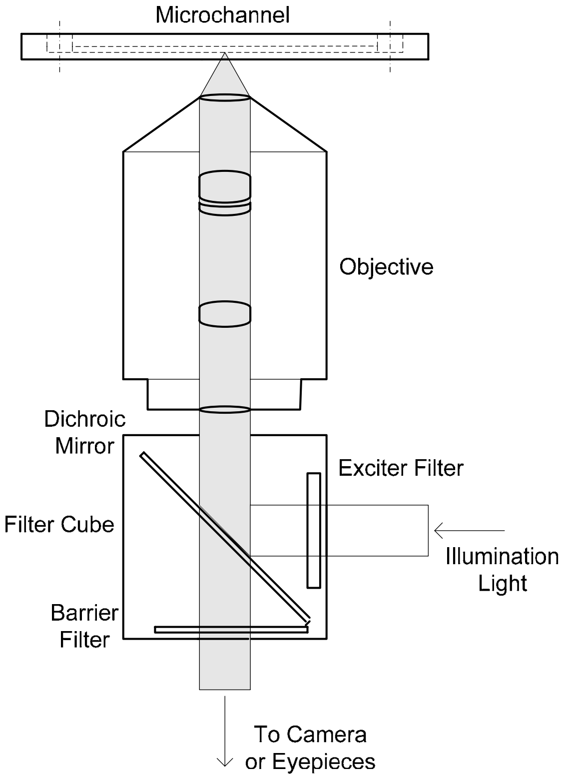

Figure 4.12: The fluorescent emission light path

more likely that all the particles in the first frame are contained in the second interrogation region. It should be noted that the resolution of the measurement is determined by the size of the interrogation region for the first frame. On the second processing pass, the size of the interrogation regions for the first frame is 32 pixel × 32 pixel, and for the second frame is 64 pixel × 64 pixel. If the spot size in the final pass is smaller than that in the starting pass, the spot size is reduced by a factor of two and the number of vector rows and columns also increase by a factor of two, giving four times the number of vectors in each pass.

In a volume illumination technique, the laser light illuminates all particles, including in-focus and out of focus particles located behind and in front of the measurement plane. The out of focus particles fluoresce, but they are a blur in the image instead of sharp particle

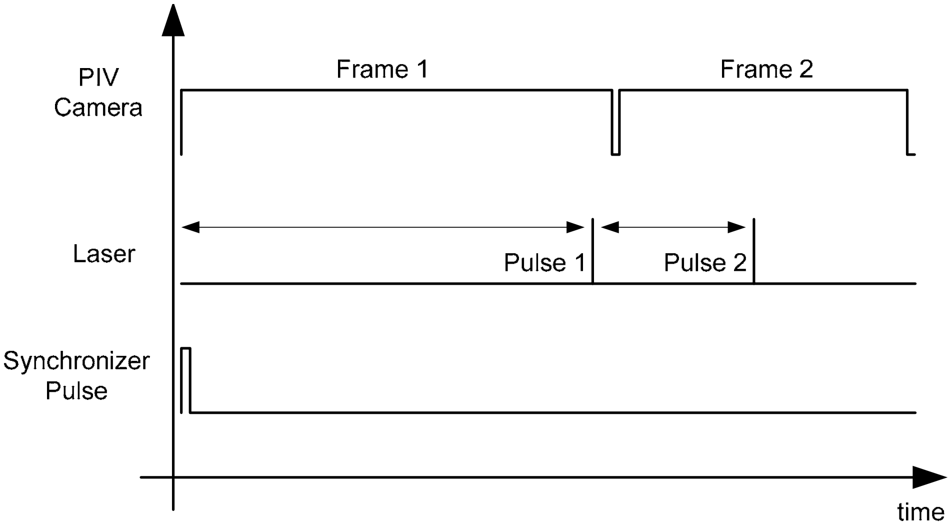

Figure 4.13: The timing diagram for capturing PIV images

images. These out of focus particles contribute to background noise. Increasing the seeding density increases the background noise faster than the in-focus particles' signals; therefore, there is a threshold above which the quality of the images is not acceptable. This threshold usually implies 2-3 particles per interrogation window which is low for good correlation results.

The *Ensemble Correlation Processing* method, used in this study, is an analysis technique used to minimize the problem of low seeding density in micro-flows. Ensemble Correlation combines the correlation maps of individual image pairs. In each image pair there are only a few particles or no particles present. The few particles will contribute to the displacement peak but the noise resulting from mismatch of particles in the two images is also very high. For the next image pair in the sequence at the same spot, the correlation map is computed and added to the previous correlation map. The height of the displacement peak which is at the same location increases, but the height of the noise peaks which are randomly distributed in the interrogation region decrease. As the correlation map of more and more particles is

Table 4.1: The laser pulse delay and pulse separation values in the experiments

Flow Rate ($\mu l/\min$)	Laser Pulse Delay (μs)	Pulse Separation (μs)
100	400	20.0
200	400	13.0
300	401	9.0
400	403	7.0
500	404	5.5

added, the noise peaks average out and as a result, the signal to noise ratio increases. As mentioned earlier, the *Recursive Ensemble Correlation Processing* method is used. After each processing pass, the displacements are measured and used to optimize the spot offset in the next processing pass. The optimization uses the ensemble vector field from the previous pass to generate a new displacement field for interrogation spots in the next pass.

The correlation function is computed using a Fast Fourier Transform. The location of the correlation peak is found with sub-pixel accuracy by fitting a Gaussian curve to the highest pixel and its four nearest neighbors, i.e. the pixels to the left, right, below, and above the peak. The *Maximum Particle Image Displacement* specifies the maximum distance around the interrogation spots in the first frame that is looked for the particle matches. The peak finding algorithm uses this value to limit the correlation map search area to ±(maximum displacement) from the zero pixel displacement. In this work the maximum displacement is 64 pixels. The *Signal To Noise Ratio* filter is enabled with a threshold value of 1.2, i.e. if the ratio of the signal peak to noise peak is less than 1.2, the solution in that spot is rejected.

4.7 PIV Calibration

The purpose of calibration is to determine the length in the flow domain in micrometers that corresponds to 1 pixel in the image domain. The size of the camera pixels are 6.45 $\mu m \times 6.45$ μm, and ideally, dividing 6.45 μm by the magnification of the system, which is 20, should yield the length in the flow domain that corresponds to a unit pixel in the image domain. But in reality, the system goes out of calibration after being used several times due to the changes in the magnification of the system. To perform the calibration, first, the width of the microchannels are determined in microns, using a previously calibrated microscope. The width of each of the microchannels are measured at various locations along the channels with magnification of 20 and 10 and then averaged. Next, the width of the channels are measured with the PIV microscope in pixels at the same locations along the channel and then averaged. The measured values are given in Tables 4.2 and 4.3. Dividing the total mean value of channel lengths in microns by the total mean value of image widths in pixels results in the length of each pixel in the flow domain in microns corresponding to a unit pixel in the image, which is 0.31 $\mu m/px$.

4.8 Velocity Measurements

The measurements in this work are done at a plane in the middle of the channel. The actual height of the channel is measured with a surface profilometer. The location of the measurement plane and channel heights are given in Fig. 4.14. When air immersion objectives are used, a specific displacement of the objective plane, results in $n_{water}/n_{air} = 1.33$ times larger displacement in object plane (Fig. 4.15). Therefore, after focusing on the bottom surface of the microchannel, the objective is moved $H_{ch}/1.33\,\mu m$ in the upward direction to reach the midplane. For focusing on the bottom wall, particles stuck to the wall were found

Table 4.2: Measured values of microchannel widths using the calibrated microscope

Measurement Number	Channel Width (μm)		
	Circular	Rectangular	Triangular
1	122.12	100.58	108.95
2	123.38	98.22	108.99
3	123.44	95.83	107.76
4	122.12	100.58	106.56
5	122.15	95.79	107.76
6	123.34	98.18	108.95
7	124.63	94.59	104.17
8	104.20	100.57	104.15
9	105.46	100.58	104.15
10	104.25	99.38	104.15
11	104.20	99.38	102.95
12	104.20	99.36	104.15
13	106.56	99.38	105.34
14	105.37	99.38	107.73
15	101.86	98.27	106.56
16	105.45	98.18	106.54
17	105.40	99.36	106.54
18	104.25	104.47	104.60
19	105.70	104.47	105.74
20	105.09	105.08	106.34
21	105.09	104.48	106.30
22	103.88	105.12	108.09
23	102.09	105.67	108.07
24	103.87	105.08	108.70
25	105.07	98.51	109.90
26	103.28	99.10	103.32
27	105.69	99.70	104.50
28	105.68	100.58	104.48
Mean	109.54	100.39	106.24
Variance	8.37	3.12	1.9625
L_{ch} = Total Mean = $105.39 \mu m$			
$S_{L_{ch}}$ = Total Variance = $3.78 \mu m$			

Table 4.3: Width of microchannels measured using a calibrated microscope

Measurement Number	Channel Width ($pixel$)		
	Circular	Rectangular	Triangular
1	347	322	331
2	349	318	331
3	356	319	333
4	360	342	344
5	364	342	342
6	363	348	338
7	339	339	351
8	339	337	353
9	341	339	357
Mean	351	334	342
Variance	10	11	10
L_{im} = Total Mean = 342 $pixel$			
$S_{L_{im}}$ = Total Variance = 9 $pixel$			

and focused on. It should be noted that this method is not accurate and an uncertainty of roughly ±5 μm is associated with it. For each microchannel, the flow rate of the syringe pump varies from 100 $\mu l/\min$ to 500 $\mu l/\min$ in 5 steps and the velocity field is measured at the entrance and exit in each step.

4.9 Uncertainty Analysis

4.9.1 Bias Error Due to Detectability

For the problem of laminar channel flow, the local fluid velocity at an interrogation region is reduced by the following relationship:

$$u = \frac{\Delta x_{flow}}{\Delta t} \tag{4.20}$$

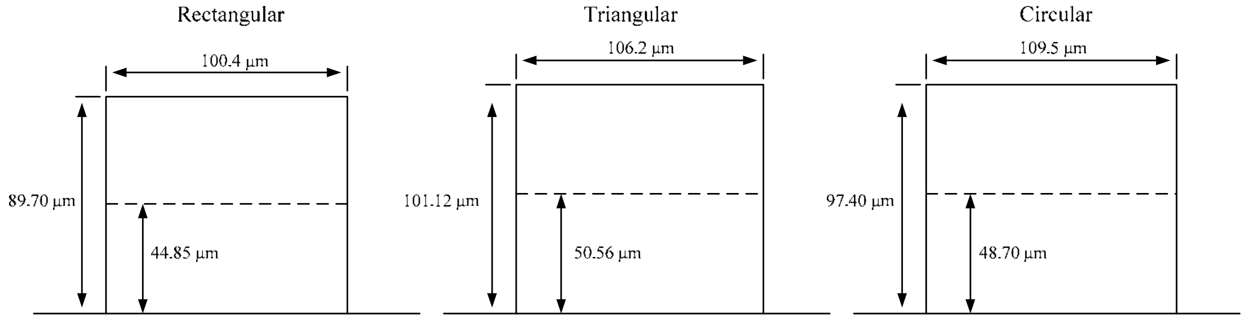

Figure 4.14: Microchannel cross-sectional profiles and location of measurement planes

where Δt is the time interval between the laser pulses and Δx_{flow} is the particle image displacement projected back into the flow in microns.

The bias uncertainty of the measured velocity due to detectability is related to the elementary bias uncertainties by the following equation:

$$\delta_{u,d}^2 = \eta_{\Delta x}^2 \delta_{\Delta x}^2 + \eta_{\Delta t}^2 \delta_{\Delta t}^2 \tag{4.21}$$

where η_ϕ is the sensitivity coefficient, defined as $\partial u/\partial \phi$; and δ_ϕ is the uncertainty in measurement of the quantity ϕ.

The uncertainty of the displacement measurement, as stated earlier in Eq. 4.18, is one tenth of the effective image diameter projected back into the measurement plane, i.e.:

$$\delta_{\Delta x} = \frac{d_e}{10\,M} = 235\,nm \tag{4.22}$$

The uncertainty in the time interval between the two laser pulses, Δt, according to the manufacturer is:

$$\delta_{\Delta t} = 1\,ns \tag{4.23}$$

The sensitivity coefficients are,

$$\eta_{\Delta x} = \frac{1}{\Delta t} \tag{4.24}$$

$$\eta_{\Delta t} = -\frac{\Delta x}{\Delta t^2} \tag{4.25}$$

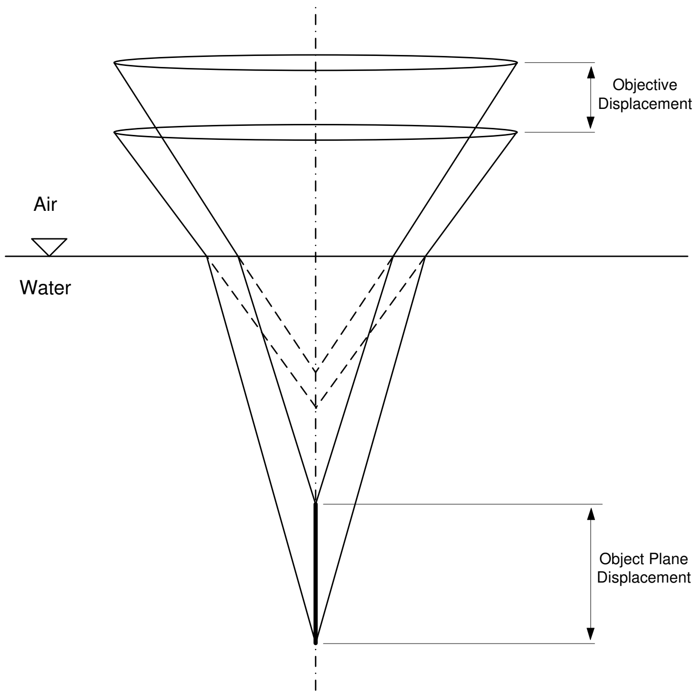

Figure 4.15: The relative displacements in the objective and measurement planes

4.9.2 Calibration Error

In order to convert the velocity results produced by the software in pixels per second to the velocity in microns per second, we have to multiply the displacements in pixels by the length in the flow domain corresponding to a unit pixel in the image, obtained by calibrating the system (see Sec. 4.7):

$$u = \frac{\Delta x_{im}}{\Delta t} \times \frac{L_{ch}}{L_{im}} \tag{4.26}$$

In this equation, Δx_{im} is the local displacement of particles in the image plane in pixels and Δt is the laser pulse separation. There is some level of error associated with calibration, i.e. L_{ch} and L_{im}. Based on the variance of data given in Tables 4.3 and 4.2 and a 90%

probability:

$$\begin{aligned}\delta_{L_{ch}} &= \pm t_{\nu,P}\, S_{L_{ch}} = 1.71 \times 3.78\,\mu m = 6.46\,\mu m \\ \delta_{L_{im}} &= \pm t_{\nu,P}\, S_{L_{im}} = 1.86 \times 9\,pixel \approx 17\,pixel \end{aligned} \tag{4.27}$$

The uncertainty of calibration can be determined by the following equation:

$$\delta_{u,c}^2 = \eta_{L_{ch}}^2 \delta_{L_{ch}}^2 + \eta_{L_{im}}^2 \delta_{L_{im}}^2 \tag{4.28}$$

where $\eta_{L_{ch}}$ and $\eta_{L_{im}}$ are given by:

$$\begin{aligned}\eta_{L_{im}} &= \frac{\Delta x_{im}}{\Delta t\, L_{im}} \\ \eta_{L_{ch}} &= -\frac{\Delta x_{im}\, L_{ch}}{\Delta t\, L_{im}^2}\end{aligned} \tag{4.29}$$

4.9.3 Precision Error

Suppose we are measuring the local velocity vector, $V(x, y)$, in the velocity field V, by ensemble averaging N image pairs, each represented by V_i, where $i = 1, 2, \ldots, N$. Statistical values obtained from such finite data sets should be regarded only as estimates of the true value of the velocity at (x, y). This finite-sized data set provides the following statistical data [45]: velocity mean value:

$$\overline{V}(x, y) = \frac{1}{N}\sum_{i=1}^{N} V_i(x, y) \tag{4.30}$$

and, sample standard deviation:

$$S_{V(x,y)} = \left(\frac{1}{N-1}\sum_{i=1}^{N}(V_i(x, y) - \overline{V}(x, y))^2\right)^{\frac{1}{2}} \tag{4.31}$$

$\big(V_i(x, y) - \overline{V}(x, y)\big)$ is called the deviation of $V_i(x, y)$. The degrees of freedom in a statistical estimate is equal to the number of measurements minus the number of predetermined statistical parameters used in estimating that value. As a result, the degrees of freedom in the standard deviation equation is $N - 1$, because $\overline{V}(x, y)$ has been previously determined. The velocity mean value provides a most probable estimate of the true mean value. The standard deviation represents the probable variations found in the data set.

The probability that any future measurements of velocity will fall within some stated interval is represented by a weight function called t-estimator. The precision uncertainty in the measurement of local velocity is:

$$\delta_{p,u} = \pm t_{\nu,P}\, S_V \tag{4.32}$$

For a normal distribution of variable $V(x, y)$, about a sample mean value, $\overline{V}(x, y)$, one can state that:

$$V_i(x, y) = \overline{V}(x, y) \pm t_{\nu,P}\, S_V \quad (P\%) \tag{4.33}$$

where the interval $\pm t_{\nu,P}\, S_V$ represents a precision interval, given at a probability of $P\%$, within which one should expect any measured velocity value to fall. The value of the t-estimator is a function of probability, P, and degree of freedom, ν. These values can be obtained from Table 4.4. Now, suppose that we measure the velocity field by ensemble averaging N image pairs. If this procedure is duplicated M times, different estimates of the local velocity mean value and velocity standard deviation at point (x, y) would be obtained each time (see Fig. 4.16). The amount of variation in the velocity means would depend on two values: The velocity standard deviation, S_V, and the number of image pairs, N. The discrepancy in mean values increases with standard deviation and deceases with $N^{1/2}$. The distribution of velocity mean values about the true mean is characterized by the standard deviation of the means, $S_{\overline{V}}$:

$$S_{\overline{V}} = \frac{S_V}{\sqrt{N}} \tag{4.34}$$

The standard deviation of the means reflects an estimate of how the local velocity mean values may be distributed about a true mean value. The range over which the possible values

Table 4.4: Values of t-estimator based on probability and degree of freedom

ν	t			
	50%	90%	95%	99%
1	1.000	6.314	12.760	63.657
2	0.816	2.920	4.303	9.925
3	0.765	2.353	3.182	5.841
4	0.741	2.132	2.770	4.604
5	0.727	2.015	2.571	4.032
6	0.718	1.943	2.447	3.707
7	0.711	1.895	2.365	3.499
8	0.706	1.860	2.306	3.355
9	0.703	1.833	2.262	3.250
10	0.700	1.812	2.228	3.169
11	0.697	1.795	2.201	3.106
12	0.695	1.782	2.179	3.055
13	0.694	1.771	2.160	3.012
14	0.692	1.761	2.145	2.977
15	0.691	1.753	2.131	2.947
16	0.690	1.746	2.120	2.921
17	0.689	1.740	2.110	2.898
18	0.688	1.734	2.101	2.878
19	0.688	1.729	2.093	2.861
20	0.687	1.725	2.086	2.845
21	0.686	1.721	2.080	2.831
30	0.683	1.697	2.042	2.750
40	0.681	1.684	2.021	2.704
50	0.680	1.679	2.010	2.679
60	0.679	1.671	2.000	2.660
∞	0.674	1.645	1.960	2.576

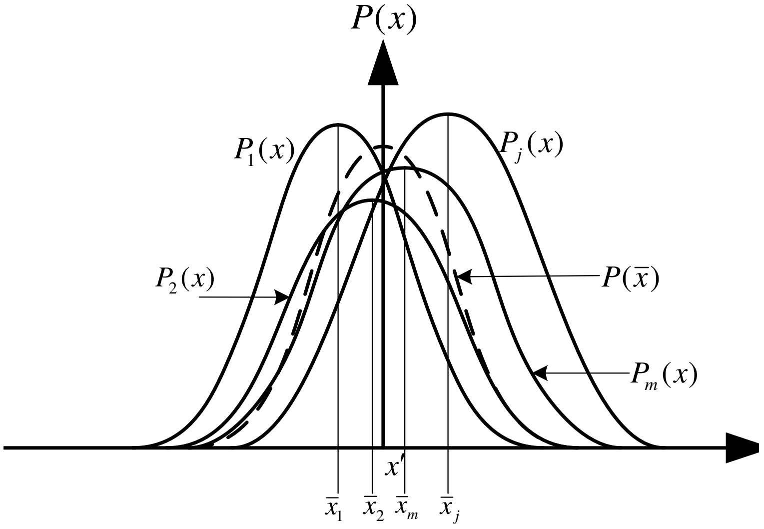

Figure 4.16: Distribution of sample means among a true mean value

of the true mean value might lie at some probability level, P, based on the information from one velocity measurement datum is given as:

$$\overline{V}(x,y) \pm t_{\nu,P}\, S_{\overline{V}} \tag{4.35}$$

The confidence interval, $\pm t_{\nu,P}\, S_{\overline{V}}$, represents the random uncertainty in the mean value due to the variations in the measured data sets. The estimate of the true mean value of velocity at point (x, y) is given as:

$$V(x,y) = \overline{V}(x,y) \pm t_{\nu,P}\, S_{\overline{V}} \quad (P\%) \tag{4.36}$$

The total uncertainty in the velocity measurement is:

$$\delta_u = \sqrt{\delta_{d,u}^2 + \delta_{c,u}^2 + \delta_{p,u}^2} \tag{4.37}$$

4.9.4 Entropy Generation Errors

Based on the velocity measurement errors, the errors in the measured entropy generation can also be determined [46]. The frictional entropy production in the fully developed region of the channel is calculated by the following equation:

$$\dot{S}_{gen} = \frac{\mu}{T}\left(\frac{\Delta u}{\Delta y}\right)^2 \tag{4.38}$$

Neglecting errors in reported fluid properties, the uncertainty of entropy production is:

$$\delta^2_{\dot{S}_{gen}} = \delta^2_{\Delta u} + \delta^2_{\Delta y} + \delta^2_T \tag{4.39}$$

where $\delta_{\Delta u}$, the uncertainty in $\Delta u = u_{i+1} - u_{i-1}$, is obtained from:

$$\delta_{\Delta u} = \sqrt{\left(\frac{\partial \Delta u}{\partial u_{i+1}}\delta u_{i+1}\right)^2 + \left(\frac{\partial \Delta u}{\partial u_{i-1}}\delta u_{i-1}\right)^2} \tag{4.40}$$

where $\partial\Delta u/\partial u_{i+1} = 1$, $\partial\Delta u/\partial u_{i-1} = -1$, and δu is determined from Eq. 4.37. $\delta_{\Delta y}$ is the uncertainty in $\Delta y = y_{i+1} - y_{i-1}$, and is obtained from:

$$\delta_{\Delta y} = \sqrt{\left(\frac{\partial \Delta y}{\partial y_{i+1}}\delta y_{i+1}\right)^2 + \left(\frac{\partial \Delta y}{\partial y_{i-1}}\delta y_{i-1}\right)^2} \tag{4.41}$$

where $y = y_{im} \times L_{ch}/L_{im}$, $\partial\Delta y/\partial y_{i+1} = 1$, $\partial\Delta y/\partial u_{i-1} = -1$, and δy is calculated from:

$$\delta^2_y = \delta^2_{y_{im}} + \eta^2_{L_{ch}}\delta^2_{L_{ch}} + \eta^2_{L_{im}}\delta^2_{L_{im}} \tag{4.42}$$

where $\eta_{L_{ch}}$ and $\eta_{L_{im}}$ are given by Eq. 4.29, $\delta_{L_{ch}}$ and $\delta_{L_{im}}$ by Eq. 4.27, and $\delta_{y_{im}}$ is roughly $1\,pixel$.

In Fig. 4.17 the velocity and entropy generation profile at a flow rate of $300\,\mu l/\min$ measured by the micro-PIV system has been compared against the analytical profiles (see Sec. 3.1) and the error bars calculated by the above method have been shown. The over prediction of velocity close to the wall has been observed in previous works (for example [13]) and is due to the near wall measurement effects. This over-prediction resulted in the deviation of measured entropy generation profile from the analytical profile near the walls.

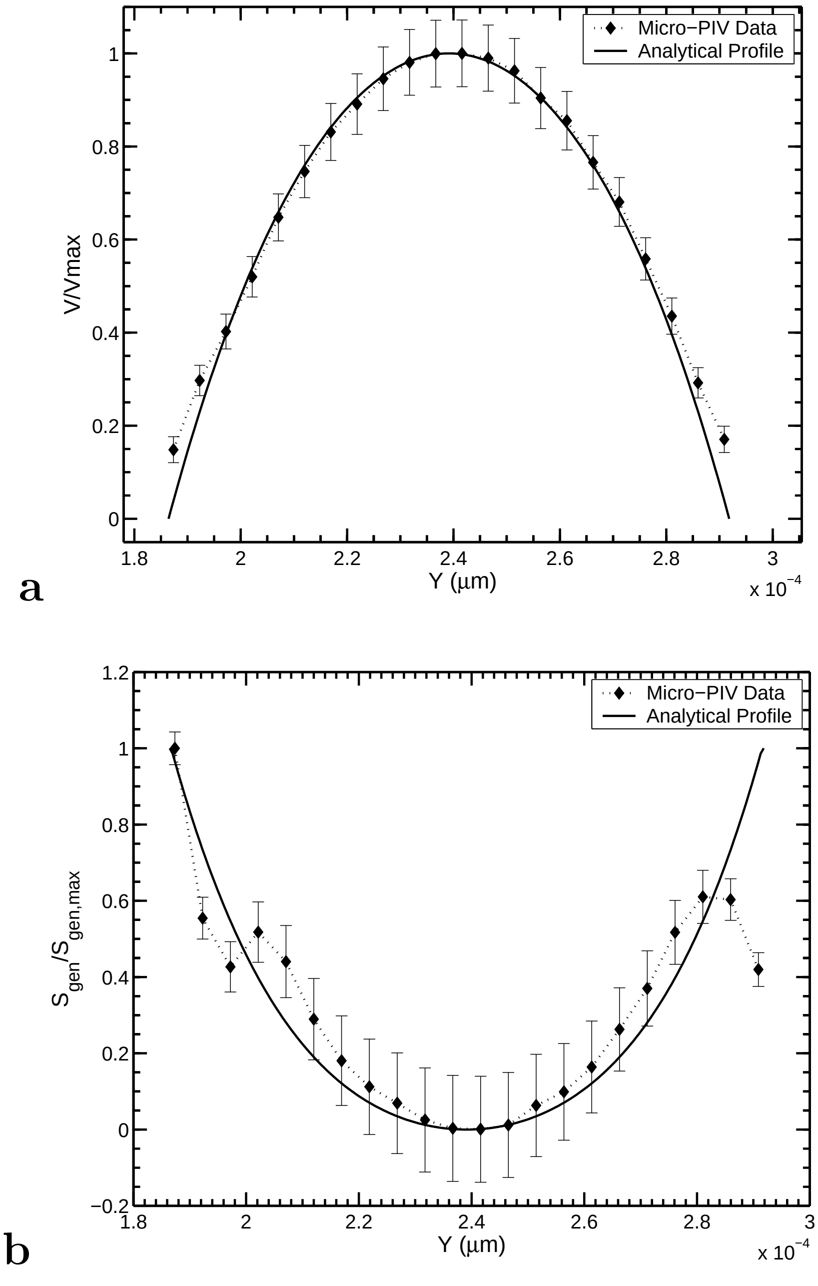

Figure 4.17: Comparison of the experimental and analytical velocity (a) and entropy generation (b) profiles at a fully developed section of the duct

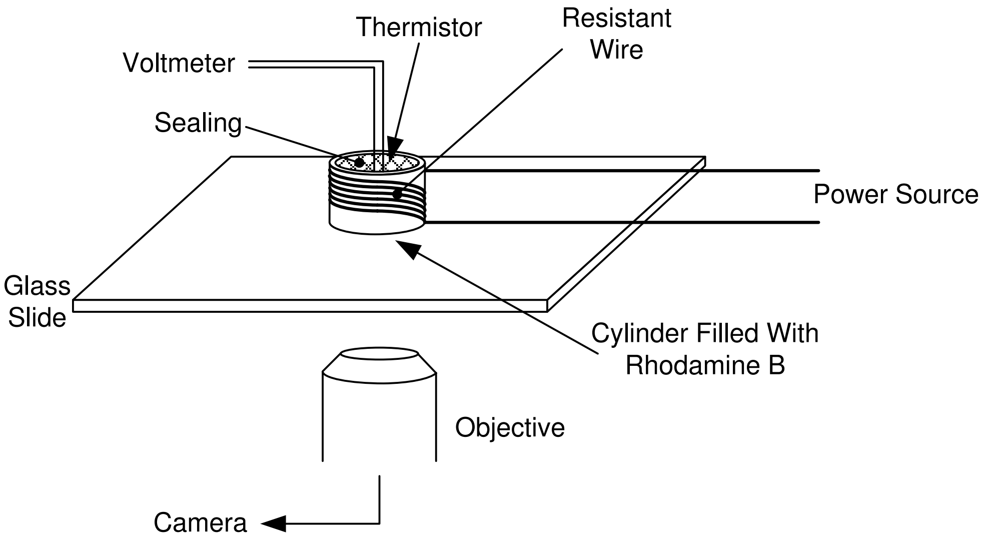

Figure 4.18: LIF calibration setup

4.10 LIF Calibration

Spatial variations of the temperature field are required to determine the thermal entropy generation rates. As stated in Chapter 1, the fluorescent intensity is a function of the intensity of the excitation light, I_e, concentration of the fluorescent dye, C, temperature dependant quantum efficiency[10], $\phi(T)$, and molecular absorptivity, α, through the following relationship:

$$I = I_e C \alpha \, \phi(T) \tag{4.43}$$

The first step in the temperature measurements procedure is the calibration, i.e. correlating the fluorescent intensity with temperature. A schematic of the calibration setup is shown in Fig. 4.18. Five centimeters of Nichrome resistance wire is spun around a 1 *cm* long piece of copper tube with a diameter of 0.5 *cm* and fixed with thermal epoxy. The tube is then glued to a standard microscope slide and filled with Rhodamine B solution

---

[10] Quantum efficiency decreases with temperature.

with a concentration of 1 mM. A thermistor, connected to a data-log, is inserted into the solution to record the variations of Rhodamine B temperature. The tube is covered on the top by sealing tape to reduce the rate of evaporation at high temperatures which changes the concentration of Rhodamine B. By controlling the voltage across the resistance wire, we can control the temperature of the solution inside the container.

The Nd:YAG laser is used as the illumination source. The laser light intensity is not distributed uniformly over the measurement area, thus the fluorescent reflection of Rhodamine B recorded by the camera is not homogeneous. To remove the effect of illumination non-uniformity on temperature measurement, the ratio of the fluorescent intensity images to a reference fluorescent intensity image, at room temperature for example, is correlated with temperature, instead of the absolute intensity images. The nonuniform distribution of illumination light is the same in all the images; therefore, it cancels out when dividing intensity images by a reference image. If the fluorescent intensity image at the reference temperature T_{ref} is I_{ref}, and at another arbitrary temperature T_1 is I_1, the ratio of I_1/I_{ref} is:

$$\frac{I(T_1)}{I(T_{ref})} = \frac{I_0 C\alpha\phi(T_1)}{I_0 C\alpha\phi(T_{ref})} = \frac{\phi(T_1)}{\phi(T_{ref})} \tag{4.44}$$

Equation 4.44 shows that the ratio I_1/I_{ref} is only a function of temperature and is not affected by illumination light uniformity. The concentration of Rhodamine B and the illumination power is kept constant for all images. A sample of an intensity image at room temperature with nonuniform illumination is shown in Fig. 4.19. The difference between the fluorescent reflection intensity of pixels is as high as 120%. Initially, ten pictures are taken 150 μm deep inside the solution at room temperature ($21.4°C$) and averaged to form a single intensity reference image. Then, the solution is heated up step by step, and ten images are captured at each temperature and averaged. The intensity images are divided by the reference image, which has the highest intensity, to remove the nonuniform illumination

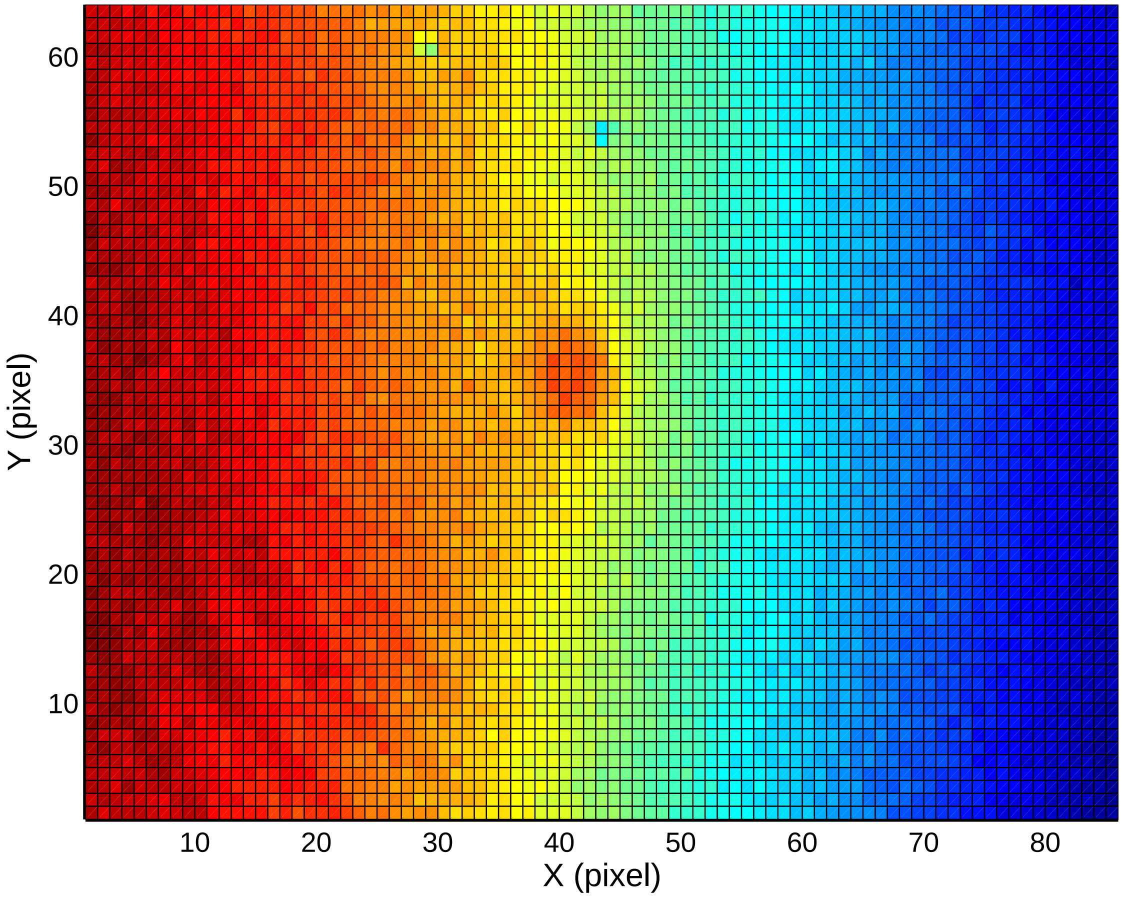

Figure 4.19: Fluorescent intensity field of a 1 mM Rhodamine B solution at room temperature. The illumination light is not uniformly distributed over the measurement field.

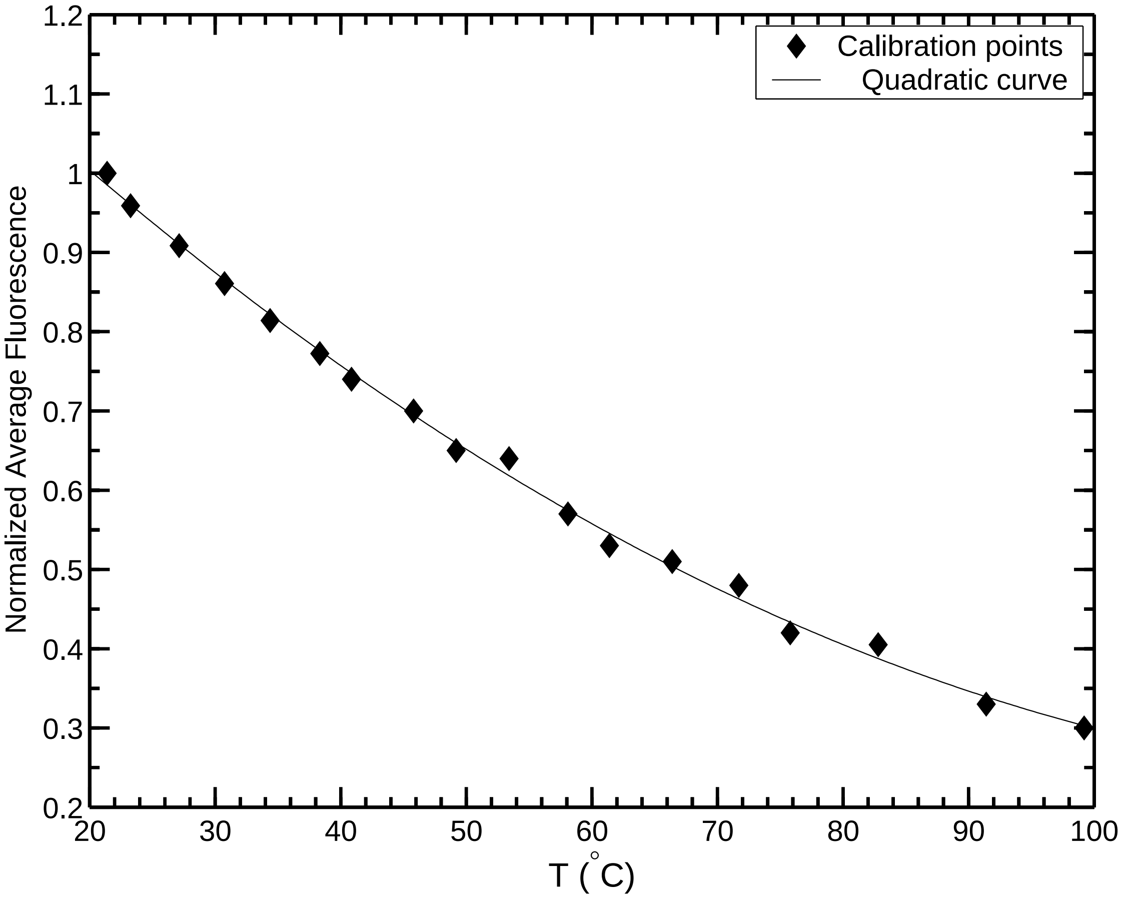

Figure 4.20: LIF calibration curve

effects. The unavoidable and rapid evaporation at temperatures higher than $60°C$ increases the calibration uncertainty. The calibration is done fast to reduce the uncertainties caused by evaporation. Figure 4.20 shows the measured normalized and averaged intensities and the corresponding temperatures, along with a quadratic curve fit.

4.11 Microchannel Fabrication

4.11.1 Soft-Lithography

The Soft-Lithography method is receiving an increasing amount of attention from the microfluidics field, especially PDMS[11] micro-molding method, due to low cost, low toxicity, transparency and ease of bonding of PDMS. Micro-molding is a simple and rapid way of fabricating microfluidics chips, as compared to etching methods. The first step in micro-molding is to construct a master to act as the mold. In this work the master has been fabricated with a Photo-Lithography method. This technique uses a photosensitive emulsion called resist, SU8-2000 in this work, that can transfer the patterns from the mask to the substrate. The patterns of the microchannels are drawn with AutoCAD and printed onto transparency films with a 20000 dpi resolution printer (CadArts Co.). In Fig. 4.21, a schematic of the mask is shown. The desired pattern is left blank with the other regions printed black. The three entrance and exit geometries, under study in this work, are also shown in Fig. 4.21. The first step is spin-coating the silicon substrate with a photoresist. The SU8-2000 resists are available in various viscosities for different thicknesses. The SU-8 film thickness, i.e. the microchannel height, is determined by the viscosity of the resist and spin speed. Higher viscosities and lower spin speeds mean a thicker resist film. Table 4.5 gives some examples of the relationship between the type of photoresist and the film thickness achieved at the spin speed of 1000 RPM. A 5 μm thick layer of SU8-2005 resist is coated on the substrate before coating it with the main layer. The spin speeds, accelerations, and times are given in the Table 4.6. This layer is called the adhesion layer and covers the roughness and probable curvatures on the substrate surface, and provides better adhesion of the main layer with the substrate. Spin-coating does not provide an even distribution of resist over the surface of the substrate and the layer is thicker at the center of the substrate and thinner near the edges.

---

[11] Polydimethylsiloxane

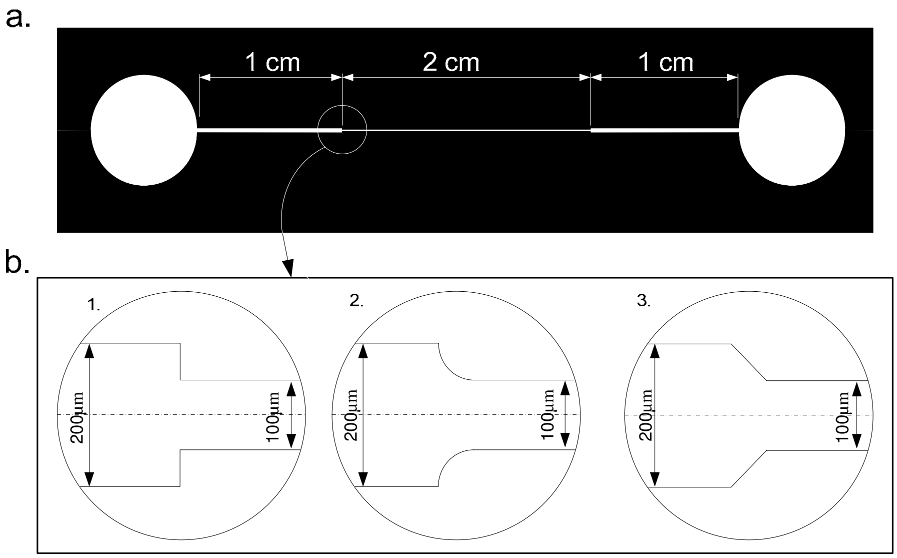

Figure 4.21: (a)Sample of the masks used in fabricating the microchannels. (b)Entrance and exit geometries of the microchannels

The next step is soft baking the adhesion layer on a hot plate to evolve the resist layer by evaporating the solvent out of it. The temperatures and durations of the adhesion layer soft bake are given in Table 4.7. The step-up heating and step-down cooling is to prevent damage caused by thermal stresses. The next process is exposure. SU-8 is a negative tone photoresist, i.e. the areas exposed to UV light are polymerized and their properties change so that they harden after being baked and maintain the transferred pattern. The entire area of the adhesion layer is exposed to 500 mJ of UV light. Thicker resist layers require higher exposure doses. Then, the substrate is post-exposure baked according to Table 4.8. After the adhesion layer is cooled to room temperature, the main layer of SU-8 resist is spin coated on the adhesion layer. The spin speeds and times vary depending on the desired height of the microchannels (see Table 4.9). The soft-bake is done afterwards with the parameters given in Table 4.10.

Later, the mask comes into contact with the baked SU-8 surface and exposed to UV

Table 4.5: Viscosity and corresponding thickness of SU-8 layer thicknesses at a spin speed of 1000 RPM [3]

SU-8 Type	Kinematic Viscosity(m^2/s)	Thickness (μm)
SU8-2002	4.3e-7	5
SU8-2005	29.3e-7	15
SU8-2010	105e-7	30
SU8-2025	252.5e-7	40
SU8-2050	1,225e-7	100
SU8-2100	5,150e-7	250

Table 4.6: Spinning steps for covering the substrate with the adhesion layer [4]

Step	Speed (RPM)	Time (s)	Acceleration (RPM/s)
1	500	15	100
2	3000	40	300

light. The mask is fixed to the substrate in a vacuum holder to ensure no gaps between the mask and the resist layer. The areas under the blank regions of the mask are polarized due to exposure with UV light, while the areas under black regions remain unchanged. The UV exposure energy is 800 mJ for a channel height of $100\,\mu m$. The fact that the incident UV light is not completely normal to the substrate surface as well as material and optical limitations cause the side walls of the channel to be slightly inclined rather than vertical. Then, the post-exposure bake (hard-bake) is done with temperatures and durations given in Table 4.11.

Table 4.7: Soft-baking and step down cooling of the adhesion layer [4]

Temperature(C)	65	95	65	50	T_{room}
Time (min)	1	2	1/2	0	10

Table 4.8: Hard-baking and step down cooling of adhesion layer [4]

Temperature($^{\circ}C$)	65	95	65	50	T_{room}
Time (min)	1	3	1/2	1/2	15

Table 4.9: Spinning steps for covering the substrate with the main resist layer for the three channel heights

Height(μm)	Step	Speed (RPM)	Time (s)	Acceleration (RPM/s)
100	1	500	15	100
	2	1000	32	300

Table 4.10: Soft-bake and cooling steps of the main SU-8 layer

Height(μm)	Temperature ($^{\circ}C$)				
	65	95	65	50	T_{room}
100	5	12	1	1	20

Table 4.11: Post exposure baking and cooling steps

Height(μm)	Temperature ($^{\circ}C$)				
	65	95	65	50	T_{room}
100	5	9	2	2	20

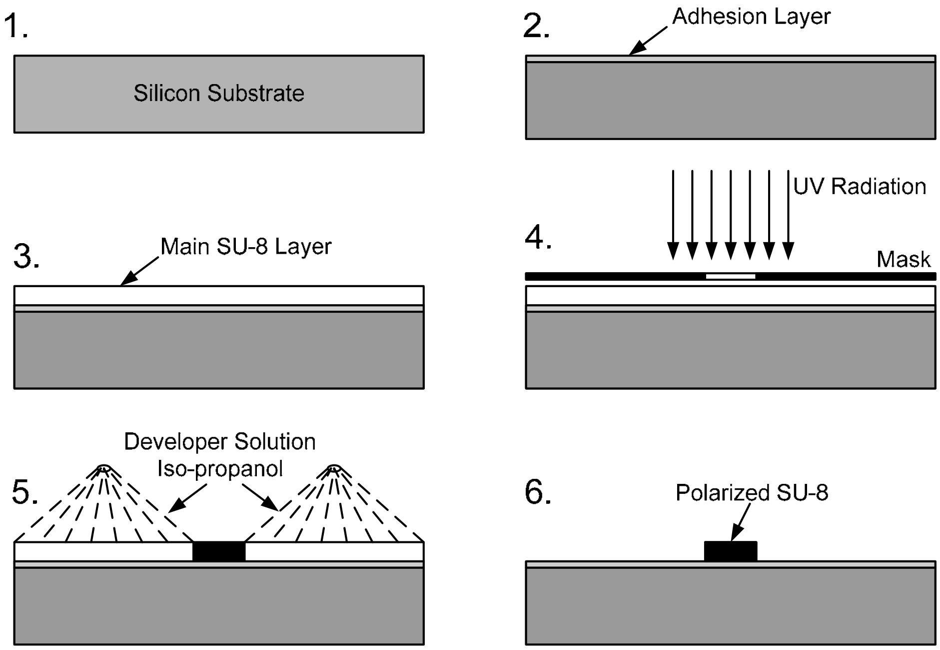

Figure 4.22: Schematic of the Photo-Lithography process used to fabricate masters

Afterwards the substrate is immersed in the developer solution for 5 to 10 minutes in which non-exposed areas dissolve. The final step is rinsing with Isopropanol to remove the unwanted regions of photoresist from the substrate. The whole process is schematically shown in Fig. 4.22. After making the master, the microchannels are made out of PDMS with a Soft-Lithography method [47]. First, the PDMS prepolymer (SYLGARD-184 Silicon Elastomer, Dow Corning) is mixed with the curing agent in a 1:10 weight ratio. The mixture is then poured over the master inside a petri dish and degassed in a vacuum oven at -27 bars for one hour to eliminate the gas baubles and insure complete mixing between the two parts. The mixture is cured at $80°C$ for 1.5 hours. The solidified PDMS is then peeled off from the master, unwanted parts are removed and two holes are made in the plenums with a punch for the fluid to come in and go out of the chip. The structured surface of the PDMS

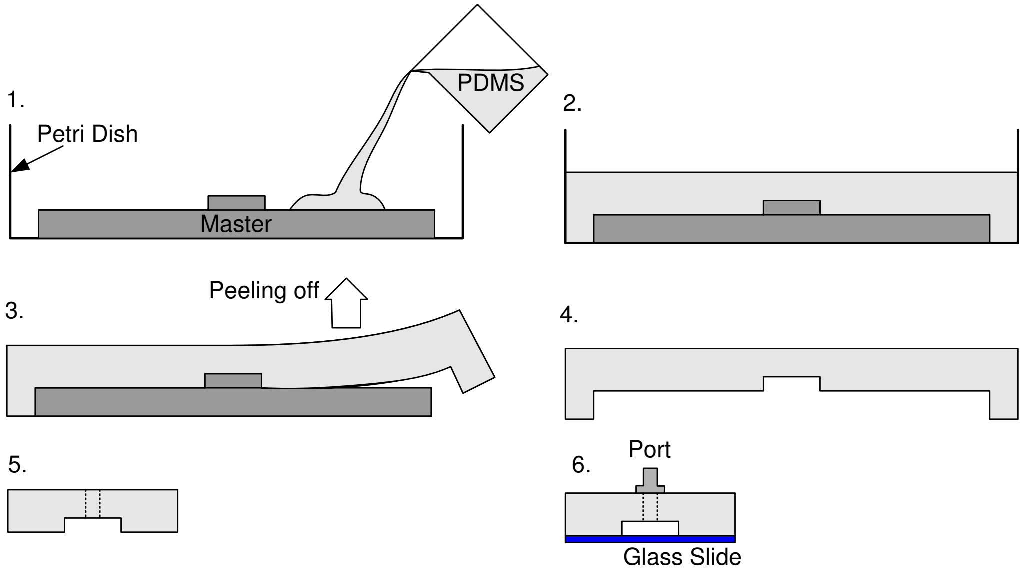

Figure 4.23: Schematic of the Soft-Lithography process

and a piece of glass microscope slides (750 μm thick) are then plasma treated for one minute at 18 W and brought into contact. The resulting bond is theoretically able to withstand pressures up to 5 bars. The inlet and outlet ports (Upchurch Scientific) are attached to the chip using PDMS at a 1:5 weight ratio. The steps of the Soft-Lithography process are shown in Fig. 4.23.

4.11.2 Anisotropic Dry Etching

Rhodamine B, which is used for the measurement of temperature, can be absorbed into the walls of PDMS channels if left untreated. The absorbed Rhodamine B emits some level of fluorescent light which causes false measurements. For this reason, silicon microchannels are fabricated using the Anisotropic Dry Etching method, specifically for the measurement of temperature.

The major problem of ordinary etching techniques is that making vertical trenches is not

Table 4.12: Spinning steps in the photolithography process

Speed (RPM)	Time (sec)
500	5
2500	45

possible. The top sections of the trench are exposed to the etching ions for a longer time; therefore, the structures are wider on the top. Anisotropic Dry Etching or Deep Reactive Ion Etching allows deep, high aspect ratio structures to be etched in silicon. The two main methods to perform this kind of etching are:

- Etching assisted by cryogenic cooling
- Alternate etching and chemical vapor deposition [12]

The second approach is used in this work, in which chemical vapor deposition is used to protect the sidewalls. The patterns are first defined by coating the silicon wafer with a thin layer of photoresist which is patterned by the photo-lithographically process prior to etching. The Shiply-1827 photoresist is used in this work. The resist is spun on the wafer in a two step process, presented in Table. 4.12. According to the resist manufacturer information, the thickness of the resist is between $3.4\,\mu m$ and $4.1\,\mu m$. The resist is then pre-baked at $117°C$. The masks are brought into contact with the resist layer in an EVG mask aligner and exposed to UV light for $20\,s$ with an energy of $20\,mW/cm^2$. As stated in the previous section, the exposed areas of the resist are polarized and hardened. The non-exposed areas are washed away after developing with MF-319 developer solution for $75\,s$. After that, it is rinsed with water and blow dried. The last step is post-baking at $117\,°C$for 10 minutes. The etching is done with an ALCATEL-601E deep reacting ion etching system. The process consists of two steps, etching and deposition. In the etching step which lasts for 7 s, the

---

[12] The method was invented by Robert Bosch, thus it is also called the Bosch process.

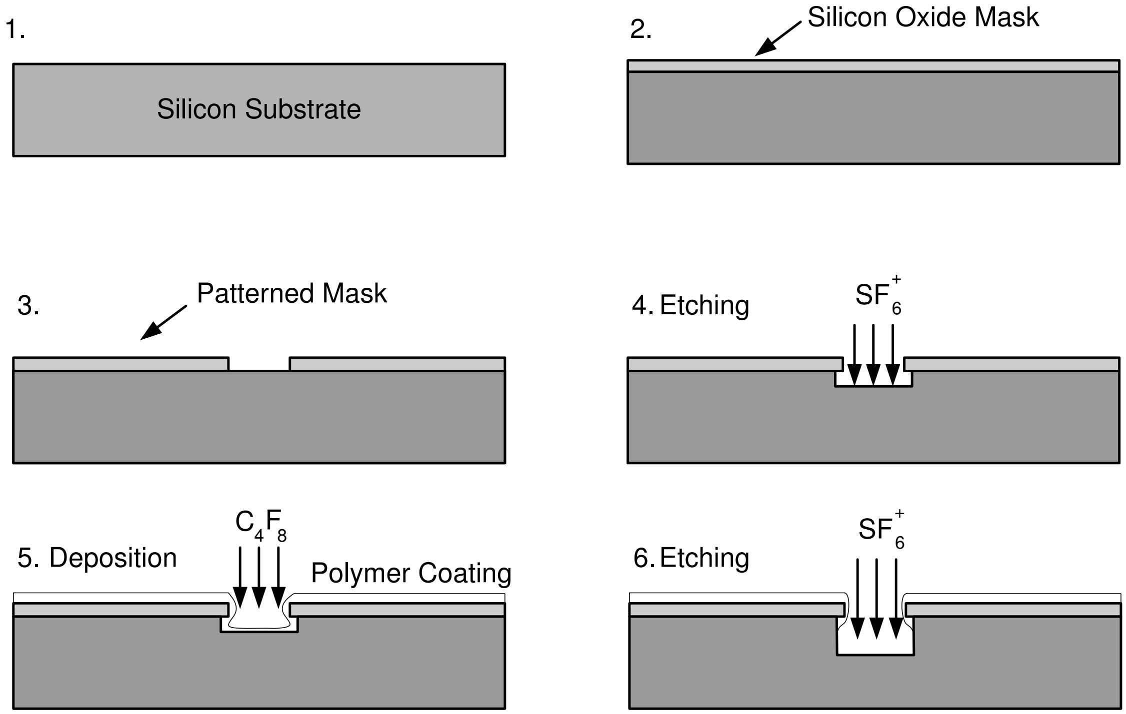

Figure 4.24: Schematic of the Anisotropic Dry Etching (Bosch) process

substrate is etched by a 300 *sccm* [13] flow of SF_6 gas ions. In the deposition step, a 10 *nm* layer of Fluorocarbon polymer is deposited on the trench walls by exposing the substrate to a 150 *sccm* flow of C_4F_8 for 3 seconds. In each etching step, the polymer film at the bottom of the trench and the silicon substrate are etched by the direct bombardment of ions, while the polymer film on the sidewalls protect it from being etched by the ions bouncing back from the bottom. The etch front advances into the substrate at a rate of $7\,\mu m/min$ and the whole process takes about 15 *min*. A schematic of the Bosch process is shown in Fig 4.24. The next step of the fabrication process is dicing the silicon wafers, with two devices on each, to get $3'' \times 1''$ chips. Before dicing, the wafer is coated with a layer of photoresist to protect the channel from being blocked with the fillings. The dicing is done in a KTS-780

---

[13] standard cubic centimeters per minute

machine with a diamond coated Nickel blade of $2''$ diameter and $35\,\mu m$ thickness. The blade rotates at $20,000\,RPM$ and advances at a rate of $0.5\,\mu m/s$. Through holes are drilled in the plenums for the fluid to enter and exit the devices with $1\,mm$ diameter diamond coated drills (UKAM Industrial) at 4700 RPM.

The next step is covering the structured silicon slides with glass. SU-8 negative-tone photoresist is used as an adhesive (for more details, see [48]). The structured silicon slides are washed with Acetone and Isopropanol alcohol to remove the protective resist layer. After that, $1\,mm$ thick glass wafers and etched silicon slides are cleaned in an ultrasound cleaner for 15 minutes and blow dried with Nitrogen to clean them of particles. The glass wafers and silicon slides are dehydrated by baking them on a hot-plate at $200°C$ for one hour. Then, SU-8 2015 photoresist was spin coated on glass wafers in a two step process for a uniform thickness of the SU-8: at 500 RPM for 10 seconds with an acceleration of $100\,RPM/s$ and at 4000 RPM for 42 seconds with an acceleration of $300\,RPM/s$. The resultant thickness of the adhesive layer is $13\,\mu m$. One silicon slide is placed in the middle of the wafer[14] and placed in an oven for 30 minutes at $150°C$ without applying any external forces on it. The resultant bond is strong enough to tolerate the pressure inside the channel and no leakage was observed. The last step is attaching the inlet and outlet ports on the microfluidic chips. The heat-curable adhesive provided by the manufacturer of the ports (Upchurch Scientific) was used. The adhesive was clamped between the substrate and the port, and heated in an oven at $150°C$ for 20 minutes. It must be noted that SU-8 is completely transparent for wavelengths above $400\,nm$. The absorbance versus wavelength of SU-8 with 4 different thicknesses is sketched in Fig. 4.25.

---

[14] The SU-8 layer is about 200 % thicker at the edges of the wafer which prevents the silicon from coming into contact with adhesive layer if placed near the edge.

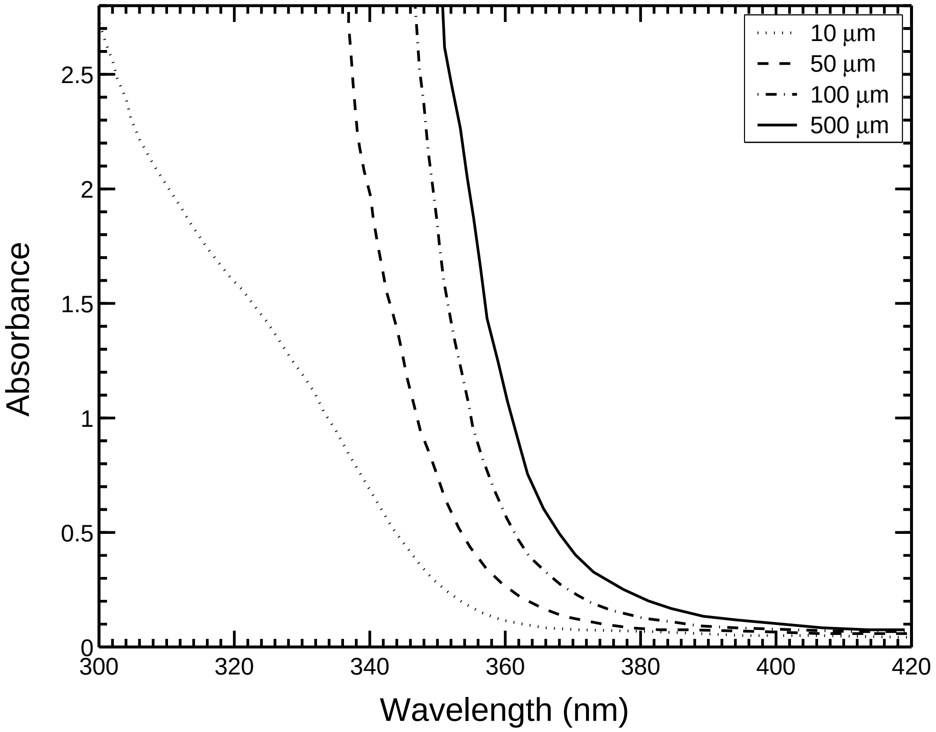

Figure 4.25: Absorbance versus wavelength of SU-8 photoresist [21]

Chapter 5

Results and Discussion

Entropy production in the entrance and exit regions of microchannels is examined using the experimental methods described in Chapter 4, combined with the analytical model presented in Chapter 3. A coupled method, using micro-LIF to measure heat transfer and micro-PIV to measure viscous dissipation can potentially provide an effective mechanism for design optimization of micro-scale devices.

5.1 Approach

As stated in the Chapter 1, entropy generation has two components; a frictional component caused by viscous dissipation within the fluid flow, and a heat transfer component caused by the convection process in the flow between the high temperature side walls and the low temperature fluid stream. First, the results of velocity measurements with micro-PIV and the frictional component of the entropy generation will be presented. Afterwards, the results of temperature measurements done with micro-LIF will be used to determine the thermal term in the entropy generation equation. Summation of these two terms results in the total entropy generation. The flowchart in Fig. 5.1 shows the steps required to obtain the total

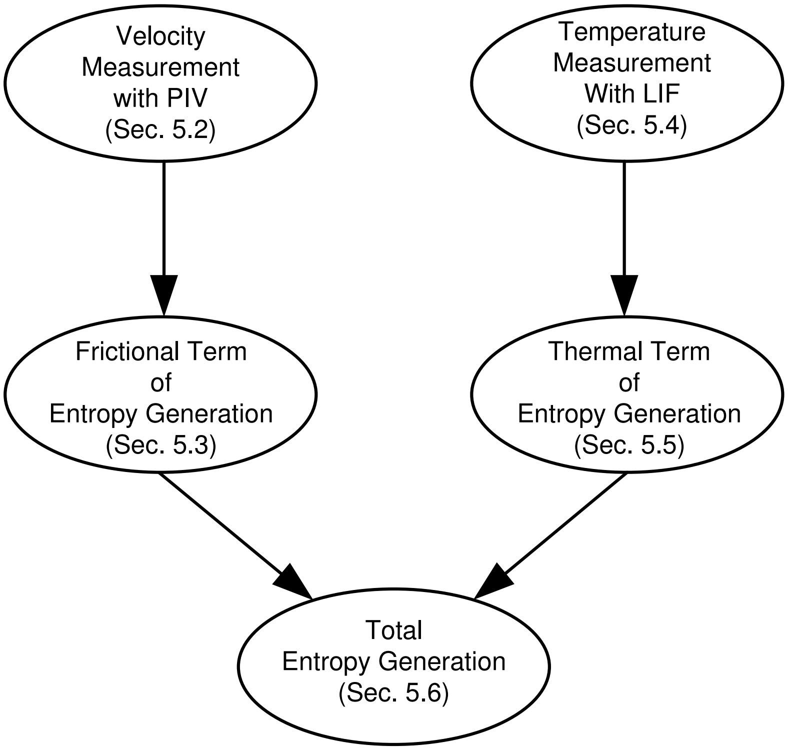

Figure 5.1: Steps required to obtain the total entropy generation

entropy generation. The test parameters, which were explained in detail in Chapter 4, are summarized as follows:

- Microchannels: Three PDMS and silicon microchannels, each with a different entrance and exit geometry, namely triangular, rounded and rectangular (see Fig. 4.21).
- Flow regime: The Reynolds number varies from 16.6 to 82.9 and the flow regime is laminar.
- Seeding: 500 nm red fluorescent polystyrene particles from Duke Scientific with a specific gravity of 1.05.
- Illumination: Nd:YAG laser pulses with a duration of 5 ns, an energy of 30 mJ, and

a wave length of 532 nm.

- Camera: 14-10 PIVCAM from TSI Inc, a CCD size of 1376 × 1040 $pixels$, a pixel size of 6.45 μm, and frame rate of 10 fps.
- Magnification: A Nikon Plan Fluor 10× objective with a Numerical Aperture of 0.3 on the microscope and a 2× projection lens in front of the camera.
- Grid: 32 × 32 interrogation regions with 50% overlap generated with a Nyquist grid generator, resulting in a resolution of roughly 5μm.
- Processing: Ensemble Correlation processing method based on Fast Fourier Transform correlation map generator. The Laser Pulse Delay and Pulse Separation are given in Table 4.1.

The deionized water flow rate ranges from 100 $\mu l/min$ to 500 $\mu l/min$ and the measurements plane is located at the middle of the channel's height (see Fig. 5.2 a). The thickness of the measurement plane, fixed by the specifications of the objective, is about 22 μm. The measurements are averaged over this volume and applied to the mid plane of the channel. Using INSIGHT 3G software from TSI Inc. and Tecplot a sample of a velocity vector field, in the exit section of the channel at a flow rate of 100 $\mu l/min$ is shown in Fig. 5.2 b. Velocity vectors are obtained within 5 μm from the wall.

5.2 Velocity Measurement

In Table 5.1, the maximum velocities at the cross-sections shown in Fig. 5.3 and their location along the width of the channel are given. The maximum velocities of measurements with the same flow rate are not identical. The reason is the slightly different cross-sectional areas that is unavoidable in the Soft-Lithography fabrication method (see Sec. 4.11.1). The

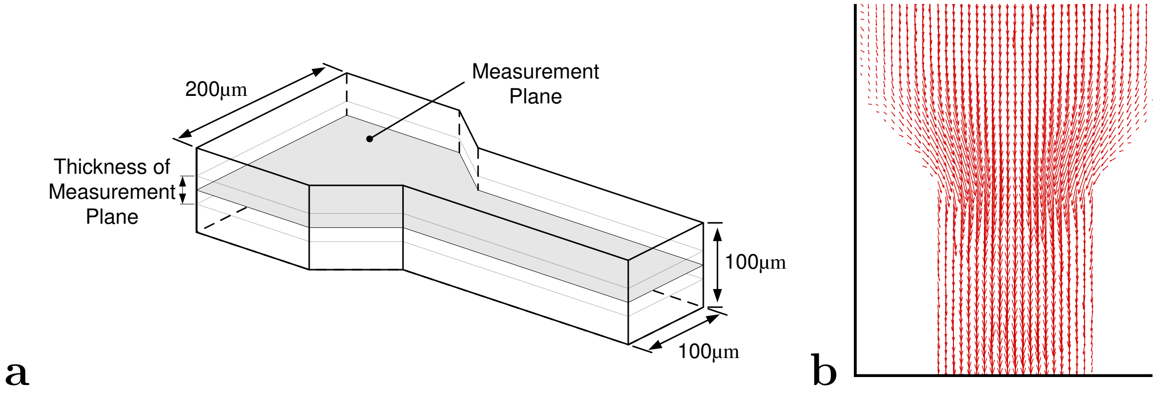

Figure 5.2: (a) A schematic of the position of the measurement plane. (b) A sample of the velocity field measurements

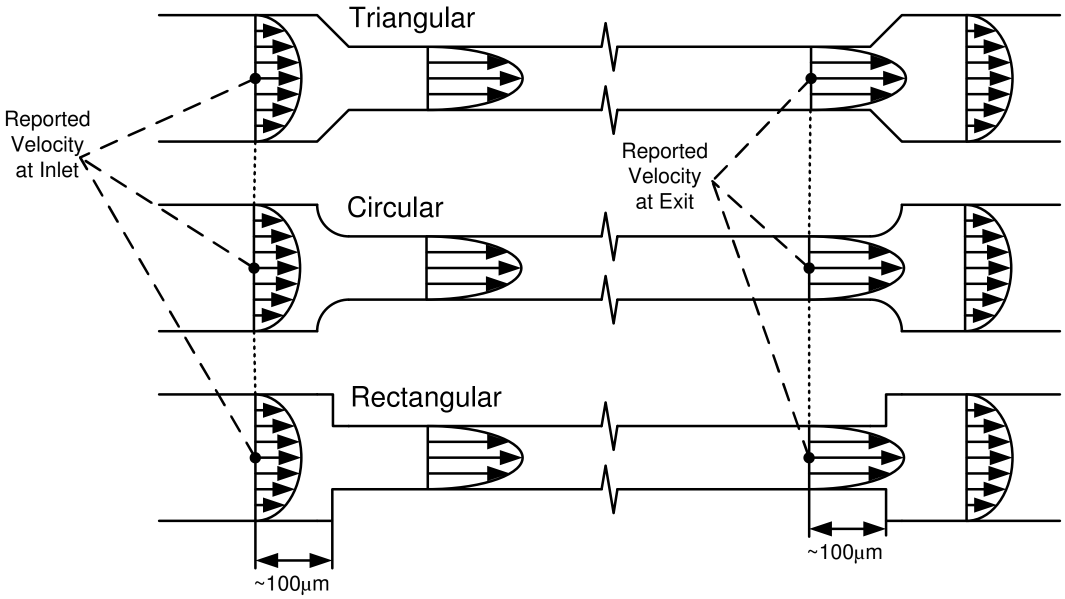

Figure 5.3: Schematic of the microchannels under study in this work and locations where the maximum velocities are reported

Table 5.1: The maximum velocities at the inlet location of the exit and entrance sections (see Fig. 5.3) in $\mu l/min$ and non-dimensionalized with the maximum velocity at $100\,\mu l/min$, along with the location along the width of the channel normalized with channel width

		Exit			Entrance		
Channel Geometry	Q ($\mu l/min$)	V_{max} Non-Dim.	V_{max} ($\mu m/s$)	y/W	V_{max} Non-Dim.	V_{max} ($\mu m/s$)	y/W
Rectangular	100	1.00	0.32	0.47	1.00	0.16	0.49
	200	1.98	0.64	0.53	1.99	3.14	0.45
	300	2.97	0.95	0.53	2.94	0.46	0.56
	400	3.94	1.26	0.47	3.89	0.61	0.49
	500	5.07	1.63	0.50	4.79	0.76	0.59
Triangular	100	1.00	0.30	0.52	1.00	0.15	0.55
	200	1.99	0.60	0.50	2.01	0.30	0.53
	300	2.99	0.90	0.50	2.89	0.44	0.50
	400	3.90	1.17	0.50	3.91	0.59	0.50
	500	4.84	1.46	0.45	4.73	0.71	0.59
Circular	100	1.00	0.27	0.57	1.00	0.15	0.58
	200	2.02	0.55	0.52	1.90	0.28	0.54
	300	3.00	0.81	0.45	2.85	0.42	0.50
	400	4.00	1.08	0.52	3.86	0.57	0.53
	500	5.02	1.36	0.52	4.63	0.68	0.41

measured velocity profiles in the flow direction (V) and normal to it (U) in the developing region and in the fully developed region of the microchannel are sketched and compared to the fully developed analytical profile in Fig. 5.4[1]. The streamwise velocity profile in the entrance region is flat at the core of the channel due to the inviscid core flow. There is an asymmetry in the profile because of the irregularity in the microchannel cross-sectional geometry. The normal velocity component in the entrance region is negative (to the left) in the right half of the channel and positive (to the right) in the left side. In the fully developed region, The measured profile is in excellent agreement with the analytical profile except very close to the walls. As expected, the vertical velocities are nearly zero. The insignificant negative values of vertical velocity are because of the small tilt of the microchannel.

Figure 5.6 illustrates the velocity vectors at the exit of the microchannels at the three flow rates of 100, 300 and 500 $\mu l/min$, for the rectangular, triangular, and circular geometries. The exact location and size of the regions under study in Fig. 5.6 is displayed in Fig. 5.5. It is shown that there is a region of separated flow at the exit of the channels, size and intensity of which depends on the geometry and flow rate. It is readily seen that the separation is more significant in rectangular channels. The strength of the circulation is almost similar in circular and triangular geometries, slightly bigger in the circular exit. As expected, the separated region grows with flow rate.

Similar measurements have been done at the entrance of the channel. The resulting velocity fields are shown in Fig 5.8. The areas under study in this figure, are shown in Fig. 5.7. No separation and vena contracta is observed in the velocity field of the rectangular entrance. The reasons are that, first, sharp corners can not be created with Soft-Lithography and second, the Reynolds number is too low for the separation to occur.

---

[1] Fully developed profile is the same in all the three microchannels; but, the developing profile in slightly different. The profile sketched in Fig. 5.4 belongs to the channel with triangular entrance and exit.

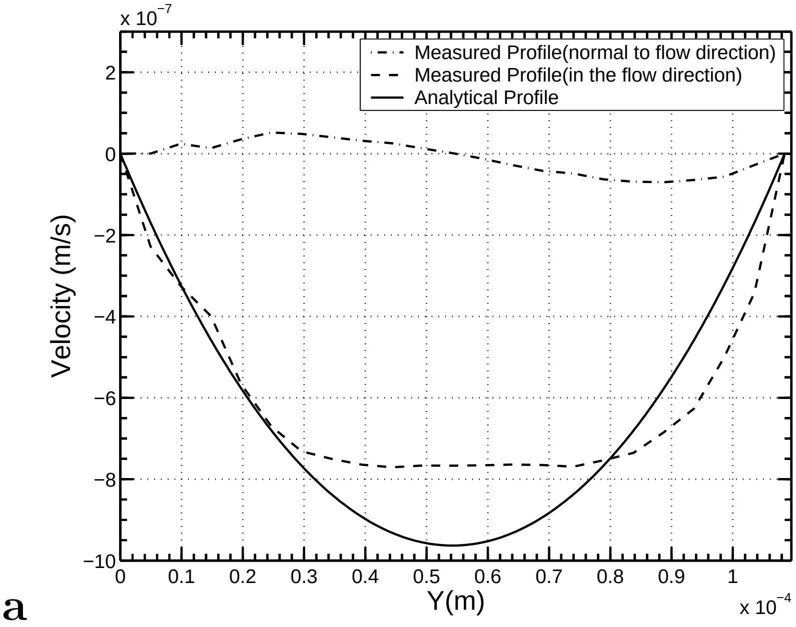

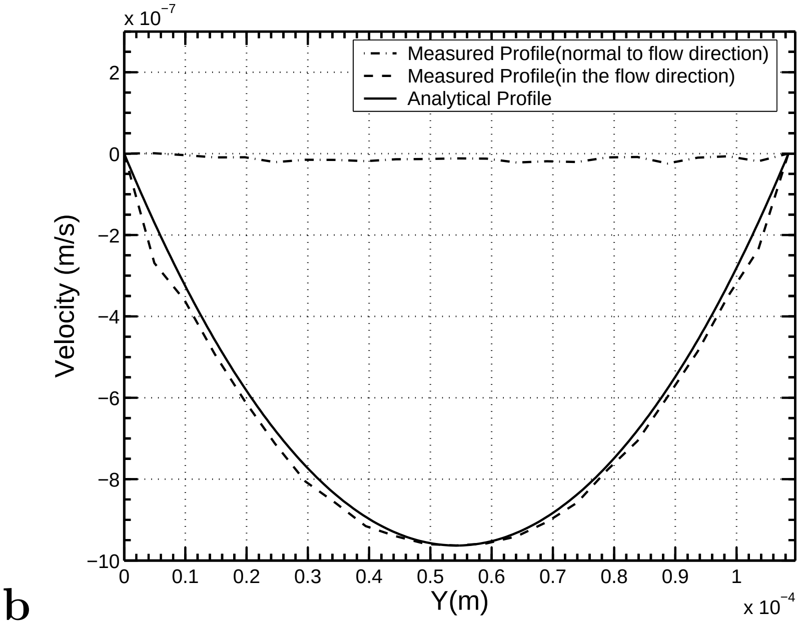

Figure 5.4: Streamwise and normal velocity profiles in the developing region (a) and fully developed region (b) of the channel compared to analytical fully developed velocity profile

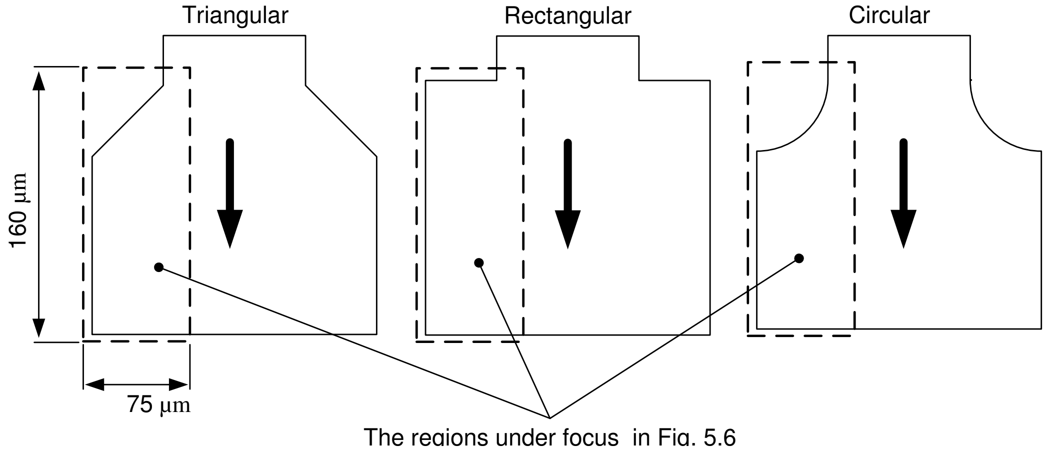

Figure 5.5: The regions at the exit of the microchannels whose velocity field is shown in Fig. 5.6

5.3 Frictional Entropy Generation

By postprocessing the velocity measurement data, the frictional entropy generation rates at the exit of the microchannels (see Fig. 5.9) are calculated and plotted in Figures 5.10 to 5.12. The highest rates of entropy generation are occurring in the region with highest shear stresses, i.e. close to the walls of the 100 μm wide channel and in the high velocity gradient regions of the jet coming out of it. Higher flow rates magnify the velocity gradients, hence increasing the entropy generation rates. The amount of entropy produced in the separated region is small, due to small velocities and velocity gradients. In other words, the entropy generated due to frictional effects are more significant than the entropy produced due to sudden flow area change and pressure drop. One can conclude from these figures that the entropy produced in triangular and circular exit shapes are larger than that produced in rectangular exit at similar flow rates.

The entropy generation profiles in the entrance and fully developed regions are plotted in Fig. 5.13. As stated in Sec. 4.9.4, the errors in the measurement of velocity near the sidewall cause the slope of the entropy generation profile to reverse close to the walls; therefore, In

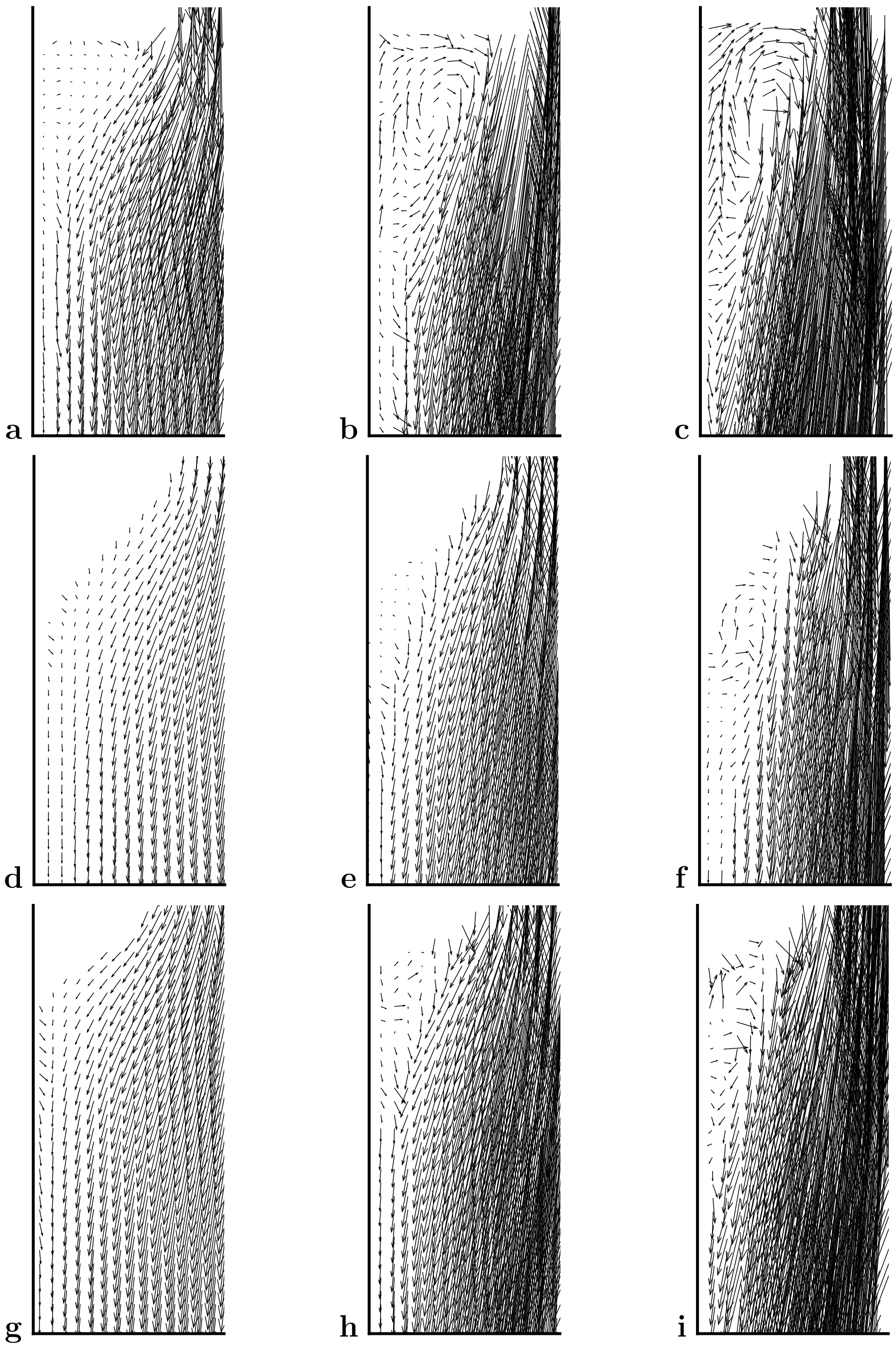

Figure 5.6: (a-c)Velocity field at the rectangular exit with flow rates of 100, 300, and 500 $\mu l/min$
(d-f)Velocity field at the triangular exit with flow rates of 100, 300, and 500 $\mu l/min$
(g-i)Velocity field at the circular exit with flow rates of 100, 300, and 500 $\mu l/min$

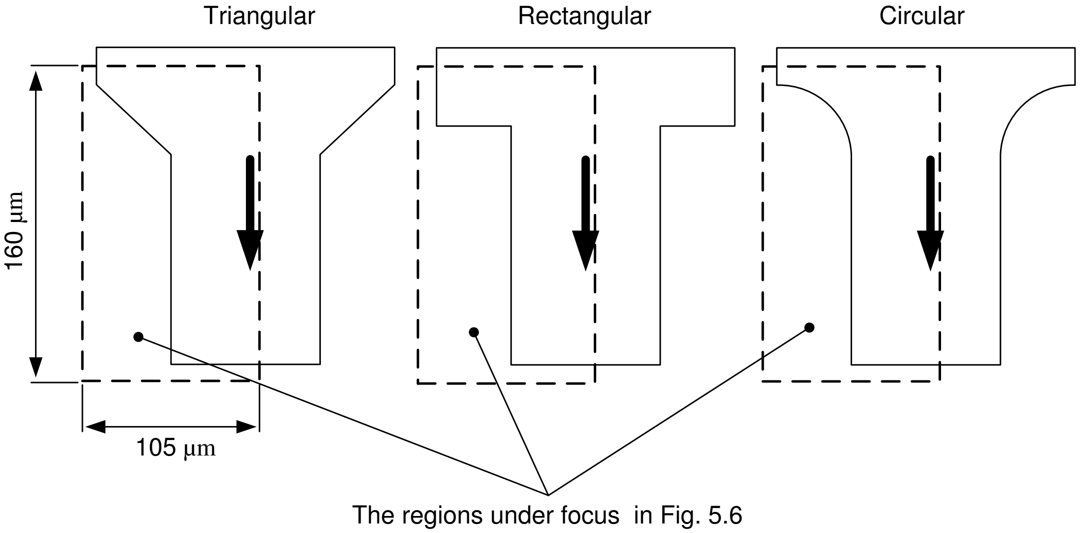

Figure 5.7: The regions at the entrance of the microchannels whose velocity field is shown in Fig. 5.8

Fig. 5.13, the data close to the walls are not considered. In the entrance region, entropy generation in the core of the flow is zero because of the zero velocity gradient in that area. Entropy generation profile is locally zero at the center of the channel, in the fully developed region, due to local zero velocity gradient there. The analytical entropy generation profile is in complete agreement with the measured profile.

The frictional entropy generation at the exit of the microchannel was determined analytically in Chapter 2. The results of the model for the flow rates of 100-500 $\mu l/min$ have been plotted in Fig. 5.14 a. Figure 5.14 b illustrates the results of the experimental measurement of entropy generation at the midplane of the microchannels' exit sections. The trends of variation in the amount of entropy production with flow rate and geometry changes are similar. However, the values are not comparable, since the model yields the entropy produced in the whole volume of the exit section, while the measurement only includes a two-dimensional plane at that section. The magnitudes of entropy generation in the exit of the microchannel, as predicted by the model and measured in the experiment are presented in Table 5.2.

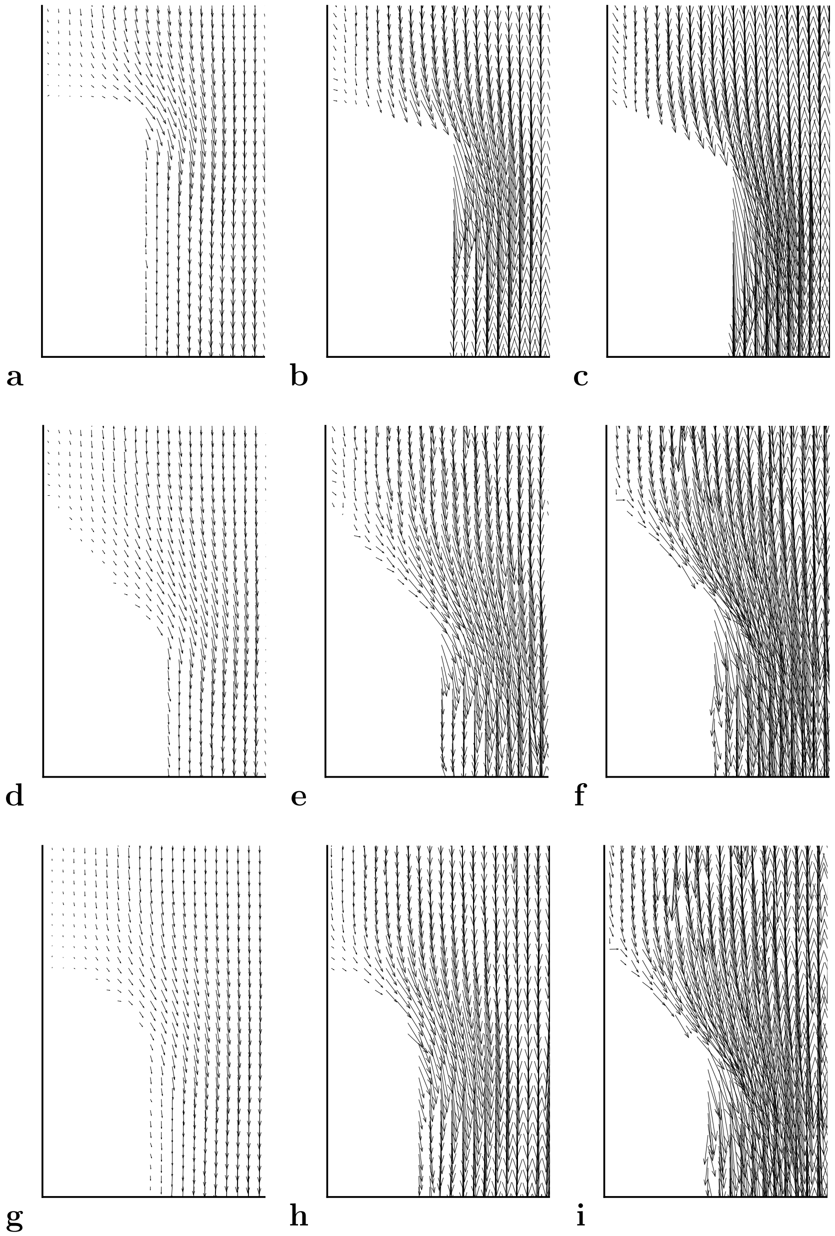

Figure 5.8: (a-c)Velocity field at the rectangular entrance with flow rates of 100, 300, and 500 $\mu l/min$. (d-f)Velocity field at the triangular entrance with flow rates of 100, 300, and 500 $\mu l/min$. (g-i)Velocity field at the circular entrance with flow rates of 100, 300, and 500 $\mu l/min$

Table 5.2: Results of the model and measurements for entropy generation in the exit of the microchannel

Channel Geometry	Q $(\mu l/min)$	$\dot{S}_{gen,model}$ (J/K)	$\dot{S}_{gen,experiment}$ (J/K)
Rectangular	100	3.1e-005	6.2e-011
	200	2.5e-004	2.8e-010
	300	8.5e-004	6.9e-010
	400	2.0e-003	1.2e-009
	500	3.9e-003	2.0e-009
Triangular	100	1.5e-004	1.0e-010
	200	1.2e-003	4.6e-010
	300	4.1e-003	1.1e-009
	400	9.7e-003	2.0e-009
	500	1.9e-002	3.7e-009
Circular	100	5.5e-005	8.0e-011
	200	3.5e-004	3.5e-010
	300	1.1e-003	8.1e-010
	400	2.5e-003	1.6e-009
	500	4.7e-003	2.5e-009

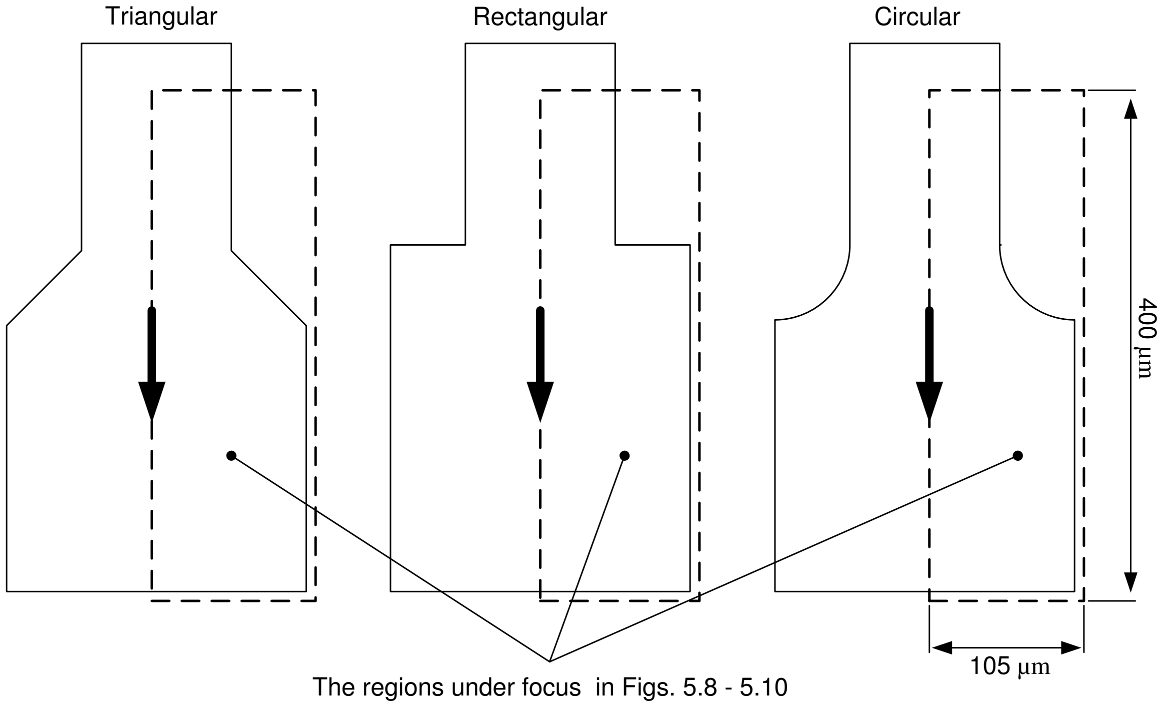

Figure 5.9: The location and size of the regions at the exit of the microchannels whose entropy generation constant contours are sketched in Figs. 5.10 to 5.12

Entropy generation has been calculated at the entrance of the channels and its contours are plotted in Figs. 5.16 to 5.18. The measurements have been done in the regions shown in Fig. 5.15. Shortly after the rectangular entrance, a small region with locally low entropy generation rate is observed near the wall which can be attributed to a separated flow region, too narrow to be observed with current resolution, at the vicinity of the wall which reduces the velocity gradient, thus the frictional entropy production.

The results of the model and the measurements for frictional entropy generation at the microchannel entrance are plotted and compared in Fig. 5.19 a and b. As stated in Chapter 3, the high entropy generation in the abrupt entrance, predicted by the model, is due to the separation and the resulting losses in the flow expansion after the vena contracta. However, due to the reasons stated earlier, no separation is observed in the experiments and the total

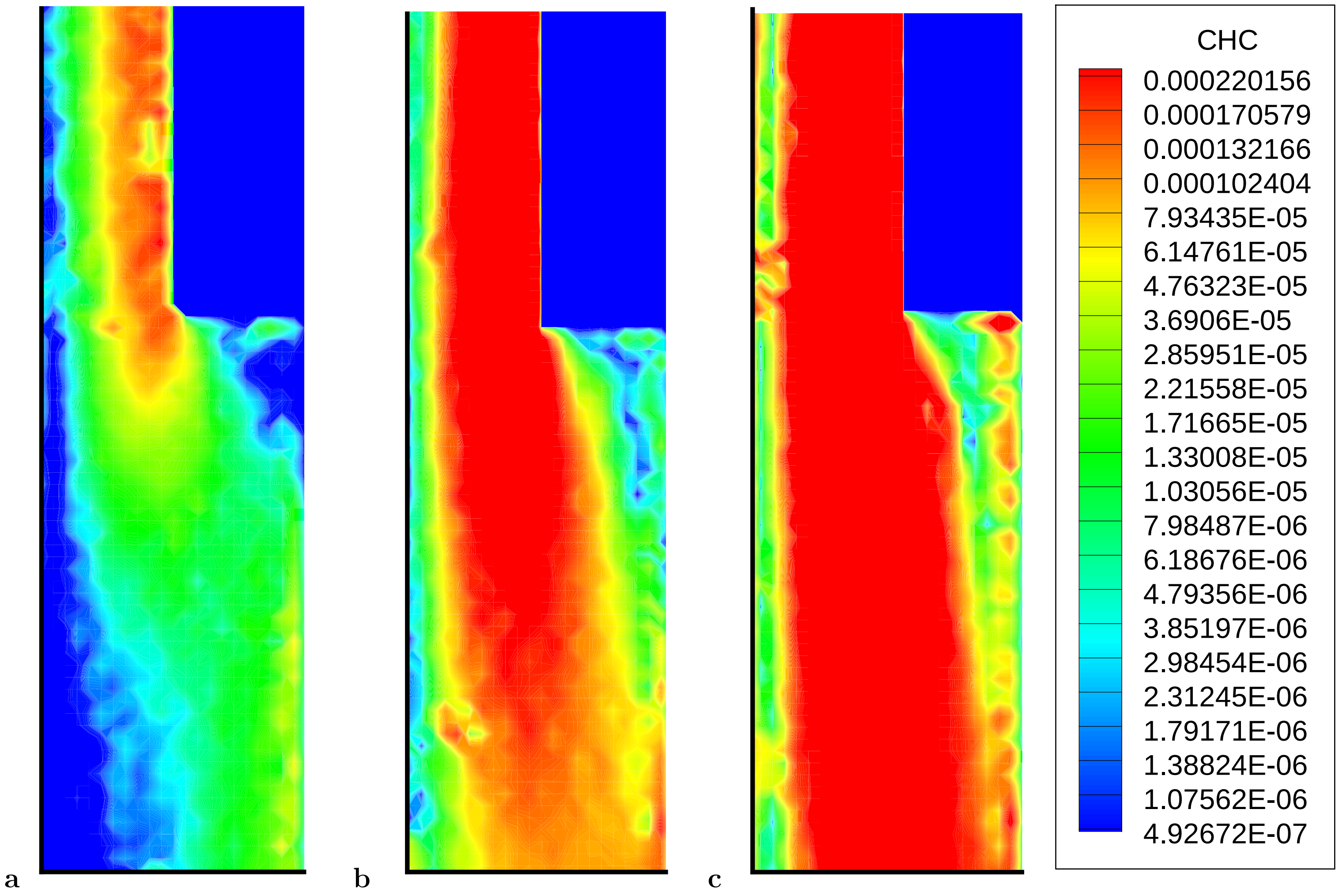

Figure 5.10: Entropy generation constant contours at the rectangular exit, at flow rates of 100, 300, and 500 $\mu l/min$

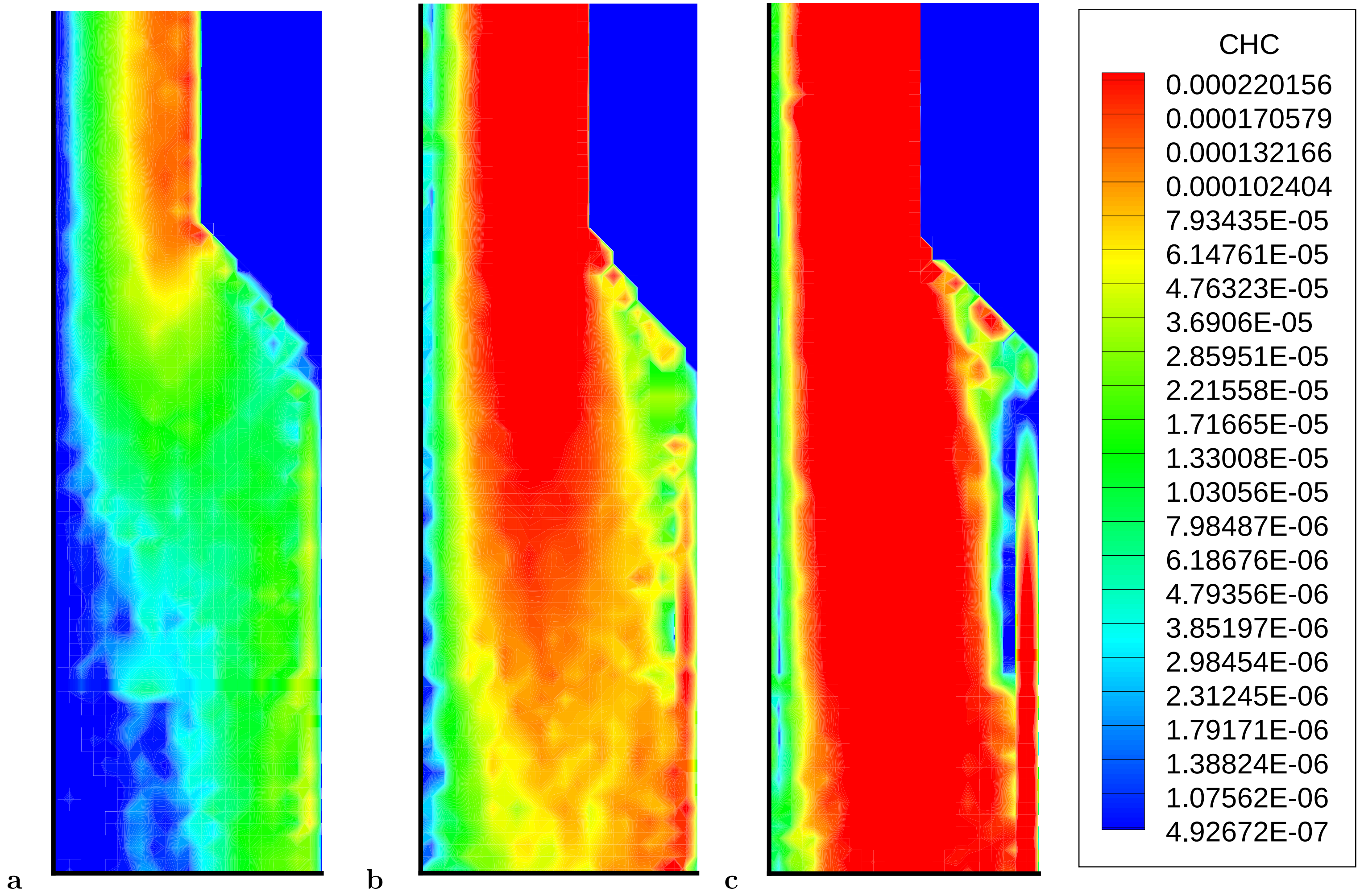

Figure 5.11: Entropy generation constant contours at the triangular exit, at flow rates of 100, 300, and 500 $\mu l/min$

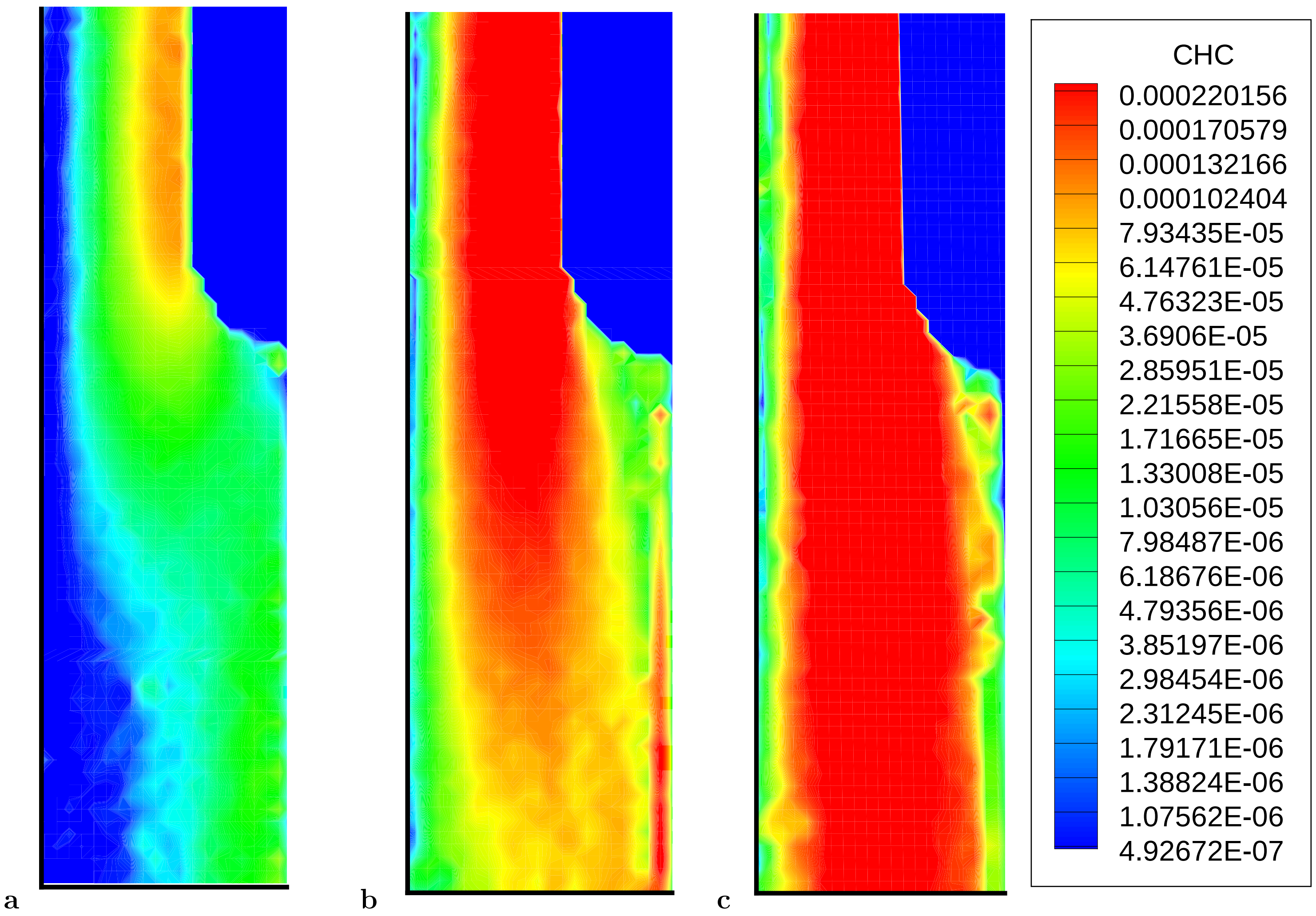

Figure 5.12: Entropy generation constant contours at the circular exit, at flow rates of 100, 300, and 500 $\mu l/min$

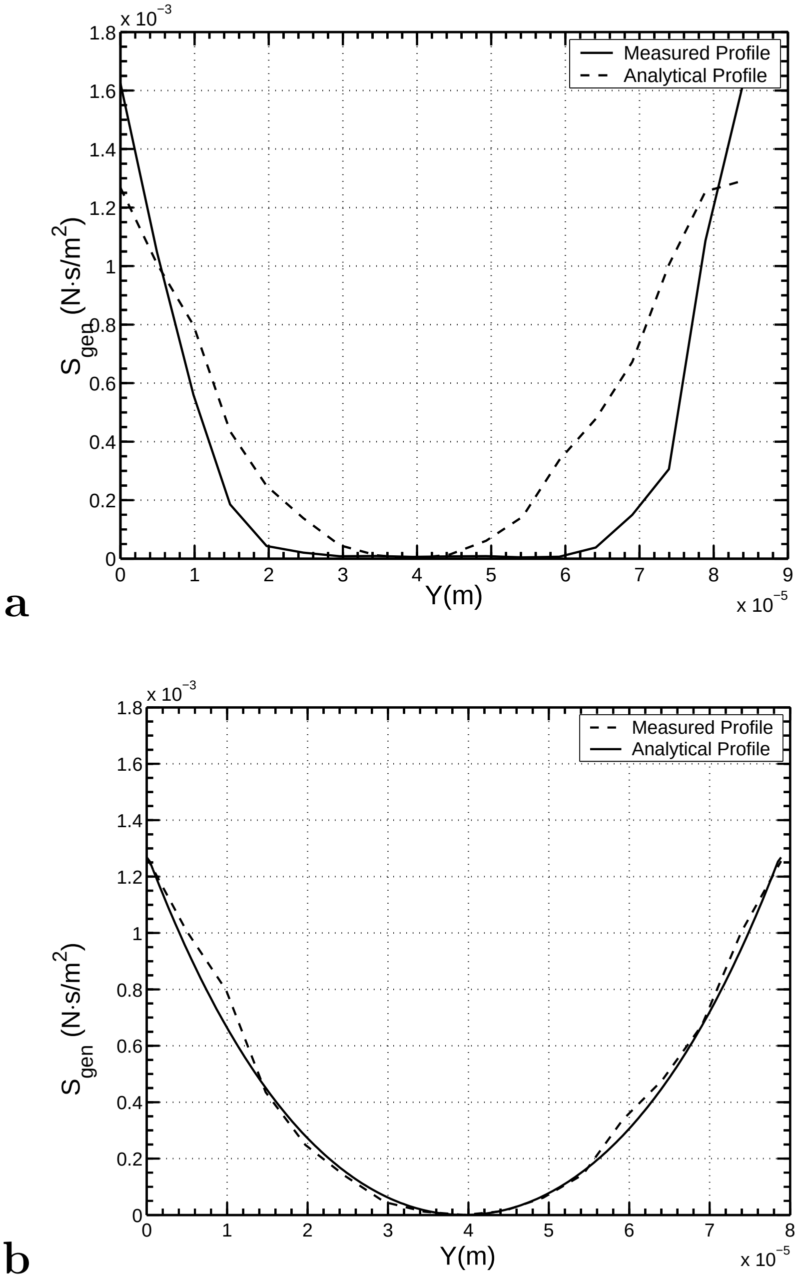

Figure 5.13: Entropy generation profiles in the developing region (a) and fully developed region (b) of the channel compared to analytical fully developed profile

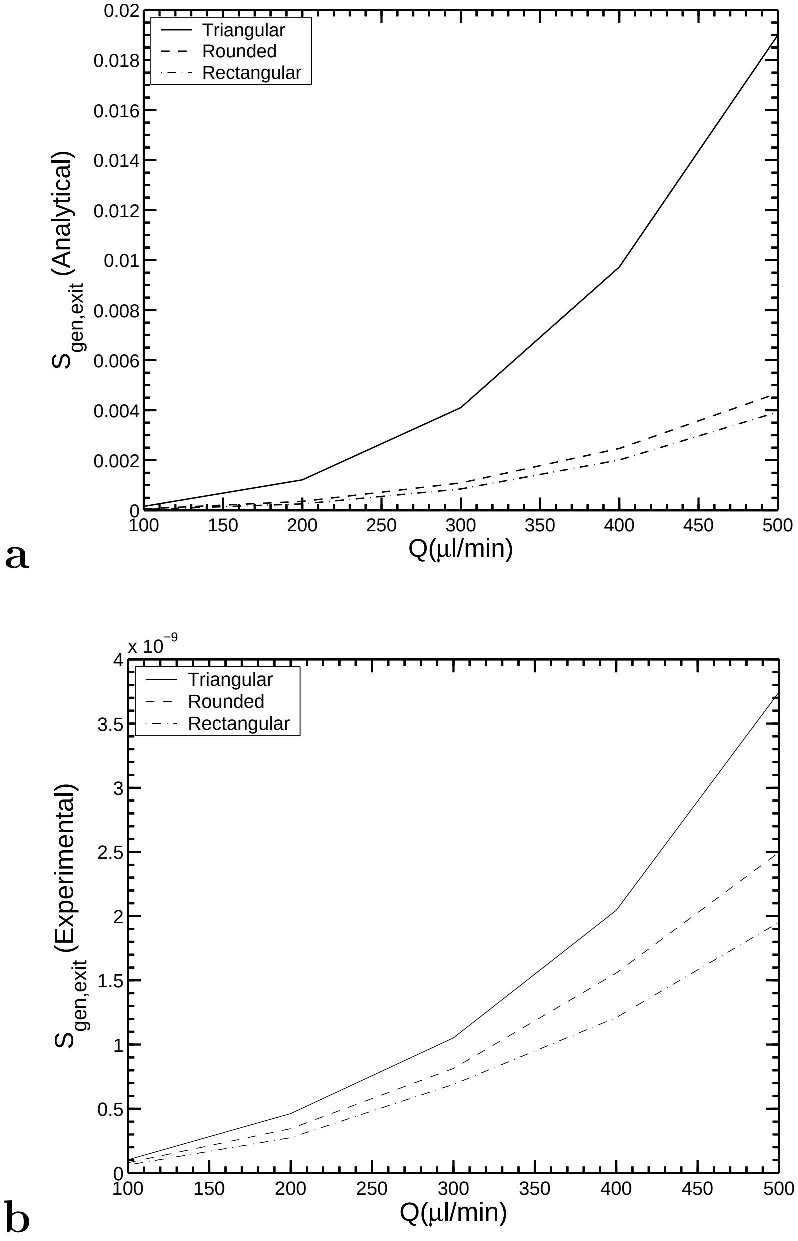

Figure 5.14: (a) The results of the model for total entropy generation at the exit of the microchannels (b) The measurement results for entropy generation at a plane in the middle of the exit section

Note that the model yield the entropy generation in the whole volume of the transition between small and large channels; but the model gives the entropy generation in a plane in the middle of the channel.

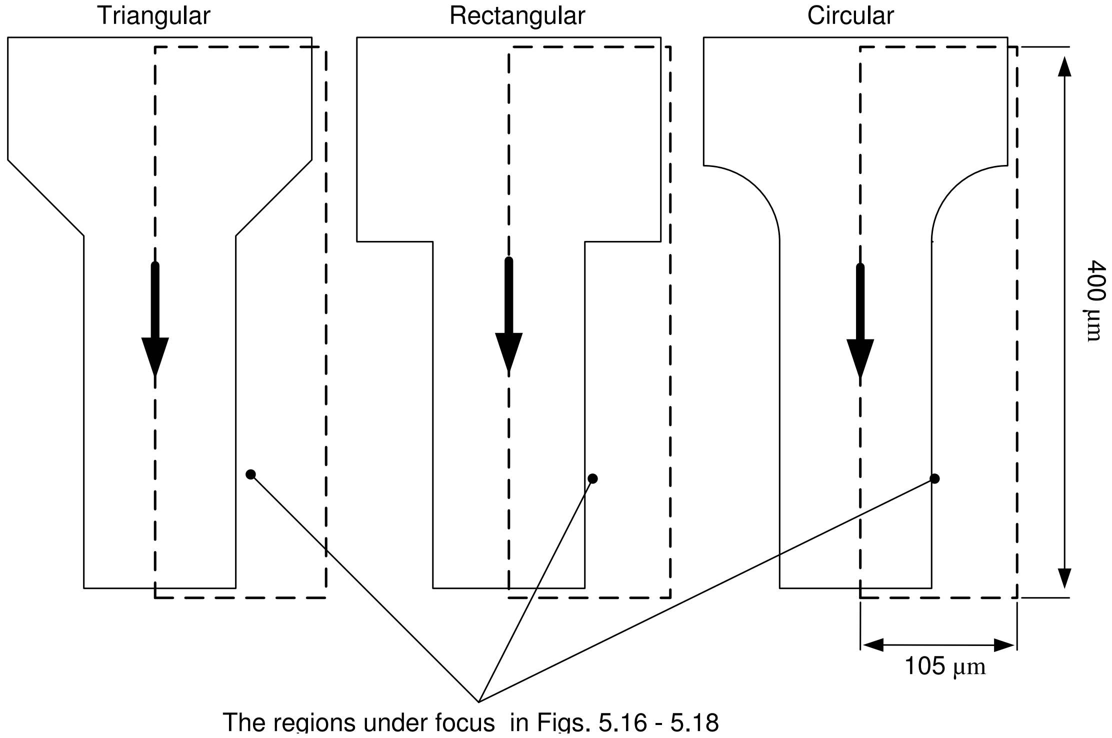

Figure 5.15: The location and size of the regions at the entrance of the microchannels whose entropy generation constant contours are sketched in Figs. 5.16 to 5.18

measured entropy generation in the abrupt entrance is lower than the circular and triangular geometries. The values of entropy generation in the entrance of the microchannels, calculated by the model and through the measurements have been given in Table 5.3.

5.4 Temperature Measurement

A schematic of the LIF measurement test setup is shown in Fig. 5.20. A 2″ × 1″ flexible heater, from Minco, is attached on top of the silicon microchannels using a layer of thermal interface material, from Thermagon. The measurements are done under the constant outer surface temperature boundary condition, at $90°C$. The temperature on the side walls of the microchannel is expected to be the same, due to the very small thickness and high conduc-

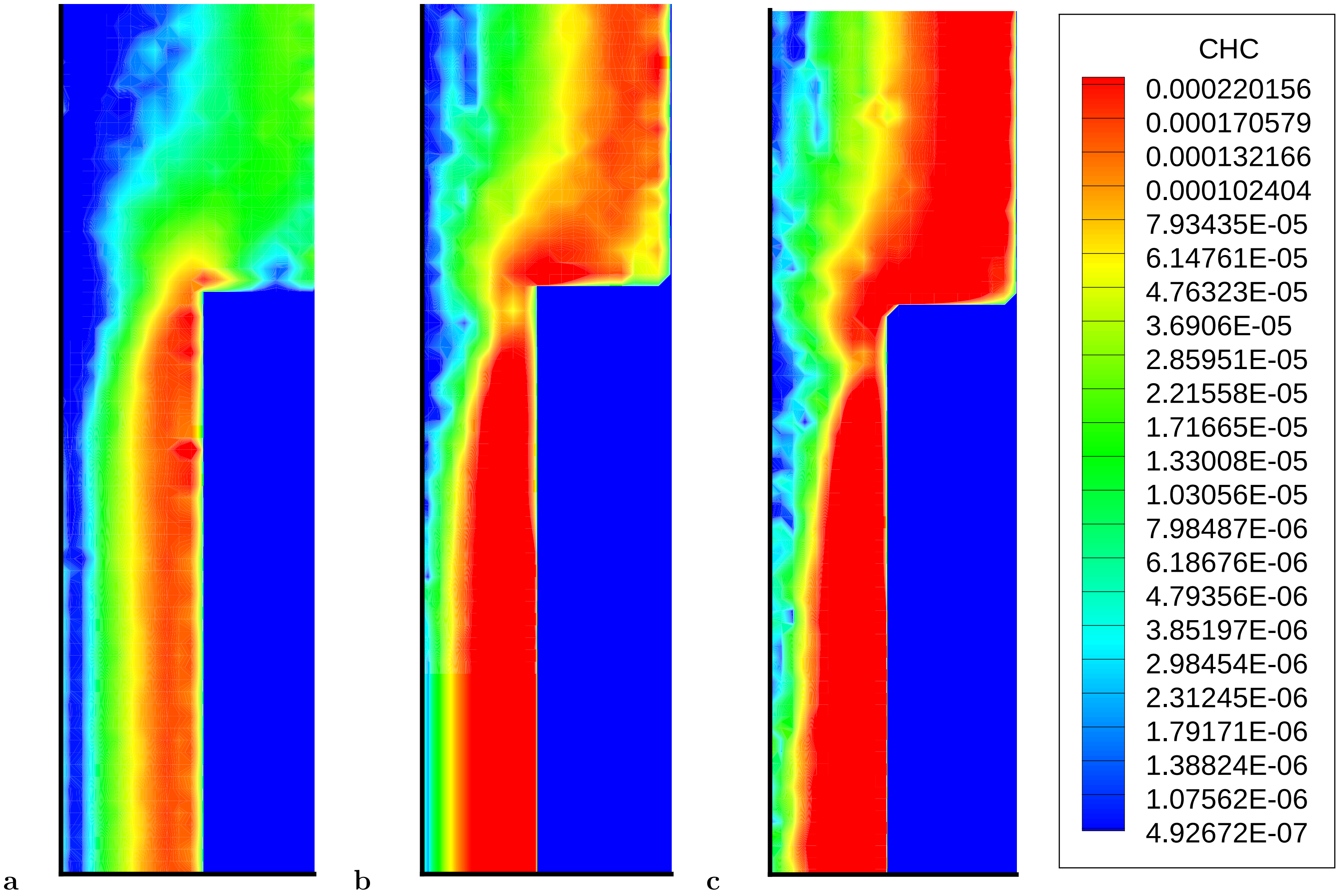

Figure 5.16: Entropy generation constant contours at the rectangular inlet, at flow rates of 100, 300, and 500 $\mu l/min$

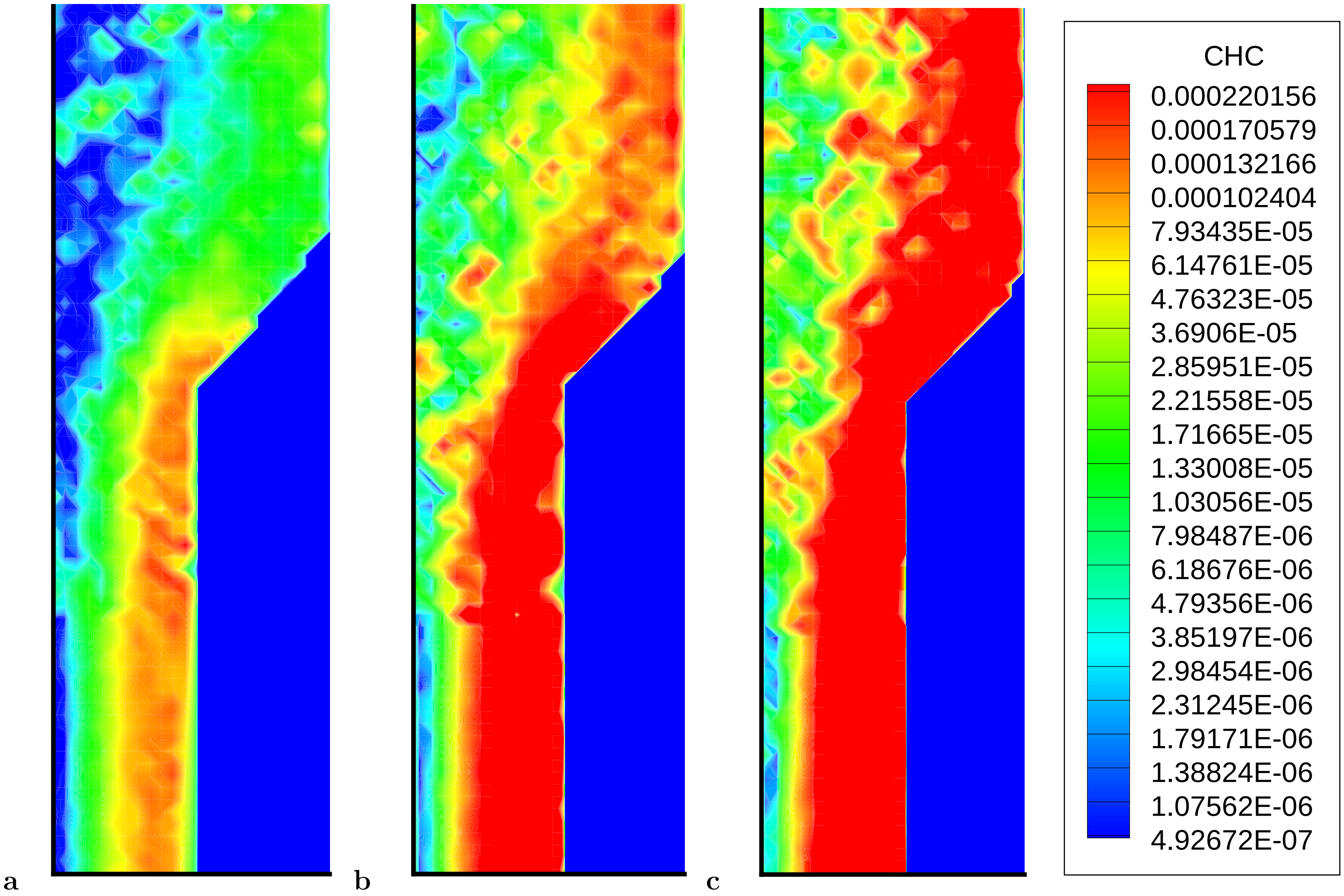

Figure 5.17: Entropy generation constant contours at the triangular inlet, at flow rates of 100, 300, and 500 $\mu l/min$

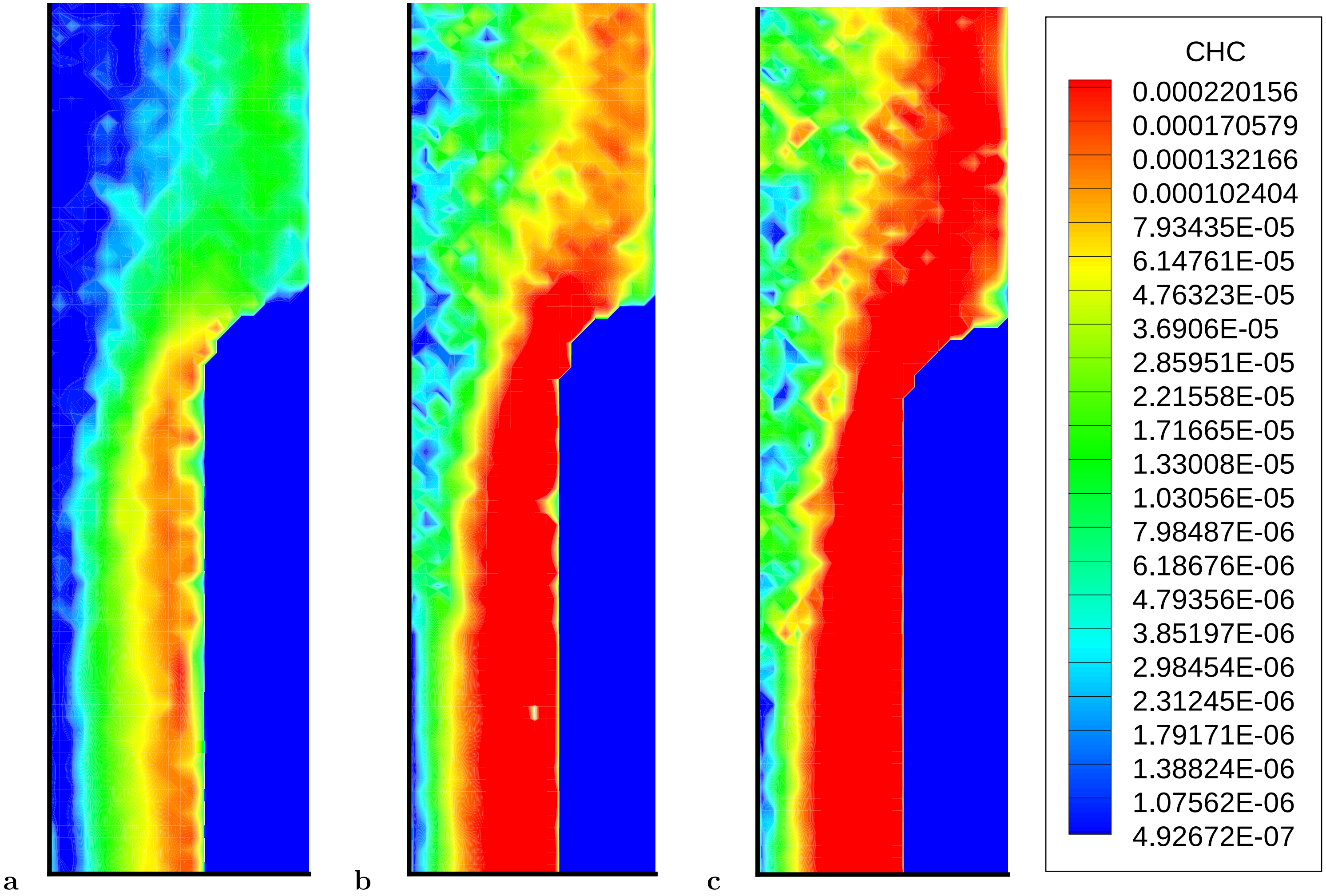

Figure 5.18: Entropy generation constant contours at the circular inlet, at flow rates of 100, 300, and 500 $\mu l/min$

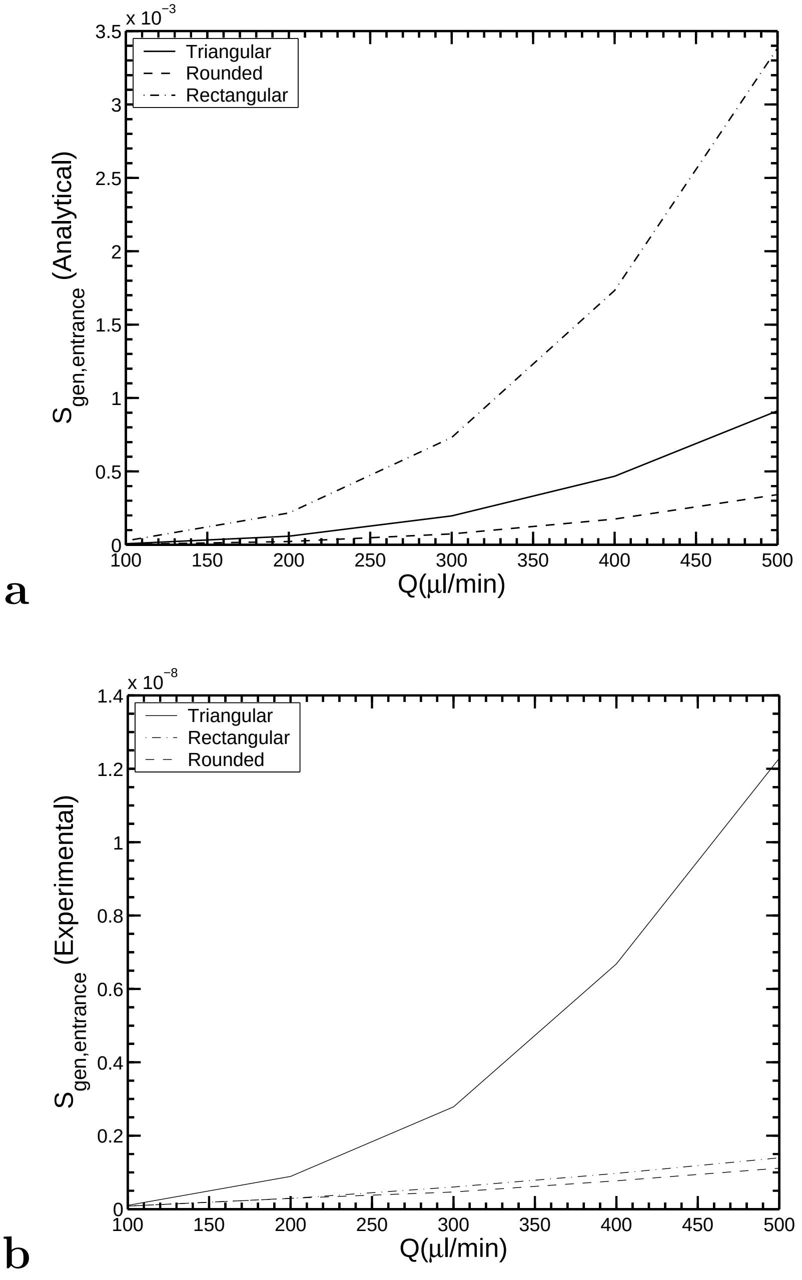

Figure 5.19: (a) The results of the model for total entropy generation at the inlet of the microchannels. (b) The measurement results for entropy generation at a plane in the middle of the inlet section
Note that The model yield the entropy generation in the whole volume of the transition between large and small channels; but the model gives the entropy generation in a plane in the middle of the channel.

Table 5.3: Results of the model and measurements for entropy generation in the entrance of the microchannel

Channel Geometry	Q $(\mu l/min)$	$\dot{S}_{gen,model}$ (J/K)	$\dot{S}_{gen,experiment}$ (J/K)
Rectangular	100	2.7e-5	8.2e-11
	200	2.2e-4	2.9e-10
	300	7.3e-4	6.0e-10
	400	1.7e-3	9.7e-10
	500	3.4e-3	1.4e-09
Triangular	100	7.3e-6	1.0e-10
	200	5.8e-5	8.9e-10
	300	2.0e-4	2.8e-09
	400	4.7e-4	7.5e-09
	500	9.1e-4	1.2e-08
Circular	100	2.7e-6	8.0e-11
	200	2.2e-5	2.9e-10
	300	7.4e-5	4.7e-10
	400	1.7e-4	7.7e-10
	500	3.4e-4	1.1e-09

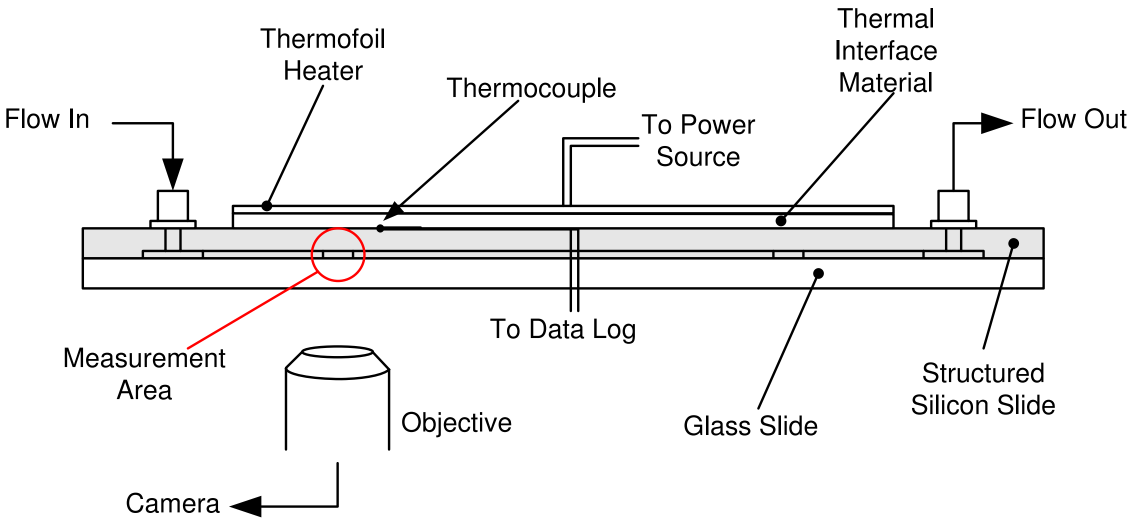

Figure 5.20: Schematic of the LIF measurements test setup

tivity of the silicon substrate. The temperature on the microchannel top surface is recorded using a thermocouple placed between the thermal interface layer and the microchannel.

The isotherms in the inlet and exit sections of the microchannels have been plotted in Figs. 5.22 - 5.25. The location and size of the measurement area is shown in Fig. 5.21. At smaller flow rates, in the exit region, the fluid is exposed to the hot channel walls for a longer period of time, therefore, heat can penetrate deeper into the fluid and the core of the flow is affected by the high temperature on the walls. As the flow rate increases, the thickness of the high temperature fluid layer, adjacent to the walls, decreases and the core regions of the flow are not affected by the heat transfer from the walls. Figure 5.22 clearly shows this trend in the rounded exit of the microchannel. At a flow rate of 100 $\mu l/min$, the entire area of the flow is influenced by the heat transfer from the side walls; while at a flow rate of 500 $\mu l/min$, a thin thermal boundary layer forms near the walls and the majority of the flow remains at approximately the inlet temperature. The measurements show that the

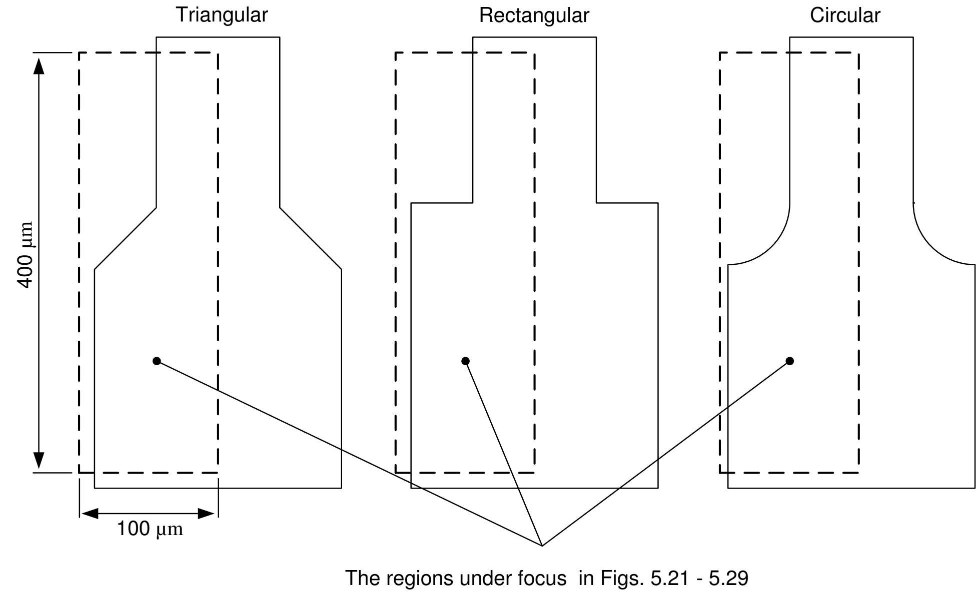

Figure 5.21: Location and size of the regions at the exit and inlet of the microchannels whose thermal entropy generation and temperature contours are sketched in this section

temperature of the fluid is higher than $90°C$ adjacent to the walls. This false reading may be attributed to near wall effects, like higher reflectivity on the side walls, or inaccuracies in the measurement of surface temperature. The measured temperature data are transformed onto a 16 pixel × 16 pixel grid, so that the spacing between the velocity vectors and temperatures are the same.

The same behavior as that in the exit section is observed in the channels with triangular and rectangular exits. Figure 5.23 shows the temperature distribution in the rectangular exit at the flow rate of $100\,\mu l/min$ and in the triangular exit at a flow rate of $500\,\mu l/min$.

The temperature of the fluid in the entrance of the microchannel is affected only in a thin layer near the walls, regardless of the flow rates, because of the low residence time of the fluid inside the channel.

The temperature profiles in two cross sections of the flow, one in the wide ($200\mu m$) and one in the narrow ($100\mu m$) sections, of the triangular exit are sketched in Fig. 5.26 for the

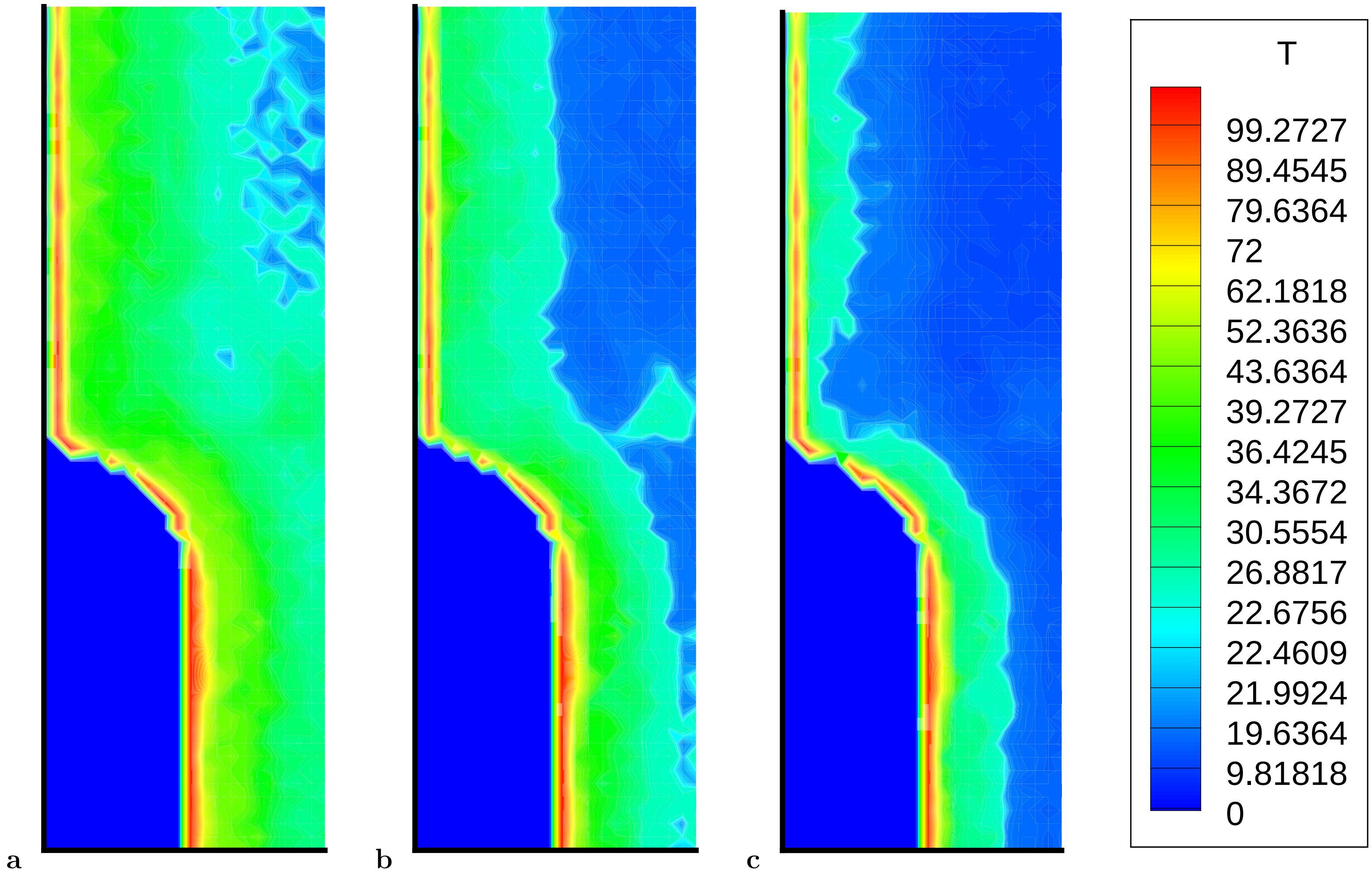

Figure 5.22: Temperature distribution in the flow at the rounded exit section of the microchannel, at a constant surface wall temperature of $90°C$, at flow rates of 100, 300, and 500 $\mu l/min$

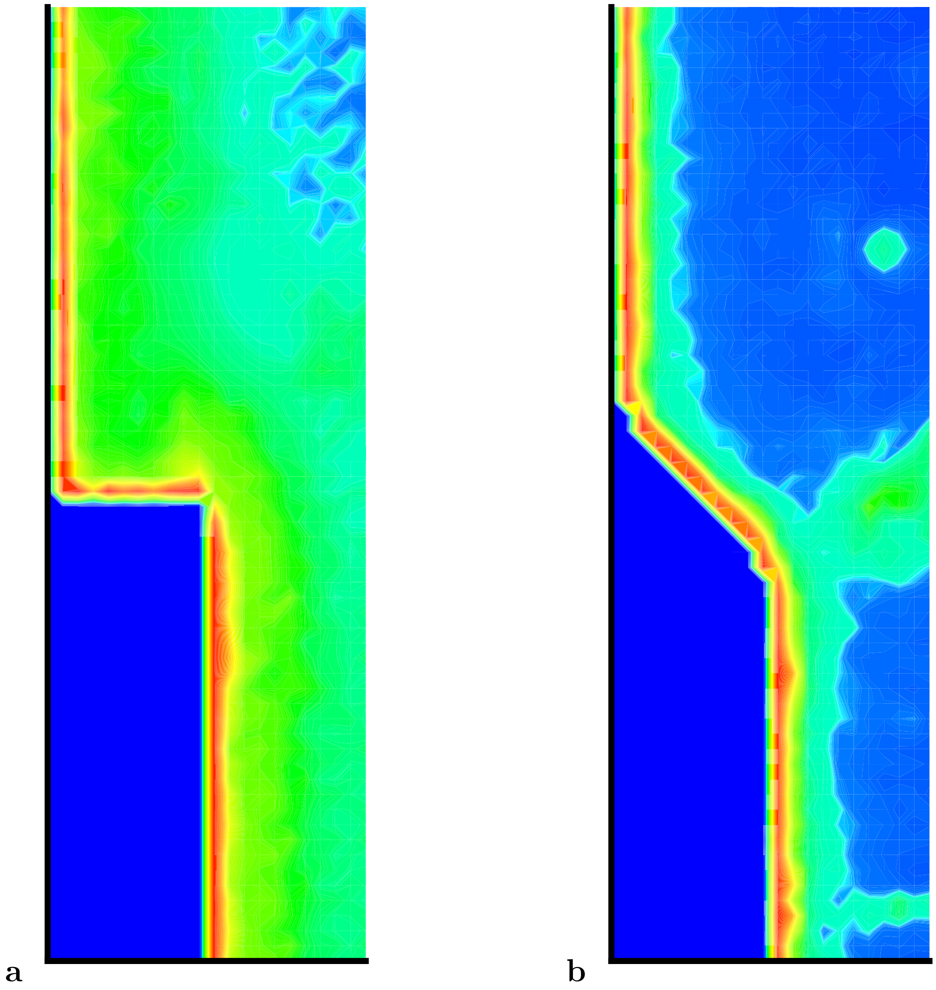

Figure 5.23: Temperature distribution in the flow at the rectangular and triangular exit sections of the microchannel, at a constant surface wall temperature of $90°C$, at flow rates of 100, and 500 $\mu l/min$, respectively.

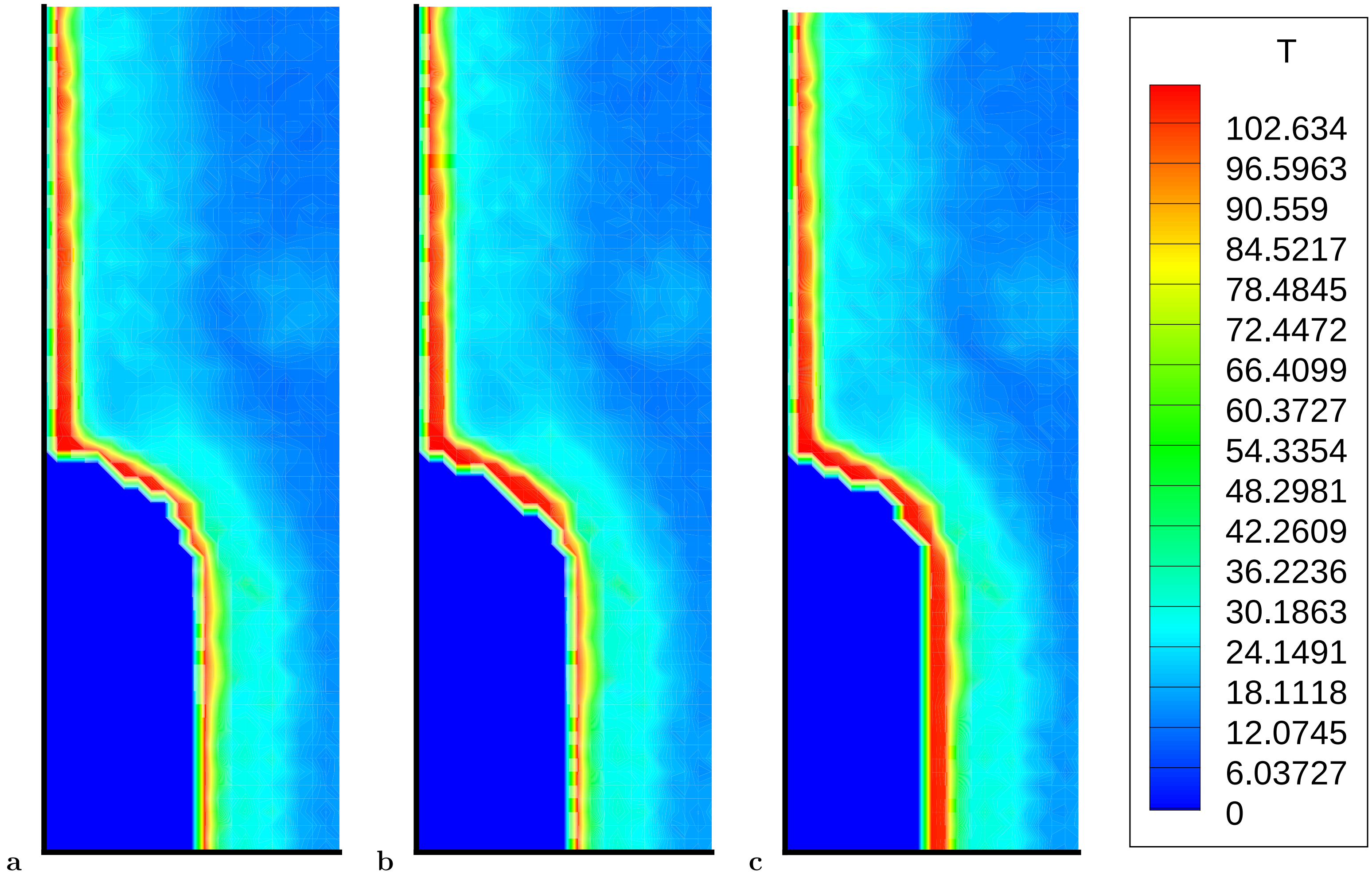

Figure 5.24: Temperature distribution in the flow at the rounded inlet section of the microchannel, at a constant surface wall temperature of $90^{\circ}C$, at flow rates of 100, 300, and 500 $\mu l/min$

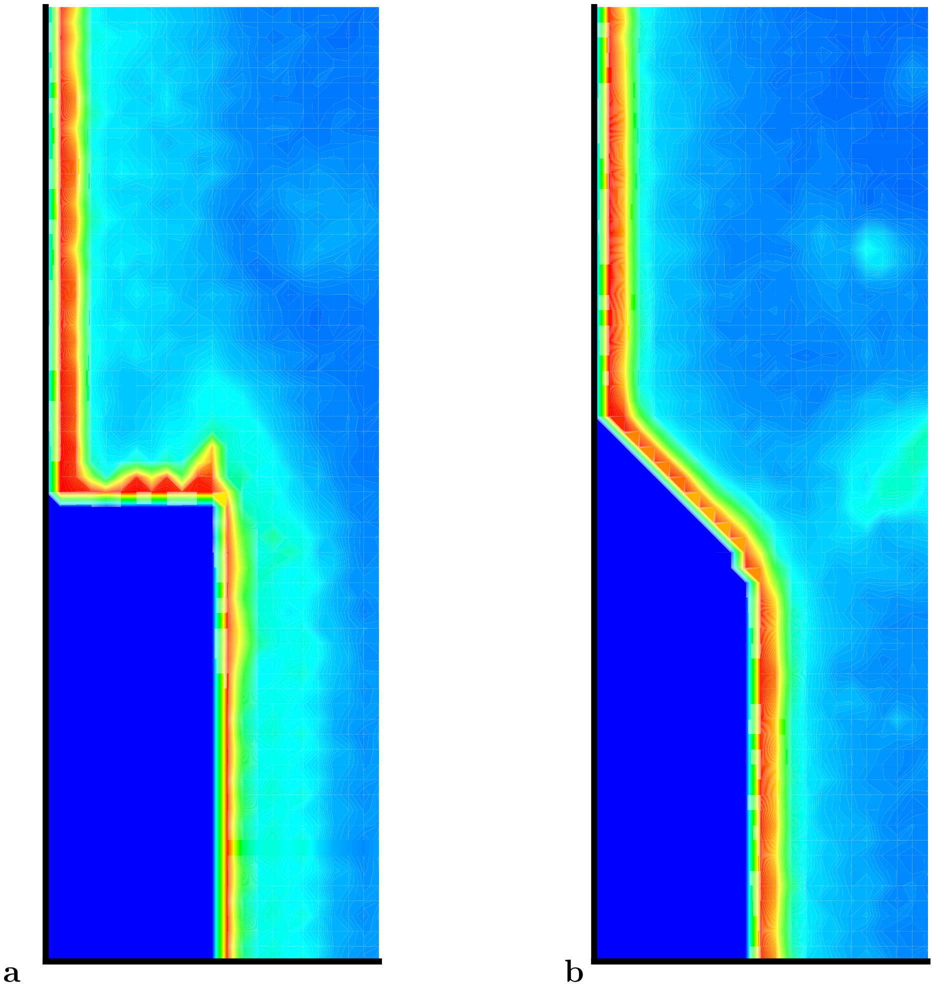

Figure 5.25: Temperature distribution in the flow at the rectangular and triangular inlet sections of the microchannel, at a constant surface wall temperature of $90°C$, at flow rates of 100, and $500\,\mu l/min$, respectively.

two flow rates of 100 and 500 $\mu l/min$. In both flow rates, there is a significant temperature rise in a thin boundary layer ($\sim 20\,\mu m$) adjacent to the walls. The flow temperature is lower for the case of 500 $\mu l/min$ flow rate due to the smaller flow residence time in the microchannel.

5.5 Thermal Entropy Generation

After determining the temperature distribution on a discrete grid, the thermal entropy generation rate can be calculated using the following equation (see Chapter 1):

$$\dot{S}'''_{gen} = \frac{k}{T^2}\left[\left(\frac{\partial T}{\partial x}\right)^2 + \left(\frac{\partial T}{\partial y}\right)^2\right] \tag{5.1}$$

The discretized form of the above equation is:

$$\dot{S}'''_{gen} = \frac{k}{T(i,j)^2}\left[\left(\frac{T(i+1,j)-T(i-1,j)}{\Delta x}\right)^2 + \left(\frac{T(i,j+1)-T(i,j-1)}{\Delta y}\right)^2\right] \tag{5.2}$$

It is expected that the entropy generation has its highest value adjacent to the side walls, where the temperature gradient is highest. The thermal entropy generation constant contours are plotted in Figures 5.27 to 5.30 for the flow rates of 100, 300, and 500 $\mu l/min$ and all three exit and entrance geometries. As anticipated, the maximum thermal entropy generation occurs near the side walls. The difference between the entropy generation distribution and entropy generation values are not noticeable for different flow rates in these plots, because the side wall and inlet flow temperatures are identical, leading to close values of temperature gradient and entropy production rates.

The total amount of thermal entropy production in the midplane of the inlet and exit sections of the microchannels are calculated and presented in Table 5.4. In general, the entropy production rates are decreasing with flow rate. The reason is the reduction in the thermal boundary layer thickness (see Fig. 5.22) and steeper temperature gradient

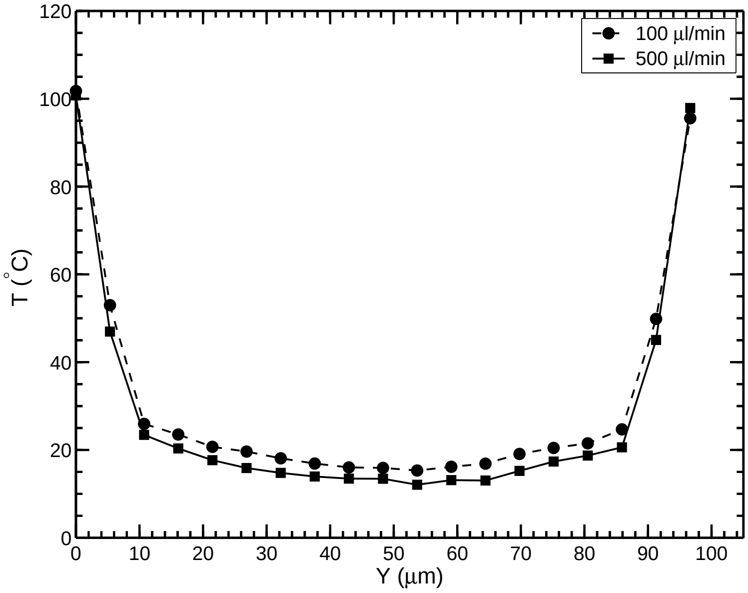

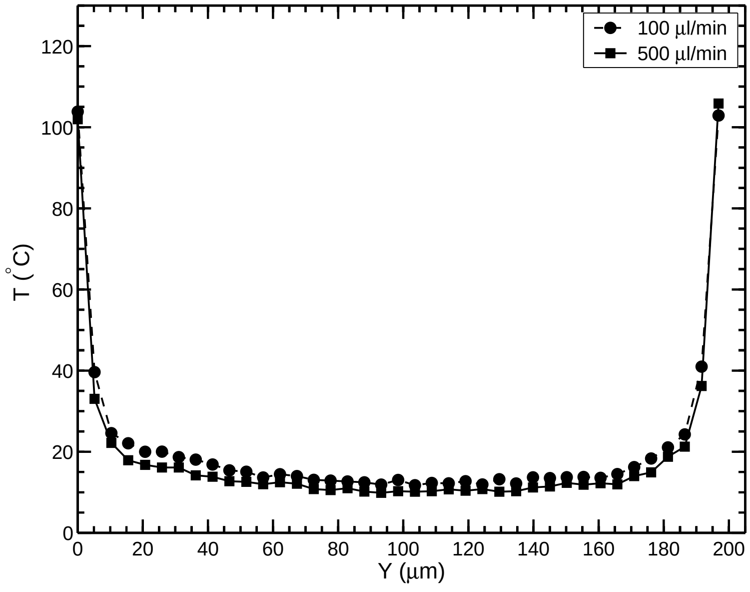

Figure 5.26: Temperature profiles in the 100 μm wide (a) and 200 μm wide (b) sections at the exit of the triangular microchannel

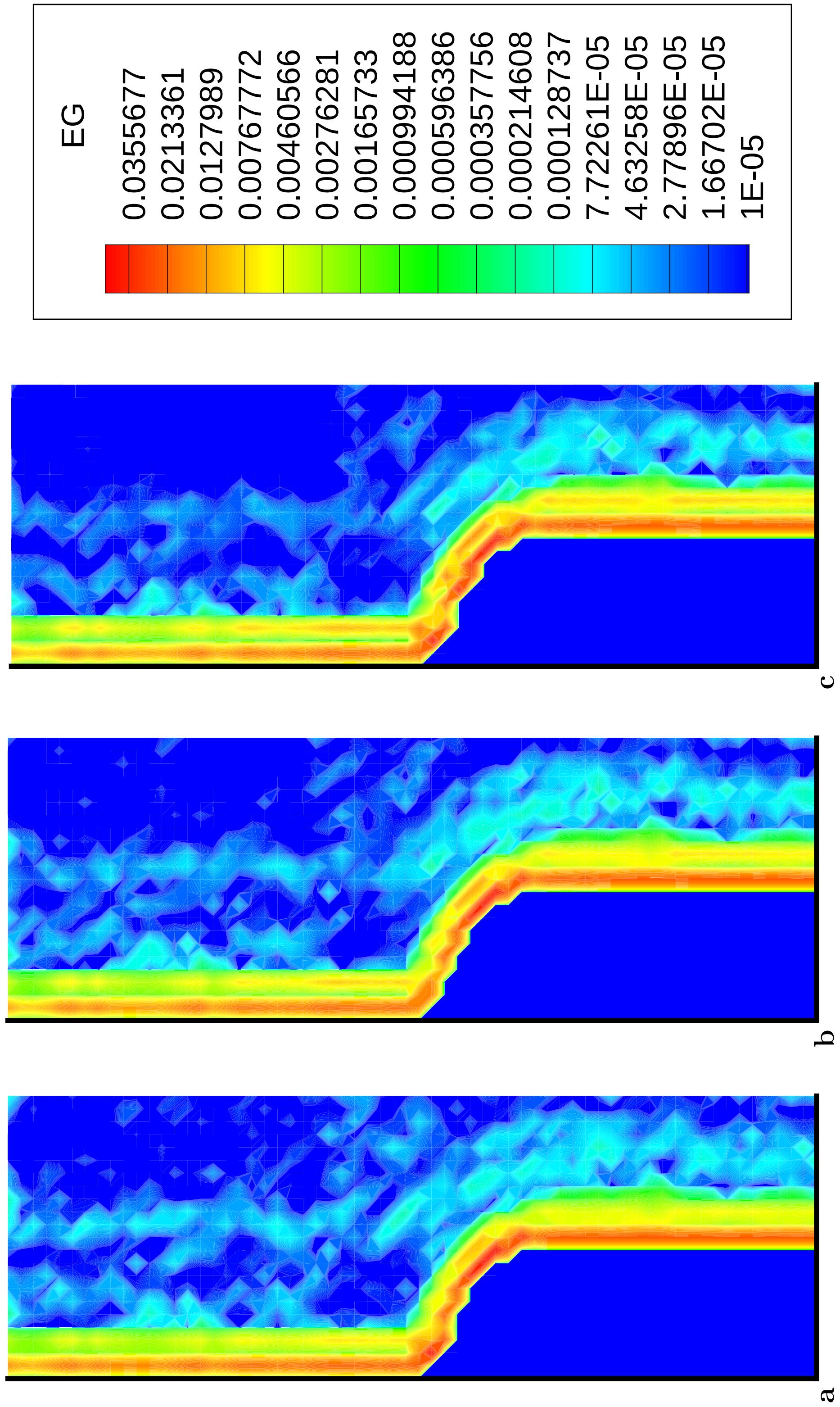

Figure 5.27: Thermal entropy generation distribution in the flow at the rounded exit section of the microchannel, at a constant surface wall temperature of 90°C, and at flow rates of 100, 300, and 500 $\mu l/min$

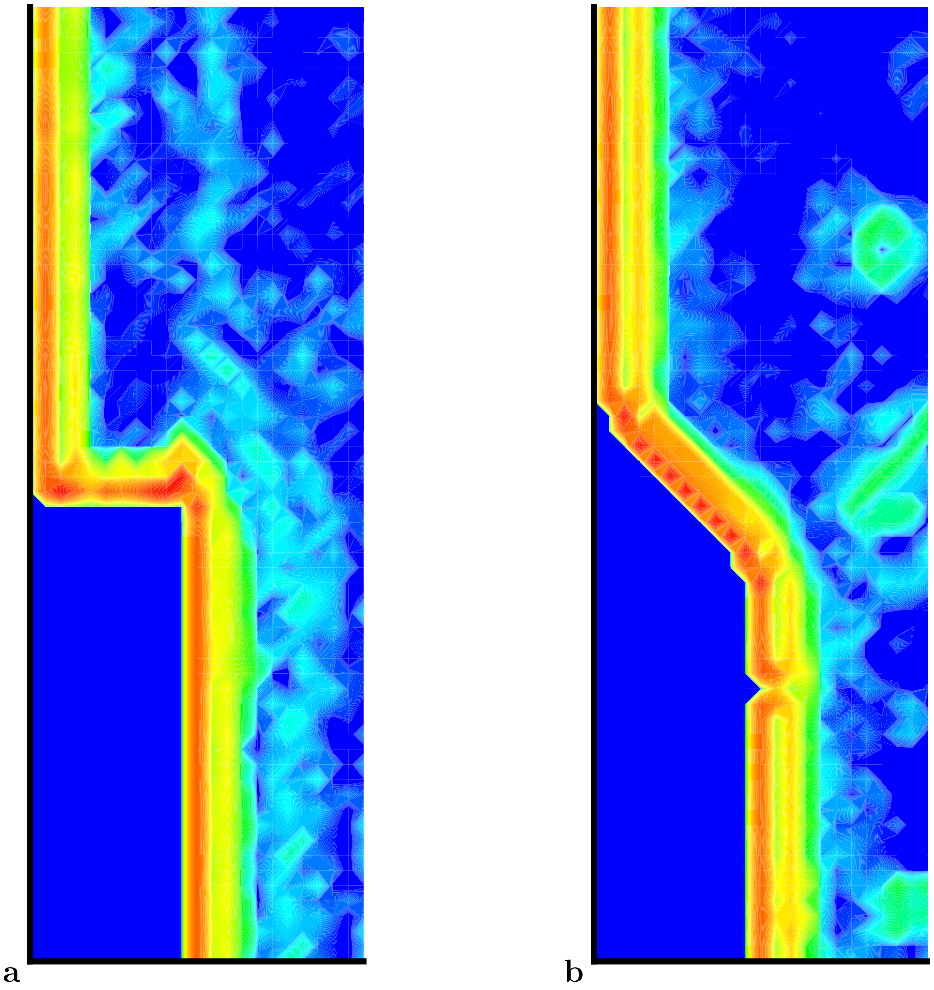

Figure 5.28: Thermal entropy generation distribution in the flow at the rectangular and triangular exit sections of the microchannel, at a constant surface wall temperature of $90°C$, and at flow rates of 100, and 500 $\mu l/min$, respectively

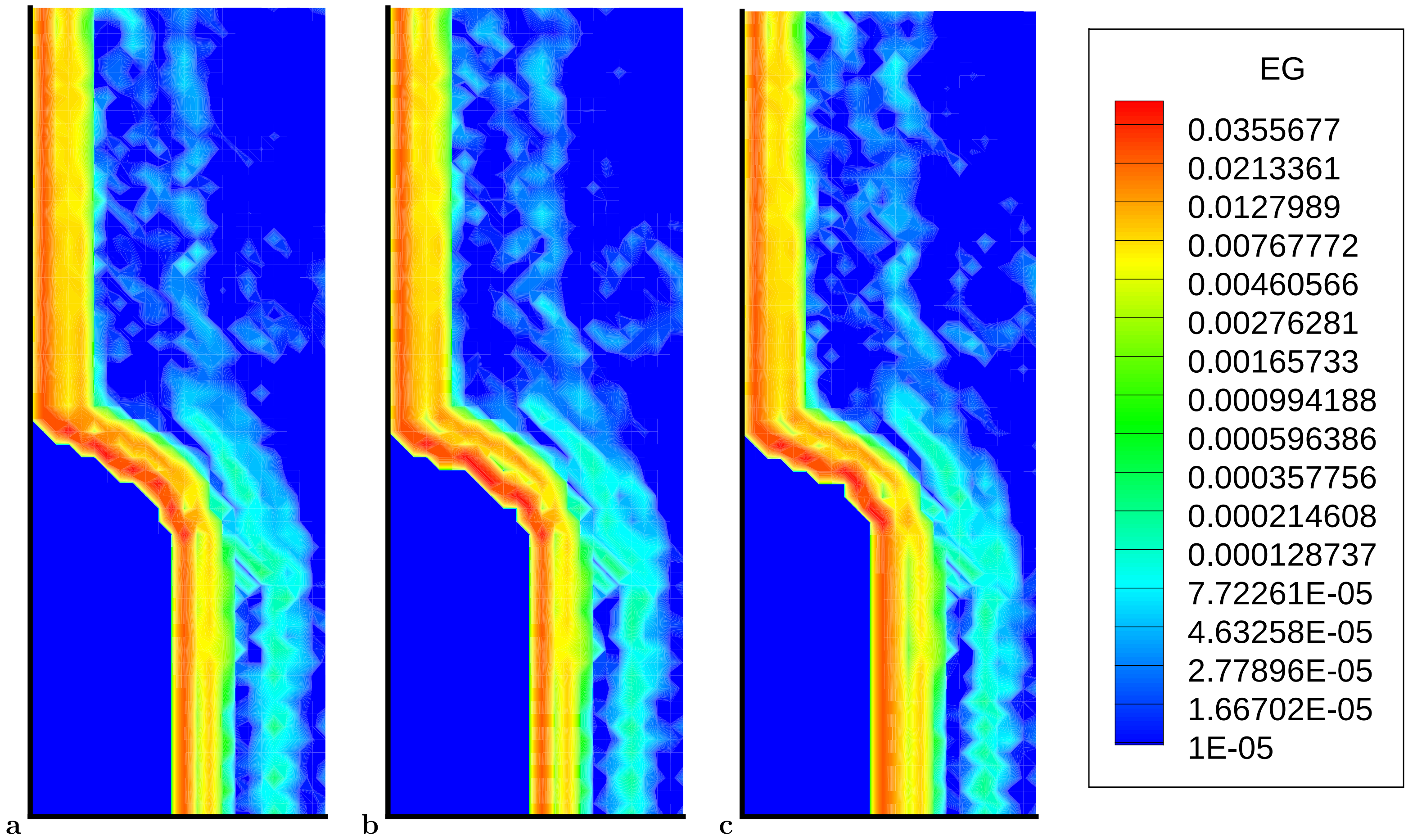

Figure 5.29: Thermal entropy generation distribution in the flow at the rounded inlet section of the microchannel, at a constant surface wall temperature of 90°C, and at flow rates of 100, 300, and 500 $\mu l/min$

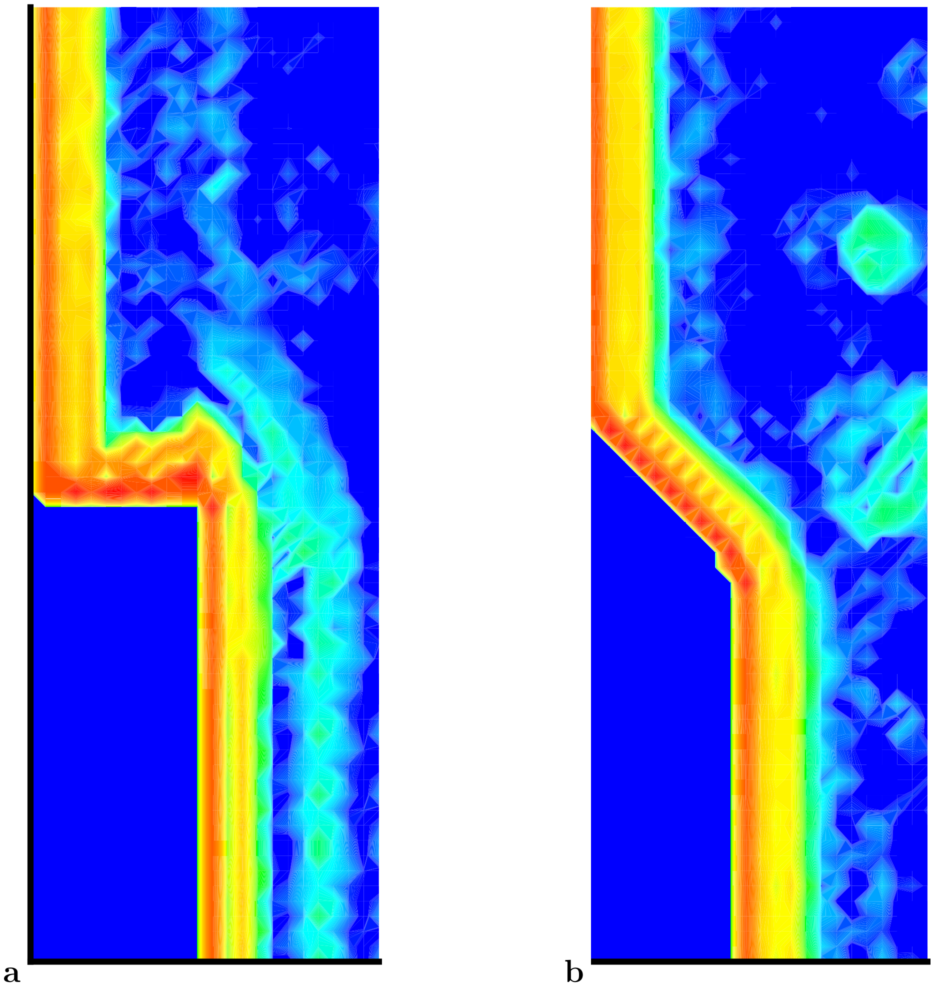

Figure 5.30: Thermal entropy generation distribution in the flow at the rectangular and triangular inlet sections of the microchannel, at a constant surface wall temperature of $90°C$, and at flow rates of 100, and 500 $\mu l/min$, respectively

Table 5.4: Results of the measurements for thermal entropy generation in the entrance and exit of the microchannels

Channel Geometry	Q $(\mu l/min)$	$\dot{S}_{gen,exit}$ (J/K)	$\dot{S}_{gen,inlet}$ (J/K)
Rectangular	100	4.5e-1	5.6e-1
	200	4.4e-1	5.3e-1
	300	4.7e-1	5.1e-1
	400	4.6e-1	5.0e-1
	500	4.2e-1	4.5e-1
Triangular	100	4.4e-1	5.7e-1
	200	4.6e-1	6.0e-1
	300	4.3e-1	5.6e-1
	400	4.3e-1	5.3e-1
	500	4.2e-1	4.9e-1
Circular	100	5.0e-1	5.5e-1
	200	4.8e-1	5.7e-1
	300	4.7e-1	5.3e-1
	400	4.7e-1	5.0e-1
	500	4.4e-1	4.7e-1

neighboring the side walls, which increases the convection heat transfer coefficient and brings down the convection thermal resistance. As stated in Chapter 1 (Eq. 1.16), the thermal entropy generation rate is directly proportional to the thermal resistance.

5.6 Total Entropy Generation

The thermal entropy generation rates are 2 to 5 orders of magnitude larger than the frictional entropy generation rates in this study, and as a result, are the dominant term in total entropy generation rate. At flow rates higher than in this study, the increasing velocity gradients cause the frictional entropy generation to catch up with the thermal entropy generation rate.

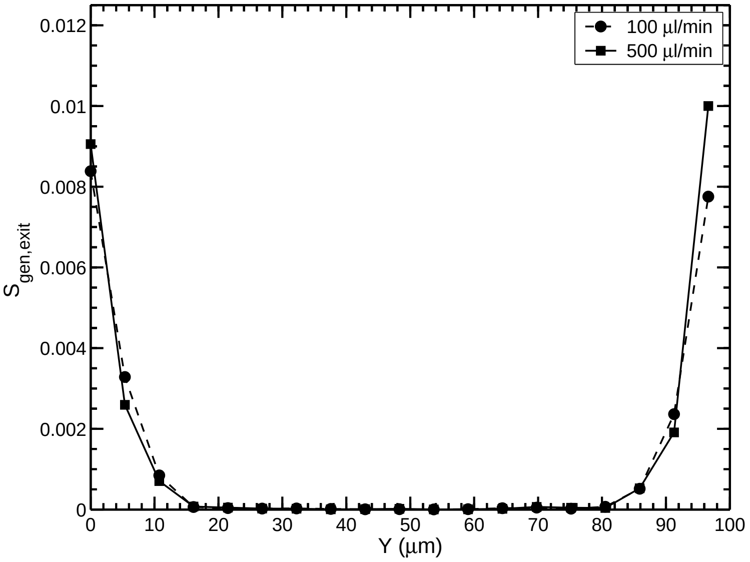

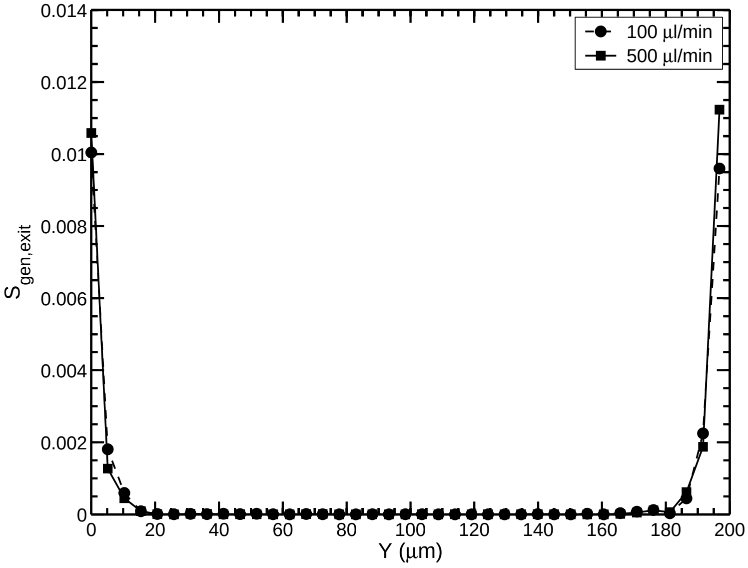

Figure 5.31: Thermal entropy generation profiles in the 100 μm wide (a) and 200 μm wide (b) sections at the exit of the triangular microchannel

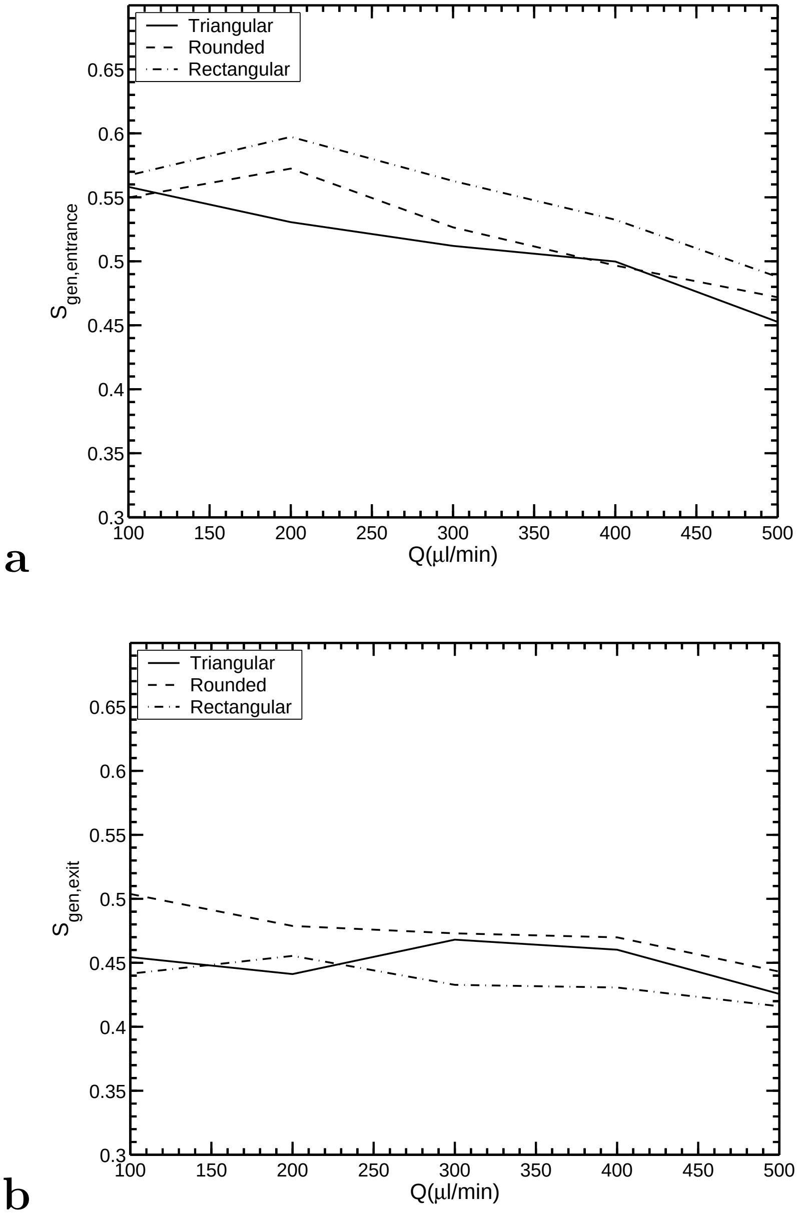

Figure 5.32: Variations of thermal entropy generation with flow rate in the inlet and exit of the microchannels

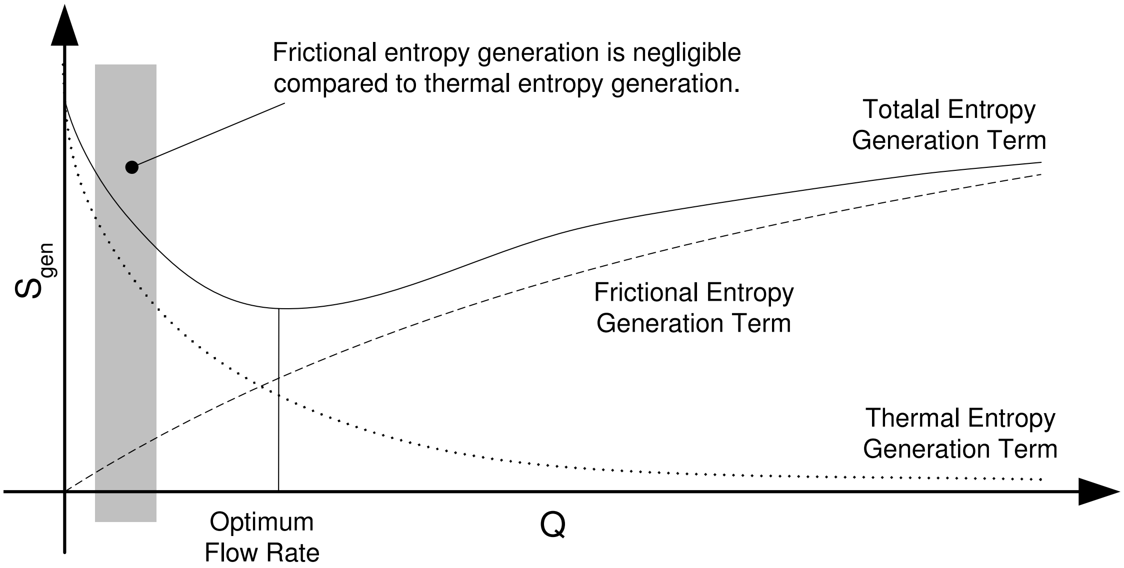

Figure 5.33: A schematic of the flow rate range under study in this work in relation to the thermal and frictional entropy generation rates.

A schematic of the flow rate range under study in this work in relation to the thermal and frictional entropy generation rates is shown in Fig. 5.33.

Chapter 6

Conclusions

The primary goal of this research is to develop a general model capable of predicting the entropy generation rate of liquid flows through the microchannels of a heat-sinks. This model is a powerful design tool, allowing the production of microchannel heat-sinks with optimum thermal and hydrodynamic performance. An experimental technique for measuring entropy production of laminar flow and forced convection in microchannels, using the combined PIV/LIF methods, has also been presented. The following conclusions can be reached from this work:

- The heat transfer and pressure drop models are based on using the square root of cross-sectional area as the characteristic length, instead of the standard hydraulic diameter. The advantage of using $\sqrt{A_{cs}}$ is that the friction factor and Nusselt number data for channels with a wide range of cross-sectional geometries and aspect ratios collapse on each other and a single relationship is required to determine the data for all shapes. By comparison with the available data in the literature, it was demonstrated that the models based on this approach, yield accurate results in micro-scale applications.
- Analytical expressions for pressure loss at the exit and entrance of the channels were

also developed. An additional pressure drop and thus excess entropy is produced at entrance and exit of microchannels. It was shown that, using a tapered exit with a small angle (less than 8°) reduces the pressure losses in the exit of the channel; while at larger angles, the combined effects of friction and separation increase losses dramatically, even more than the abrupt area change. However, at the entrance of the channel, the abrupt contraction generates the highest amount of entropy among the geometries under study, because of the formation of vena contracta and losses associated with the expansion after that.

- The results of the model indicate that there exists an optimum point, i.e. a point with minimum entropy production, for changes in Reynolds number and aspect ratio of the channel.

- Pressure drop and heat transfer rise with increasing Reynolds number. As a result, the frictional entropy generation grows and the thermal term shrinks as Reynolds number increases.

- The increase in aspect ratio, i.e. decrease in channel slenderness, leads to smaller pressure drops and heat transfer rates. Therefore, the frictional entropy generation term goes down and the thermal term increases with increasing aspect ratio.

- The laser based method described in this work enables the non-intrusive, whole-field and time-varying measurement of entropy generation within the microchannels. The conventional methods of entropy generation measurement used standard anemometry techniques to measure pressure and temperature at single point, or yield a global rate of entropy generation in the system.

- Using the new technique presented here, engineers can have a detailed structure of entropy generation in the system and target the spots with high entropy generation rates and redesign them to enhance the overall efficiency of the system.

- A combination of micro-PIV and micro-LIF systems were used to determine the local temperature and velocity values, respectively, over a discrete grid. A discretized expression for the local entropy generation rate was developed as a function of temperature and velocity. By postprocessing the velocity and temperature data using this expression, entropy generation maps were developed at the exit and entrance regions of the microchannel.

- Frictional entropy generation has its maximum value near the side walls of the channel and in the shear layer of the stream coming out of the microchannel which have high velocity gradient.

- Thermal entropy generation has its maximum value adjacent the side walls of the channel where the temperature gradient is highest.

- As the flow rate increases, a separated region forms at the exit microchannel. The size and intensity of the circulating flow in this region is higher in the abrupt expansion than the other geometries.

- The temperature gradient and as a result, the convection coefficient increases with flow rate. Thus, the thermal entropy generation, which is inversely proportional to the heat transfer coefficient, decreases with flow rate.

- It was found that the measured trends of the variation in entropy generation with geometrical shape and flow rate are similar to those of the model. Because of the fact that sharp corners can not be created with the fabrication techniques used in this work, no separation was observed and the entropy production in the abrupt entrance was not the highest for this geometry in contradiction to the model.

Bibliography

[1] H. Wu and P. Cheng, "Friction factors in smooth trapezoidal silicon microchannels with different aspect ratios," *International Journal of Heat and Mass Transfer*, vol. 46, pp. 2519–2525, 2003.

[2] Y. Muzychka, *Analytical and Experimental Study of Fluid Friction and Heat Transfer in Low Reynolds Number Flow Heat Exchangers.* PhD thesis, Department of Mechanical Engineering, University of Waterloo, 1999.

[3] N. Nguyen and S. Wereley, *Fundamentals and Applications of Microfluidics.* Norwood: McGraw-Hill, 1st ed., 2002.

[4] "SU-8 2000 permanent epoxy negative photoresist processing guidelines," *MicroChem Inc., Newton, MA*, 2000.

[5] K. Chen, "Second-law analysis and optimization of microchannel flow subjected to different thermal boundary conditions," *International Journal of Energy Research*, vol. 29, pp. 249–263, 2005.

[6] W. Khan, M. Yovanovich, and J. Culham, "Optimization of microchannel heat sinks using entropy generation minimization method," in *Twenty Second Annual IEEE Semiconductor Thermal Measurement and Management Symposium (Semi-Therm)*, (Dallas, TX), 14-16 March 2006.

[7] J. Santiago, S. Wereley, C. Meinhart, D. Beebe, and R. Adrian, "A particle image velocimetry system for microfluidics," *Experiments in Fluids*, vol. 25, pp. 316–319, 1998.

[8] C. Meinhart, S. Wereley, and J. Santiago, "PIV measurements of a microchannel flow," *Experiments in Fluids*, vol. 27, pp. 414–419, 1999.

[9] R. Fu, B. Xu, and D. Li, "Study of temperature field in microchannels of a PDMS chip with embedded local heater using temperature-dependant fluorescent dye," *International Jounrnal of Thermal Science*, vol. 45, pp. 841–847, 2006.

[10] E. Yamaguchi, V. Natarjan, and K. Christensen, "Development of a two-dye LIF technique for measuring fluid temperature fields in microfluidic devices," in *European Fluids Engineering Summer Meeting*, (Miami, FL), July 2006.

[11] O. Adeyinka and G. Naterer, "Particle Image Velocimetry measurment of entropy production with free convection heat transfer," *Transactions of the ASME*, vol. 127, pp. 614–623, 2005.

[12] G. Naterer and O. Adeyinka, "New laser based method for non-intrusive measurement of available energy loss and local entropy production," *Experimental Thermal Fluid Science*, vol. 31, pp. 91–95, 2006.

[13] S. Devasenathipaty, J. Santiago, S. Wereley, C. Meinhart, and K. Takehara, "Particle imaging techniques for microfabricated fluidic systems," *Sensors and Actuators*, vol. 34, pp. 504–514, 2003.

[14] F. White, *Viscous Fluid Flow.* Boston: McGraw-Hill, 3rd ed., 2005.

[15] M. Kohl, S. Abdel-Khalik, S. Jeter, and D. Sadowskii, "An experimental investigation of microchannel flow with internal pressure measurement," *International Journal of Heat and Mass Transfer*, vol. 48, pp. 1518–1533, 2005.

[16] P. Lee, S. Garimella, and D. Liu, “Investigation of heat transfer in rectangular microchannels,” *International Journal of Heat and Mass Transfer*, vol. 48, pp. 1688–1704, 2005.

[17] P. Lee and S. Garimella, “Thermally developing flow and heat transfer in rectangular microchannels of different aspect ratios,” *International Journal of Heat and Mass Transfer*, vol. 49, pp. 3060–3067, 2006.

[18] G. Hewitt, *Hemisphere Handbook of Heat Exchanger Design.* New York: Hemisphere, 1st ed., 1990.

[19] B. Munson, D. Young, and T. Okiishi, *Fundamentals of Fluid Mechanics.* New York: Wiley, 3rd ed., 1998.

[20] “Micro Particle Image Velocimetry, operation manual,” *TSI Inc., Shoreview, MN*, 2006.

[21] “Nano$^{\text{TM}}$ SU-8 2000 photoresists formulations,” *MicroChem Inc., Newton, MA*, 2002.

[22] D. Tuckerman and R. Pease, “High performance heat sinking for VLSI,” *IEEE Electron Device Letters*, vol. EDL-2, pp. 126–129, 1981.

[23] M. Yovanovich, Y. Muzychka, and J. Culham, “Spreading resistance of isoflux ractangles and strips on compound flux channels,” *Journal of Thermophysics and Heat Transfer*, vol. 13, pp. 495–500, 1999.

[24] A. Bejan, *Entropy generation minimization.* Boca Raton: CRC Press, 1st ed., 1996.

[25] “Particle Image Velocimetry, theory of operation,” *TSI Inc., Shoreview, MN*, 1999.

[26] H. Lee, “Application of a ratiometric laser induced fluorescence thermometry for microscale temperature measurement for natural convection flows,” Master’s thesis, Department of Mechanical Engineering, Texas A&M University, 1999.

[27] H. Abbassi, “Entropy generation analysis in a uniformly heated microchannel heat sink,” *International Jounrnal of Energy*, vol. 32, pp. 1932–1947, 2007.

[28] L. Erbay, M. Yalcin, and M. Ercan, “Entropy generation in parallel plate microchannels,” *Heat and Mass Transfer*, vol. 43, pp. 729–739, 2007.

[29] D. Ross, M. Gaitan, and L. Locascio, “Temperature measurement in microfluidic systems using a temperature-dependant fluorescent dye,” *Analytical Chemistry*, vol. 73, pp. 4117–4123, 2001.

[30] P. Wilding, M. Shoffner, and L. Kircka, “Manipulation and flow of biological fluids in straight channels micromachined in silicon,” *Clinical Chemistry*, vol. 40, pp. 43–47, 1994.

[31] I. Papautsky, B. Gale, S. Mohanty, T. Ameel, and A. Frazier, “Effect of rectangular microchannel aspect ratio on laminar friction constants,” *SPIE*, vol. 3877, pp. 147–158, 1999.

[32] X. Jiang, J. Zhou, Y. Yao, and X. Ye, “Micro-fluid flow in microchannel,” in *Proceedings of Transducers Conference*, 1995.

[33] G. Mala and D. Li, “Flow characteristics of water in microtubes,” *International journal of heat and fluid flow*, vol. 20, pp. 142–148, 1999.

[34] Q. Weilin, G. Mala, and L. Dongqing, “Pressure driven water flows in trapezoidal silicon microchannels,” *International Journal of Heat and Mass Transfer*, vol. 43, pp. 353–364, 2000.

[35] R. Phillips, *Microchannel Heat Sinks.* PhD thesis, Department of Mechanical Engineeinrg, Massachusetts Institute of Technology, 1987.

[36] R. Shah and A. London, *Laminar Flow Forced Convection in Ducts.* New York: Academic Press, 1st ed., 1978.

[37] F. Abdelall, G. Hahn, S. Ghiaasiaan, S. Abdel-Khalik, S. Jeter, M. Yoda, and D. Sadowski, “Drop caused by abrupt flow area changes in small channels,” *Journal of Experimental Thermal and Fluid Sciences*, vol. 29, pp. 425–434, 2005.

[38] A. Olsson, G. Stemme, and E. Stemme, “Diffuser-element design investigation for valveless pumps,” *Sensors and Actuators*, vol. 57, pp. 137–143, 1996.

[39] C. Meinhart, S. Wereley, and M. Gray, “Volume illumination for two-dimensional particle image velocimetry,” *Measurement Science and Technology*, vol. 11, pp. 809–814, 2000.

[40] R. Panton, *Incompressible Flow.* New York: McGraw-Hill, 1st ed., 1984.

[41] C. Meinhart and S. Wereley, “The theory of diffraction-limited resolution in microparticle image velocimetry,” *Measurement Science and Technology*, vol. 14, pp. 1047–1053, 2003.

[42] O. Tornblom, “Introduction course in Particle Image Velocimetry, course notes,” 2006.

[43] “PIVCAM 14-10 CAMERA Manual,” *TSI Inc., Shoreview, MN*, 2004.

[44] “INSIGHT 3G, user’s guide,” *TSI Inc., Shoreview, MN*, 2006.

[45] R. Figliola and D. Beasley, *Theory and Design for Mechanical Measurements.* New York: McGraw-Hill, 4th ed., 2006.

[46] O. Adeyinka and G. Naterer, “Experimental uncertainty of measured entropy production with pulsed laser PIV and Planar Laser Induced Fluorescence,” *International Journal of Heat and Mass Transfer*, vol. 48, pp. 1450–1461, 2005.

[47] B. Jo, L. VanLerberghe, K. Motsegood, and D. Beebe, "Three-dimensional micro-channel fabrication in polydimethylsiloxane (PDMS) elastomer," *Journal of Microelectromechanical Systems*, vol. 9, pp. 76–81, 2000.

[48] L. Yu, F. E. Tay, G. Xu, B. Chen, M. Avram, and C. Iliescu, "Adhesive bonding with SU-8 wafer level for microfluidic devices," *Journal of Physics: Conference Series*, vol. 34, pp. 776–781, 2006.